Universitat Politècnica de Catalunya

Doctoral Thesis

ULTRAFAST QUANTUM CONTROL OF ATOMS AND MOLECULES: A DENSITY MATRIX APPROACH

Iduabo John Afa

Supervisor:

Dr. Carles Serrat

A thesis submitted in fulfillment of the requirements for the degree of Doctor in Computational and Applied Physics

Nonlinear Dynamics, Nonlinear Optics and Laser Group (DONLL)

Department de Fisica

UPC

Acknowledgement

With all my heart, I give full gratitude to God Almighty for His grace, favour and mercy all through my life endeavours.

My deepest gratitude goes to my parents, Engr. and Mrs Afa and my siblings for their immeasurable support, advice and encouragement in helping me get to this point in my life. Without their support, none of this would have been possible.

I express my deepest thanks to my supervisor, Prof Dr. Carles Serrat for giving me the opportunity to carry out my PhD research under his supervision. I truly appreciate his support, patience and guidance all through the course of my research. He has always been there to direct me in striving to achieving better results and transforming me into being a better scientist.

I also deeply thank the director of the DONLL research group, Prof. Dr. Ramon Vilaseca, for creating an amazing research atmosphere that made us all feel at home. I truly appreciate his continuous help in solving all the problems I faced during the course of the programme.

My big thanks go out to all the collaborators involved in making this PhD thesis possible, for their helpful contributions to its success. I would also like to take this opportunity to thank all the professors, researchers and fellow students of the DONLL research group, you all have made the PhD experience a great one. I also thank my friends, Benjamin, Dipo, Ebiakpo, Kenneth and many more.

Eli Alvarez, you've been a great inspiration to me. Your strength and support have kept me going. Words are not enough to express my thanks for your love and patience.

Lastly, I acknowledge the grant "Plan Nacional FIS2014–51997–R" from the Spanish Ministry of Economics and Competitiveness.

Abstract

Control is important for transferring theoretical scientific knowledge into practical technology for applications in numerous fields. This is why coherent control study is significant on every timescale to have a complete understanding of dynamic processes that occur on the electron, atomic and molecular levels. As a result, numerous schemes have been proposed to carry out effective control of diverse systems. This study focuses on coherent control of systems based on their natural timescales from the picoseconds (10^{-12} s), femtosecond (10^{-15} s) to attosecond (10^{-18} s) regimes. For instance, in photochemistry a long standing goal is to achieve selective population transfer from an initial state to a desired target state with little or no diminution in the energy transferred. Another application is the excitation of unoccupied Rydberg states for the design and implementation of robust fast two-qubit gates in quantum computation.

This thesis explores the modelling of dynamical light-matter interaction processes, like effective population inversion and generation of vibrational coherences in atoms and molecules, on their fundamental timescales using the density matrix (DM) theory under and beyond the rotating wave approximation (RWA). One main advantage of the density matrix over other theoretical approaches is that it allows the possibility of easily computing relaxation terms and other physical parameters critical to successful coherent control. The density matrix formalism is shown to be successful in properly describing the enhancement effects in atoms and complex molecular systems, it is robust in coherent control and quantum control spectroscopy (QCS) schemes and is extendable to numerous systems and geometric configurations. In the last part of the thesis, experiments on laser dressing processes in attosecond transient absorption spectroscopy are compared to numerical simulations using the DM formalism beyond the RWA. The research in this thesis thus opens a pathway to numerous studies using the DM formalism for applications in diverse fields of femtochemistry, attophysics, high precision spectroscopy and quantum information processing.

List of Publications and Presentations at Conferences

Peer-Reviewed Articles

1. Serrat, Carles, Corbera, Montserrat, and **Afa, John** "Trichromatic π-pulse for total inversion of a four level system, **Applied Sciences, Vol. 5, Issue 4, pp 1484 – 1493. http://www.mdpi.com/2076-3417/5/4/1484. doi: 10.3390/app5041484.**

2. **Afa, Iduabo John,** Serrat, Carles, "Quantum control of population transfer and vibrational states by chirped pulses in four level density matrix equations" **Applied Sciences, Vol. 6, Issue 11, pp 351 – 364. http://www.mdpi.com/2076-3417/6/11/351. doi: 10.3390/app6110351.**

3. **Afa, Iduabo John,** Font, Josep Lluis, and Serrat, Carles, "Control of rubidium low-lying Rydberg states with trichromatic femtosecond π-pulses for ultrafast quantum information processing". **Physical Review A, Vol. 96, Iss. 5, 053843. https://link.aps.org/doi/10.1103/PhysRevA.96.053843**

4. Seres E, Seres J, Namba S, **Afa J,** Serrat C, "Attosecond transient absorption and Fourier transformation spectroscopy of strong field laser dressing and beating on 3d to 5p and 3p to 5s core-transitions in Krypton", **Submitted – Optics Express.**

Oral Presentations at Conferences

5. Brühl, Elisabeth, **Afa, Iduabo John,** Serrat, Carles, Buckup, Tiago and Motzkus, Marcus "Combination of Chirped and Multipulse Excitation: Control of Population and Vibrational Coherence", **Deutsche Physikalische Gesellschaft e.V. (DPG) Spring Meeting of AMOP, Heidelberg, Germany, 23 – 27 March, 2015. (Link: http://www.dpg-verhandlungen.de/year/2015/conference/heidelberg/part/mo/session/2/contribution/)**

6. Serrat, Carles, **Afa, Iduabo John,** Brühl, Elisabeth, Buckup, Tiago, and Motzkus, Marcus "Quantum control of population transfer and vibrational states by chirped pulses in four level density matrix equations", **Session 5D02 (11:30am), Room D, 26th IUPAC International Symposium on Photochemistry, 3-8th April 2016, Osaka, Japan.**

Poster Presentations at Conferences and Schools

7. **Afa I.J.,** Serrat C, Brühl E, Buckup T, Motzkus M, "Quantum Control of Population Transfer and Vibrational Coherences by chirped ultrashort pulses in four level density matrix equations of Oxazine Systems", **Sao Paulo School of Advanced Science on Nanophotonics and XV Jorge Andre Swieca School on Nonlinear and Quantum Optics, 17-29th July, 2016, Instituto de Fisica Gleb Wataghin (IFGW), Campinas, Brazil. http://sites.ifi.unicamp.br/spsasnano/**

8. **Afa I.J.,** Serrat C, "Multiphoton π-pulse excitation for ultrafast population inversion of Alkali atoms", **VI Erasmus Mundus Europhotonics-POESII Spring School, 22-24th March, 2017, Sitges, Barcelona, Spain. http://www.europhotonics.org/wordpress/spring-school**

9. **Afa I.J.,** Font J.L., Serrat C, "Ultrafast coherent control of low-lying Rydberg states with trichromatic femtosecond π-pulses", **8th International Symposium on Ultrafast Photonics Technology, 10-11th July, 2017 (ISUPT-2017), Winchester School of Arts, University of Southampton, Winchester, United Kingdom. Organized by the Optoelectronics Research Centre (ORC), Southampton, UK. http://www.isupt2017.co.uk**

10. Serrat, Carles, **Afa, Iduabo John,** Font, Josep Lluis, 'Ultrafast coherent population transfer with trichromatic femtosecond π-pulses in a four-level ladder system'. **14th International Conference on Multiphoton Processes (ICOMP), Budapest, Hungary, 24 – 27th September, 2017.**

Chapter 1

Introduction

Ultrafast laser spectroscopy has been of huge significance in the characterization of atomic, molecular and biochemical system dynamics [1]. When dealing with coherent fields interacting with quantum mechanical systems, quantum interference becomes an essential phenomenon. Therefore, being able to understand how this quantum interference can be properly manipulated to effectively control the dynamic processes that occur when these atoms and molecules interact with some form of coherent excitation, can broaden our comprehensive understanding of the dynamics and physio-chemical properties of these systems.

A fundamental concept in ultrashort laser spectroscopy is the control of population transfer from an initial state to a target state and the generation of vibrational coherences between different states. The importance of these coherent effects makes it worth employing numerous theoretical models to explore the influence of these effects and compare them with the experiments [2]. To achieve this level of control of dynamic processes, numerous approaches have been introduced to utilize the coherence of laser excitation fields and the quantum interference effects among the eigenstates of atoms and molecules to achieve control of targeted states in the systems. Coherent control comprises numerous techniques that can steer quantum mechanical systems to target electronic states using carefully tailored coherent excitation [3]. For instance, a photoreaction can be channelled towards a desired product channel through modulated excitation. Also selective control of chemical reactions like bond formation and dissociation become possible on a microscopic level [4].

The implementation of these methods is dependent on the size and other properties of the system studied, whether it is an atomic or a simple molecular system, complex chemical, bio-molecular or a solid state system or nano-systems [5]. These control methods could be in the temporal, frequency or adiabatic domain in single and multilevel transitions.

Studies on coherent population trapping (CPT) and electromagnetically induced transparency (EIT) set the basis for many coherent control techniques based on combined detuned lasers and adiabatic transfer [6–12]. The concept of CPT was employed to demonstrate pumping of atomic systems in a particular state, and has been theoretically analyzed by Arimondo and Orriols [7] and Gray et al. [8] based on the solution of the Bloch-like equations of motion for a 3-level system with applications in Sodium atoms. This concept was further experimentally demonstrated by Whitley and Stroud [10].

The main goal of these studies was to optimally pump as much population as possible to the excited state from the ground state with the requirements of a proper combination of density matrix relaxation rates, Rabi frequencies and precise detuning of the laser field. An important scheme combined with CPT and EIT is the adiabatic transfer scheme, which entails using two pulses, a Stoke and pump pulse with a delay between these pulses which turns off the initial pulse from returning the population to the lower levels thereby successfully trapping the final population in the target state. The stimulated Raman adiabatic passage (STIRAP) fosters the generation of Rabi oscillations. Two photon Rabi transfer has been previously demonstrated for resonant and near-resonant excitation based on Rabi flopping [13, 14, 15].

Previous studies employing adiabatic transfer schemes have been used to demonstrate EIT for achieving population transfer to bounded states in atomic systems [9, 16, 17] and molecular systems [18, 19], with extensions to solid media [20]. Some studies also showed the possibility of extending these techniques to four-level schemes, achieving a limited but significant amount of population transfer [21].

This previous research showed the potential for other interesting phenomena in multilevel systems, such as transfer to higher bound and continuum levels [8], and development of techniques for efficient transfer to unpopulated Rydberg states [18], which is essential for further advancement on spectroscopy, collision dynamics, quantum memories [20] and photon control in quantum information processing [22]. Kuklinski et al [18] showed an extension to the Heisenberg picture which presents a solution of the Liouville equations that allows the computation of the relaxation processes during the evolution of population transfer in multilevel systems. Zhang and George [23–25] employed the dynamical solution of the Liouville equations to find a practical path to more efficient CPT in Fullerenes with a proper combination of parameters, like time delay and pulse duration. CPT and EIT have also been demonstrated in Rubidium with extensions to different multilevel configurations, for instance, in a 3-level Λ-type and ladder-type atomic systems in ^{87}Rb atoms cooled and confined in a magneto-optical trap [26], in a three-level V-type system in a D2 transition of ^{87}Rb [27], in a 4-level inverted-Y atomic system [28], and in a 4-level tripod atomic system in the ^{87}Rb D1 line [29].

One of the earliest schemes was introduced by Brumer and Shapiro [30], which was a quantum pathway interference method based on phase control in the frequency domain. They theoretically demonstrated that the transition probability can be controlled by manipulating the relative phase between two excitation pathways that lead to the desired reaction product. This method has been used to demonstrate population transfer [31]. For instance, control has been achieved in the ionization of atoms such as Hg [32], in the ionization of deuterium iodide (DI) molecules using the 3ω–ω scheme [33] and also in semiconductors like N-doped AlGaAs/GaAs specially designed quantum wells [34]. Another interesting application is in the control of nonlinear parametric processes with femtosecond pulses using Four wave mixing (FWM) [35].

Another very relevant approach to coherent control is the temporal control scheme using the pump-probe (pump-dump) technique in time-resolved spectroscopy. Initially introduced in the work of Tannor, Kosloff and Rice [36], this method has become ubiquitous in experimental demonstration of control in atomic and molecular systems [37]. The method introduces the implementation of the wavepacket that is created when ultrashort pulses excite several vibrational states. This vibrational wavepacket play a huge role in light absorption processes of these molecules investigated. The pump-probe (pump-dump) method can be employed to control the wavepacket, shown in figure 1.1(a).

Baumert et al [38, 39] demonstrated bond formation and breakage of Na_2 by applying a wavepacket to both ground and excited state potential energy surfaces (PES). Proper manipulation of the phase of the laser pulse can foster change in the amplitude of the wavepacket which could lead to an enhancement or suppression of the population transfer between electronic states and the vibrational coherence generation between these states. Introduction of different pulse shaping methods capable of phase modulation, for instance methods like optimal control theory that combine wavepackets or density matrix propagation between states and self learning algorithms [40], has sparked numerous interests in implementing this temporal domain method for coherent control of quantum systems.

Ideally, transform-limited (TL) pulses can be tailored into modulated single or train of pulses as shown in figure 1.1(b), which can achieve increased selectivity and recently shown enhancements of population transfer to target states [41]. A comparison of the transient behaviour of these molecular systems after interaction with transform limited (unmodulated) and a shaped excitation sets up the conceptual basis for quantum control spectroscopy, which will be discussed in further detail in Chapter 5. Since the advent of extreme ultraviolet (XUV) and x-ray pulses generated using high harmonics processes, the pump-probe method has also

been extended to attosecond physics experiments, where the electronic dynamics are examined on their fundamental timescale [42].

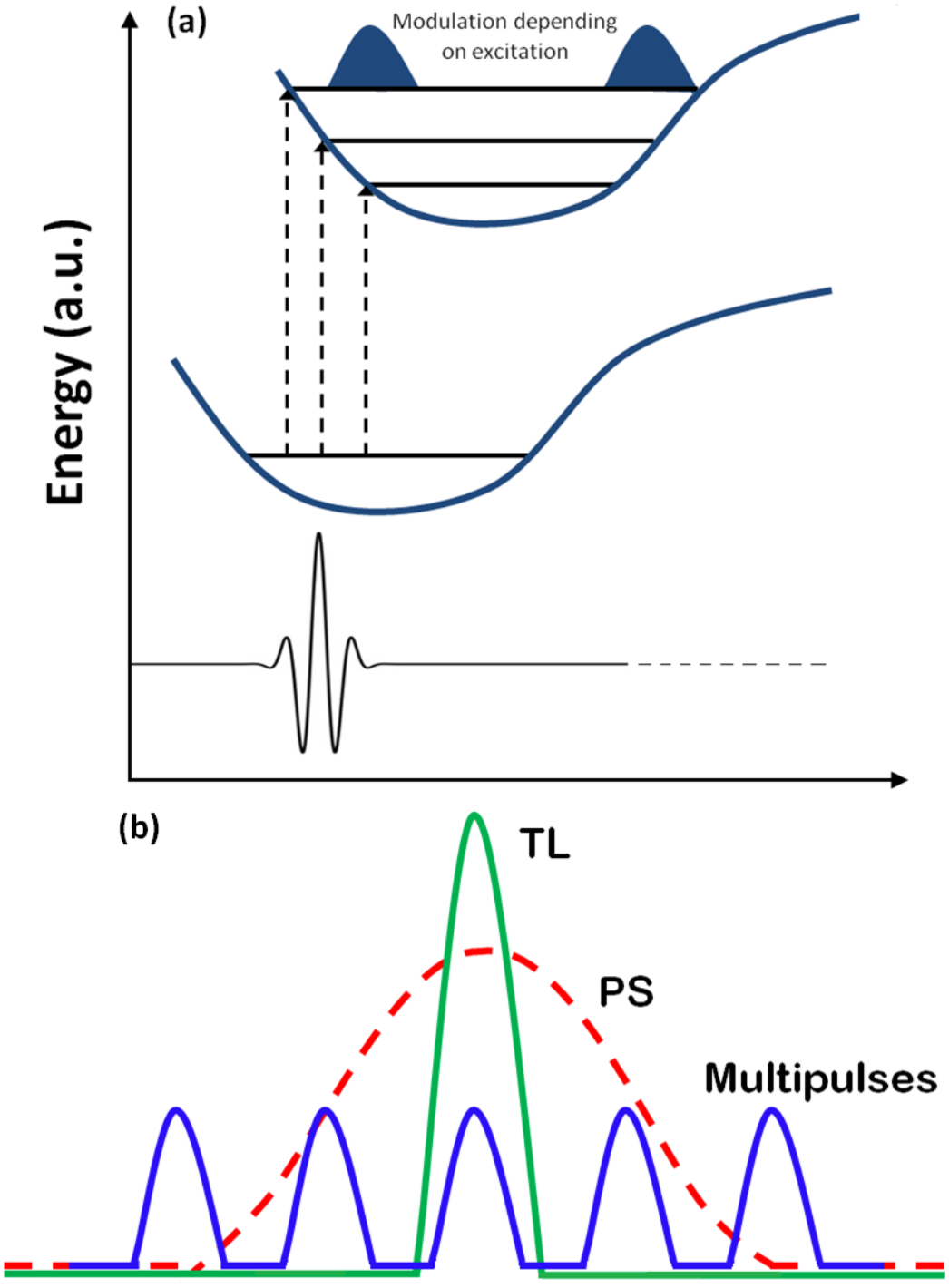

Figure 1.1: (a) Vibrational wavepacket theory (b) TL pulse (green), modulated pulse (red-dotted lines) and train of pulses (blue).

These coherent control schemes have been demonstrated to have prospective applications in numerous fields which will be discussed in section 1.1.

1.1 Applications of Coherent Control

The potential of the earlier mentioned schemes to control quantum systems has been an essential prerequisite for present and future applications involving manipulation of atoms, molecules and other forms of matter [5]. Numerous applications of coherent control are demonstrated in fields such as femtochemistry [4, 43], quantum information processing and Rydberg states [44, 45], attosecond physics [42] and nanoscience [46].

One of the most prominent applications of coherent control is femtochemistry. This field of chemistry allows studies of chemical, biological and physical variations in molecules to be observed on a timescale equivalent to that of atomic motion and molecular vibrations. The main goal of femtochemistry is to study atomic motions during chemical reaction processes such as bond formation and breakage, as they are steered through vibrational states. Ahmed Zewail, known as the founding father of femtochemistry, was awarded the 1999 Nobel Prize in Chemistry for his groundbreaking work on transition states of chemical reactions using femtosecond spectroscopy through pump-probe experiments [43]. Since then, several studies on femtochemistry have been done from demonstration of the control of simple atomic and molecular systems such as iodine [47], control of complex systems, for instance, photodissociation processes [48], retinal isomerization [49], study of emission properties of fluorescent molecules [50] and control of energy transfer pathway in biomolecules [51].

Another important application is in quantum information processing. Preparation of states for quantum simulation and logic gates has been a “huge” achievement of coherent control [45, 52]. The introduction of Rydberg states has opened pathways to expanded applications in

quantum computation [53]. Protocols using Rydberg interaction and control have been proposed in quantum information applications. An example is the design of fast quantum gates [54], collective encoding of multiqubit registers [45], quantum interfaces, hybrid quantum devices, superconducting circuits [55] and ultracold molecules for Bose-Einstein condensates (BEC) [56].

Coherent control applications can be expanded to attosecond physics. Corkum and Krausz first identified experimentally electronic motion on the atomic scale, which opened doors to time-domain control of atomic-scale electron dynamics and their real-time observation [57]. Control schemes such as the pump-probe method have been used to study ultrafast processes on the attosecond timescale. The applications have expanded to the study of ultrafast x-ray diffraction of biological samples [58], real time observation of fast material responses [59]. Other applications are in the study of attosecond pulse generation with high frequency weak extreme ultraviolet (XUV) and strong infrared (IR) pulses [60, 61] and also, in attosecond vacuum UV control of the dynamics of simple molecular systems like simple Hydrogen H_2 and Deuterium D_2 molecules [62]. Here, they combined VUV (<200 nm) attosecond pulse trains from high harmonic generation (HHG), i.e. 7ω–13ω, synchronized with an IR field (784 nm) together with another delayed IR field. By doing such, they were able to demonstrate ionization control of electron wavepackets in the excited neutral and singly ionized molecules.

Another application worth mentioning is in the control of nanostructures. The importance of applying coherent control is to study ultrafast nanoscale processes like energy localization in nanosystems, time-resolved nanoscale probing and detection [63]. Stockman *et al* demonstrated the effect of shaped excitation on a V-shaped nanostructure. Extensive understanding of these effects could open doors for energy distribution and control of optical

computations in nanostructures. The study is even further extended to the attosecond timescale with possible applications in ultrafast nanoplasmonics [64].

1.2 Scope of the thesis

The thesis is divided into six chapters. Chapter 2 discusses the theoretical concepts used in the context of the thesis. Ultrashort pulses are introduced, and then electric field, Rabi oscillations, π-pulse scheme and density matrix formalism are explained. Chapter 3 introduces the multiphoton π-pulse scheme. First, bichromatic π-pulse excitation in a three level system is shown and optimal parameters are established. Next, extended results from trichromatic π-pulse excitation in a four level cascade system are shown using the density matrix formalism. The goal is to demonstrate the influence of different parameters and phenomena that affect population inversion like detuning and chirp.

Chapter 4 introduces Rydberg atoms and multiphoton π-pulse excitation of these atoms. Later on, the applications of Rydberg atoms are presented. With a focus on application to quantum information processing, control of low-lying Rydberg states of Hydrogen-like alkali atoms (for instance, Rubidium atom) is demonstrated. The results of the simulations are presented showing a comparison between using the rotating wave approximation (RWA) and going beyond the RWA. Influence of detuning and comparison between the results obtained using single and multiphoton π-pulse schemes are investigated. Chapter 5 introduces the application of coherent control and quantum control spectroscopy (QCS) in time-resolved spectroscopy and transient absorption spectroscopy (TAS). Enhancement and suppression effects in typical Oxazine systems are examined and results on population transfer and vibrational coherences and how they are influenced by different parameters are discussed.

In chapter 6, TAS is extended to the attosecond regime. At the beginning of this chapter, the concept of attosecond transient absorption spectroscopy (ATAS) is introduced. After that, the density matrix formalism is used to support experimental measurements on laser dressing on XUV transmission. A study on the time-evolution of the atomic polarization response of Krypton (Kr) is presented. Experimental results obtained by the group of Professor Jozsef Seres in Vienna (Austria) on the dynamics of the transient absorption in Kr for weak and strong field ionizations are shown. Theoretical calculations using the density matrix formalism beyond the RWA are compared to these experimental measurements. Finally, the summary and bibliography are presented.

Chapter 2

Theoretical Background

Ultrashort laser spectroscopy and coherent control as stated earlier are used to steer quantum mechanical processes in atoms and molecules through manipulation of properties of the optical fields. No matter what technique is used to achieve this goal, there are physical parameters and phenomena that are depended on to achieve desired results. It is essential to understand these parameters and phenomena to achieve optimal control and fully understand the dynamics of these systems as they interact with coherent excitation.

In this chapter, we are going to cover the characteristics of ultrashort pulses based on the electric field, as they are electromagnetic waves. Parameters like field intensity (i.e. modulus square of field amplitude), the duration of the excitation pulse, chirp and spectral phase of the pulse are briefly introduced. We are also going to briefly look at Rabi oscillation and its frequency, pulse area theorem and π-pulse excitation using multiphoton excitation schemes for resonant and detuned transitions. We will further discuss the density matrix formalism by first defining the properties of the density operator, then examining light-matter interaction using this formalism and the optical Bloch equations for a simple two level system, considering cases with and without decay and dephasing times. The non-pertubative density matrix approach will be further expanded to multilevel systems in subsequent chapters under different approximations such as the RWA and the slowly varying envelope approximation (SVEA), and additionally applied to different systems.

2.1 Characteristics of ultrashort laser pulses

Since the advent of ultrashort (pico- and femtosecond) laser pulses, coherent control and time-resolved spectroscopy has experienced a wide range of successful applications [43, 47 – 49]. This success is due to the possibility of obtaining more spectroscopic information as a result of the larger bandwidths of these very short pulses, and has opened a vital pathway into the understanding of dynamic behaviours of atomic, molecular and solid state systems that influences our comprehension of science in general.

In this section, we take a look at some characteristics of ultrashort laser pulses and their interaction with matter. First, the electric field and its representation with ultrashort pulses will be examined.

2.1.1 Electric field and field amplitude

Ultrashort pulses are electromagnetic waves and as such can be fully demonstrated mathematically by the spatial and temporal dependence of the electric field which directly relates to numerous measurable physical quantities that facilitate the characterization of these pulses. For the intensities used in the present research, the magnetic field of the electromagnetic wave can be neglected. When considering a case where these electromagnetic pulses undergo interaction, the complex representation plays a key role in managing problems relating to the propagation of these pulses. The electric field can be illustrated in the time and frequency domains [2].

The linearly polarized real-valued time-dependent laser pulse electric field oscillating with a carrier frequency ω, is given as:

$$E(t) = E_0(t)cos[\omega t + \varphi(t)] \qquad (2.1)$$

Neglecting the spatial dependence by considering the light pulse at a fixed point in space, the real oscillating electric field can also be written as

$$E(t) = Re\{E_o(t)e^{-i[\omega t + \varphi(t)]}\} \qquad (2.2)$$

Where $E_o(t)$ is the field amplitude, ω is the angular laser frequency and $\varphi(t)$ is a time-varying phase . The complex spectrum of the field strength, $\tilde{E}(\omega)$, through the Fourier transform ($\mathfrak{F}$) can be defined as:

$$\tilde{E}(\omega) = \mathfrak{F}\{E(t)\} = \int_{-\infty}^{+\infty} E(t)e^{-i\omega t}dt \qquad (2.3)$$

$$\mathfrak{F}\{E(t)\} = \left|\tilde{E}(\omega)\right|e^{-i\varphi(\omega)} \qquad (2.4)$$

Considering E(t) to be real, the conditions $\tilde{E}(\omega) = \tilde{E}^*(-\omega)$ and $\varphi(\omega) = -\varphi(-\omega)$ hold [2].

The time-dependent electric field can be directly obtained by the inverse Fourier transform ($\mathfrak{F}^{-1}$) of the frequency-dependent electric field in (2.3)

$$E(t) = \mathfrak{F}^{-1}\{\tilde{E}(\omega)\} = \frac{1}{2\pi}\int_{-\infty}^{+\infty} \tilde{E}(\omega)e^{-i\omega t}d\omega \qquad (2.5)$$

Where, E(t) and E(ω) represent the time and frequency evolution of the electric field of the laser pulse, as shown in figure 2.1.

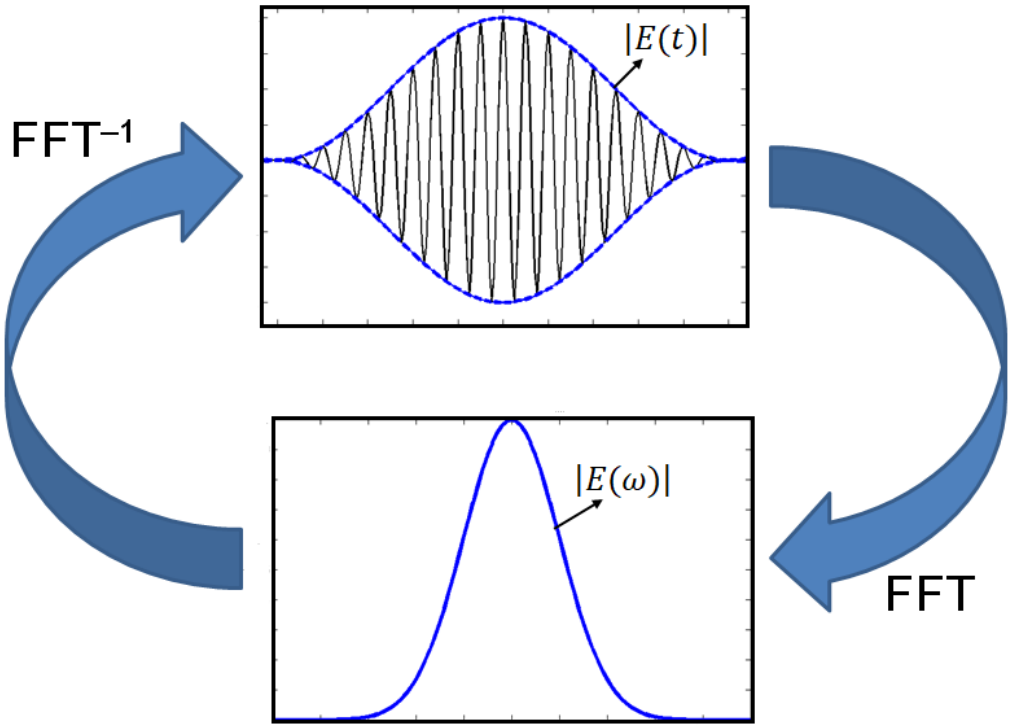

Figure 2.1: Representation of the time-dependent and spatial-dependent electric fields in the temporal and frequency domain for a transform limited pulse. The Fourier transform relationship is demonstrated.

The complex time-dependent electric field $\tilde{E}(t)$ can be further represented by a product of its amplitude function and the time-dependent phase term, φ(t) as;

$$\tilde{E}(t) = E_0(t)e^{-i\varphi(t)}e^{-i\omega t} \quad = \quad \tilde{\varepsilon}(t)e^{-i\omega t} \qquad (2.6)$$

Where $\tilde{\varepsilon}(t)$ is the slowly varying complex amplitude. Extension to polychromatic laser sources is very important in the understanding of this thesis (Chapter 3). In this case, the total electric field E(t) consists of oscillating fields [$E_1(t)$, $E_2(t)$, ... $E_n(t)$] with individual contributions to the total E(t) with each individual field possessing its amplitude, angular laser frequency and phase term.

The field intensity of the laser pulse is of critical importance when demonstrating interaction of these pulses with atoms and molecules. The field intensity can be described in the

frequency and time domain as proportional to the square modulus of the electric fields, $E(\omega)$ and $E(t)$ respectively:

$$I(t) = \frac{1}{2}\varepsilon_0 c|E_0(t)|^2 \qquad (2.7)$$

$$I(t) \propto |E(t)|^2 \qquad (2.8a)$$

$$I(\omega) \propto |E(\omega)|^2 \qquad (2.8b)$$

2.1.2 Pulse duration and Spectral bandwidth

Pulse duration is a fundamental physical parameter to further characterize ultrashort pulses and classify their interaction with matter in terms of the appropriate timescales [65].

It is widely known that half maximum quantities are easier to measure experimentally. Hence, pulse duration, τ_{FWHM} can be defined as the full width at half maximum (FWHM) of the intensity in time, I(t), while the spectral bandwidth, $\Delta\nu$ as the FWHM of the spectral intensity, I(ω) . Both τ_{FWHM} and $\Delta\nu$ are dependent on each other as they are directly linked by the Fourier transform, therefore, they fluctuate together [2]. The relationship between these two quantities can be mathematically represented by the "pulse duration–spectral bandwidth" product given as:

$$\Delta\nu \times \tau_{FWHM} \geq K \qquad (2.9)$$

Where, K is a numerical constant that depends on the definite pulse profile. The condition of $\Delta\nu \times \tau_{FWHM} = K$ in the equation (2.9) above holds for transform-limited pulses, that is to say, pulses without any frequency modulation.

In numerical calculations, the shape of the pulse plays an important role and is more ideal for implementation. The two widely quoted pulse profiles are the Gaussian and Hyperbolic secant

pulses [2, 66]. The temporal dependence of the field for the Gaussian and hyperbolic secant pulse profiles can be written as (2.10) and (2.11) respectively [2];

$$\varepsilon(t) = \varepsilon_0(t)e^{-(t/\tau_p)^2} \qquad (2.10)$$

$$\varepsilon(t) = \varepsilon_0(t)\,\mathrm{sech}\left(\frac{t}{\tau_p}\right) \qquad (2.11)$$

The corresponding values of τ_p are $\tau_p = {}^{\tau_{FWHM}}/_{\sqrt{2\ln 2}}$ and $\tau_p = {}^{\tau_{FWHM}}/_{1.76}$ for the Gaussian and hyperbolic secant profiles. A constant angular frequency TL pulse has a duration-bandwidth product of $\Delta\nu \times \tau_{\mathrm{FWHM}} \cong 0.441$ while for a hyperbolic secant pulse, the product is $\Delta\nu \times \tau_{\mathrm{FWHM}} \cong 0.315$.

2.1.3 Chirp and Spectral Phase

TL pulses are pulses free of phase modulation. This means that $\varphi(\omega)$ = constant and $\varphi(t) = 0$. In the Fourier domain, chirp can be defined as the amount of group delay dispersion (GDD) added to the spectral phase of the pulse. This dispersion addition could be as a result of propagating these short laser pulses through a transparent dispersive medium, which leads to a phase modulation in the frequency domain by changing the phase of the pulse without affecting its spectral amplitude [2].

The said quadratic phase modulation plays a key role in light propagation, whether in the temporal or spatial domain. It results from the different phase delays that different spectral components experience on interaction. Due to this frequency chirp, a TL pulse in the time domain becomes temporally broadened with a certain frequency distribution across the envelope, such that the spectral amplitude profile remains unchanged.

In this thesis, the spectral chirp parameter φ″ was implemented in the Fourier domain and is defined as

$$\varphi(\omega) = \frac{1}{2}\varphi''(\omega_l - \omega_0)^2 \qquad (2.12)$$

φ(ω) is the group delay dispersion (GDD) added to the spectral phase of the pulse. The rephasing of the spectral components that leads to the time broadening of the pulse can be given by [2]

$$\tau_{p_c} = \sqrt{\tau_p{}^4 + 16\,(\ln 2)^2 \varphi''^2/\tau_\mathrm{p}} \qquad (2.13)$$

Where, τ_{p_c} is the FWHM of the chirped pulse intensity profile and τ_p is the pulse duration of TL pulse. The physical interpretation of phase function φ(t) and chirp can be further demonstrated in the time domain.

Assume a pulse propagating with an instantaneous frequency, ω(t) which is dependent on the variation of the phase function φ(t). This instantaneous frequency, ω(t) can be given as:

$$\omega(t) = \omega + \frac{d}{dt}\varphi(t) \qquad (2.14)$$

Where, ω is the angular laser frequency. A case where $\frac{d}{dt}\varphi(t)$ is constant, the pulse is referred to as an unchirped pulse and therefore, transform limited. In a case where $\frac{d}{dt}\varphi(t)$ is not constant, i.e.

$$\frac{d}{dt}\varphi(t) = f(t) \gtrless 0 \qquad (2.15)$$

The carrier frequency varies with time and the pulse is said to be chirped [2]. From equation (2.15), if the carrier frequency decreases along the pulse, the pulse is described as being down

or negatively chirped and if the frequency increases, it is said to be up or positively chirped (shown in figures 2.2(c) and (d)).

As we considered a Gaussian pulse profile, a linearly chirped pulse would have an electric field given by

$$\tilde{E}(t) = E_0 e^{-(t/\tau_p)^2} e^{-i\omega t} e^{-i\varphi(t)} \qquad (2.16)$$

With pulse duration $\tau_p = \tau_{FWHM}/\sqrt{2\ln 2}$ and a chirp parameter, a_0, which is positive for down chirped pulses and negative for up chirped pulses having a time dependent phase, with $\varphi(t) = -a_0 t^2/{\tau_p}^2$. This can be represented as a cosine function as in equation (2.1) for a single component pulse [2].

$$E(t) = e^{-(t/\tau)^2}\left\{E_0 \cos\left[\omega_0 t - a_0\left(\frac{t}{\tau_p}\right)^2\right]\right\} \qquad (2.17)$$

Where E_0 is the peak amplitude, $e^{-(t/\tau)^2}$ is the Gaussian profile. Figure 2.2(a) shows a TL pulse which has not been frequency modulated. Figure 2.2(b) shows the pulse after the Fourier transform ($\mathfrak{F}$) in the frequency domain where the positive or negative frequency modulation is implemented, it demonstrates the quadratic term which is a parabolic function introduced to the phase to create a linear chirp that leads to a temporally broadened pulse in the time domain after the inverse Fourier transform ($\mathfrak{F}^{-1}$) as shown in Figure 2.2(c) and (d) for up-chirped and down-chirped pulses respectively.

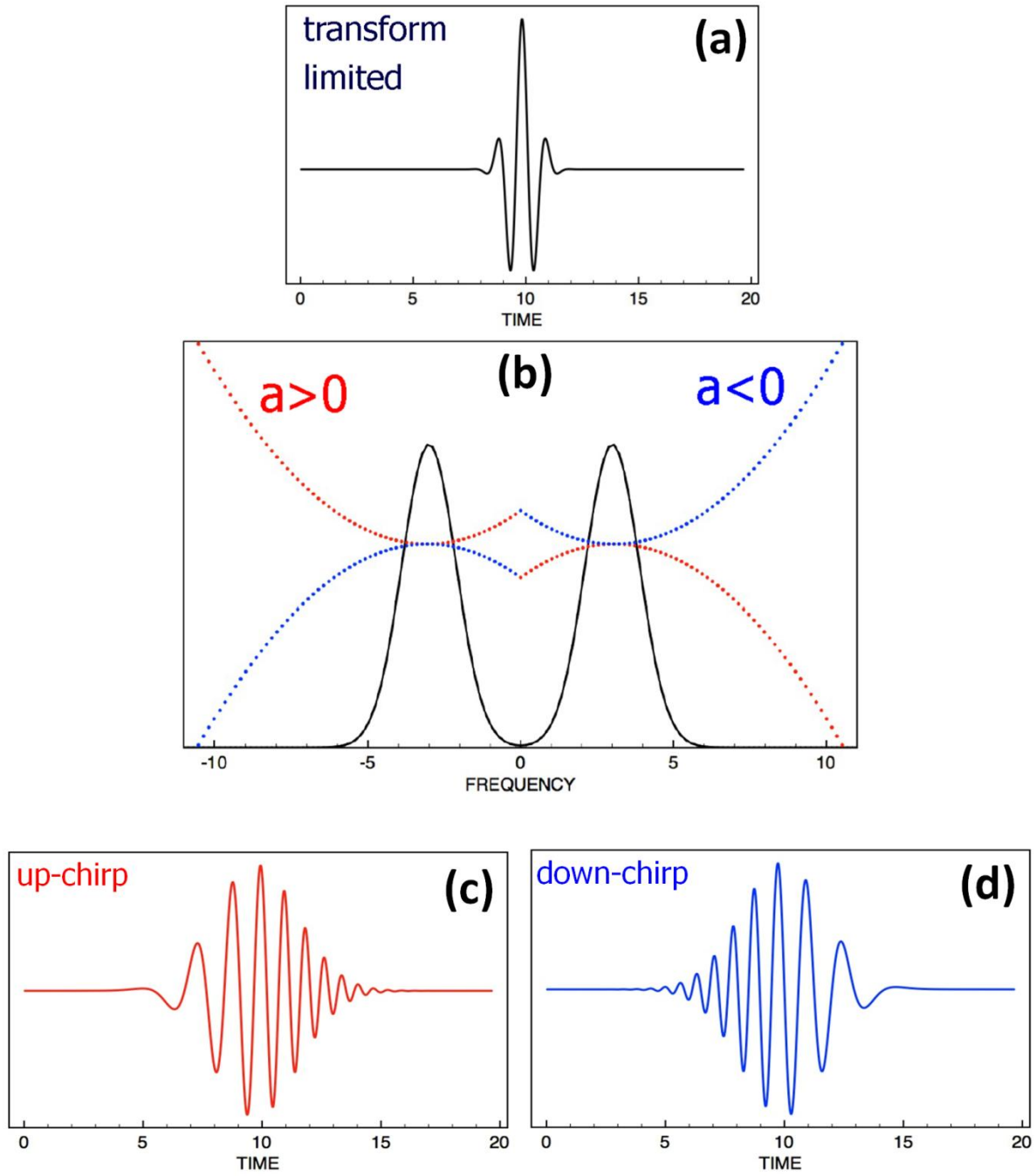

Figure 2.2: (a) TL pulse in time domain which is Fourier transformed (b) The frequency domain of the pulse where the spectral phase chirp is applied (c) Up-chirped pulse which represents an addition of a positive chirp (d) Down-chirped pulse which represents addition of a negative chirp.

2.2 Rabi Oscillation

Rabi oscillations are oscillations of atomic population between two coherently coupled states and are a confirmation of the coherence of the coupling between these two states. To demonstrate this concept, assume a two level system coherently interacting with a near–resonant or resonant pulse. This interaction is characterized by the Rabi oscillation which is dependent on Rabi frequency, Ω_R, involving the coupling strength, pulse duration and field amplitude. This means the pulses can easily be characterized by the Rabi frequency, which is a frequency measure of the electric dipole interaction between the field and the atomic system given by [67]:

$$\Omega_R(t) = \frac{\mu_{ab} E_0}{\hbar} \qquad (2.18)$$

Where, μ_{ab} is the transitional dipole moment. Assuming introducing detuning, this means setting the laser frequency to be slightly off-resonant with the transition, $|a\rangle \rightarrow |b\rangle$, i.e. $\omega_{ab} - \omega = \delta$, as shown in figure 2.3.

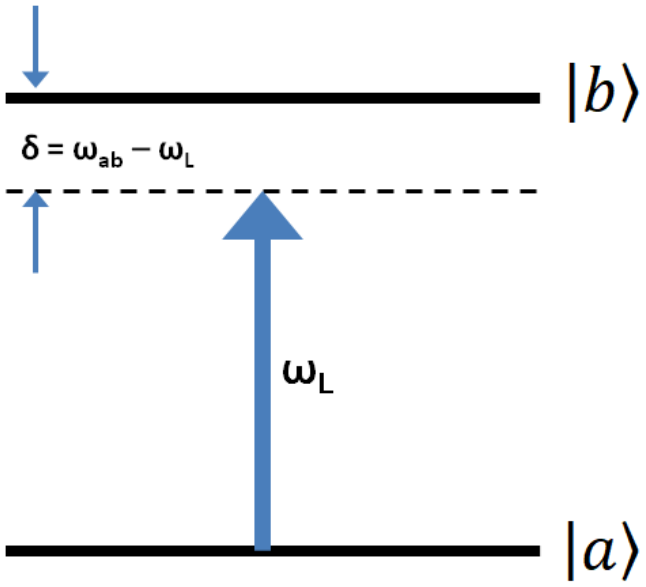

Figure 2.3: 2-level system showing field detuning, $\delta = \omega_{ab} - \omega_L$

Then the generalized Rabi frequency, Ω_G, will become

$$\Omega_G = \sqrt{{\Omega_R}^2 + \delta^2} \qquad (2.19)$$

Where, Ω_R is the resonant Rabi frequency at which the population oscillates between the states, $|a\rangle$ and $|b\rangle$.

A fundamental physical parameter for a coherent resonant interaction is the pulse area, θ, which can be fully described using the McCall and Hahn Pulse area theorem [68]

$$\frac{d\theta}{dz} = -\frac{\alpha}{2}\sin\theta \qquad (2.20)$$

With the pulse area θ being the angle that incline the pseudo-polarization vector as demonstrated in Figure 2.4 at resonance when Δω = 0 and given by

$$\theta = \int_{-\infty}^{\infty} \Omega(\mathrm{t}) d\tau \qquad (2.21)$$

Where Ω(t) is the Rabi frequency. In a case of adequately intense pulse excitation which defines the π-pulse area condition, it is possible to achieve a complete atomic population inversion in a two level system when $\theta = \Omega\tau = \pi$

This means that pulses with area θ becomes multiples of π that propagate between the transitions of the atomic system with no changes to the field amplitudes [69].

$$\theta = \int_{-\infty}^{\infty} \Omega(\mathrm{t}) d\tau \equiv n\pi \qquad (2.22)$$

$$\theta \equiv \Omega\tau = n\pi \qquad (2.23)$$

As the electric field amplitude E_0 is strongly linked to the Rabi frequency as shown in equation (2.18), it is therefore dependent on the area. A consequence of this is that in an

absorbing medium, one can keep the area fixed. Therefore, the product $\mu\tau_p$ has to be sufficiently large enough to compensate the field amplitude in order to avoid the E_0 from producing strong ac–Stark effects [70]. Chirp can be applied to increase the pulse duration thereby reducing the field strength to avoid these effects.

Pulses with an area value that is an odd multiple of π change the wave form of the pulses propagating in this two level system. Although, the pulses with even multiples of π are proven to be more stable, an illustration is the soliton pulse having an area of 2π that remain constant in shape and peak amplitude as they propagate through absorbing media [69]

This brings us to the question of π-pulses control scheme, a control technique that has attracted huge interest over the years [67] based on interaction times. According to the area theorem, a fully resonant π-pulse (i.e. $\Delta\omega = 0$) represents a field with a 180-degree rotation of its pseudo-polarization vector on the Bloch sphere (see, Ref [2, 68]) about an axis at a Rabi frequency, $\Omega_R(t)$. Assuming a two level atomic system (see Figure 2.4(a)) with all the population distributed in the presumed ground state $|a\rangle$ is illuminated by the field for a period of time, $\tau_p = {}^{\pi}/_{\Omega}$. After interaction, the atom will be completely driven to the excited state $|b\rangle$ due to the π rotation about that axis resulting in a complete inversion.

This means a π-pulse is a pulse that will completely transfer the population from one state to another and satisfies the area condition for the transition. A 2π-pulse will return the system back to its original ground state after making a complete Rabi cycle of population inversion. This concept is demonstrated in Figure 2.4 where multiples of π pulses are shown to make population transfers between the ground $|a\rangle$ and excited $|b\rangle$ states.

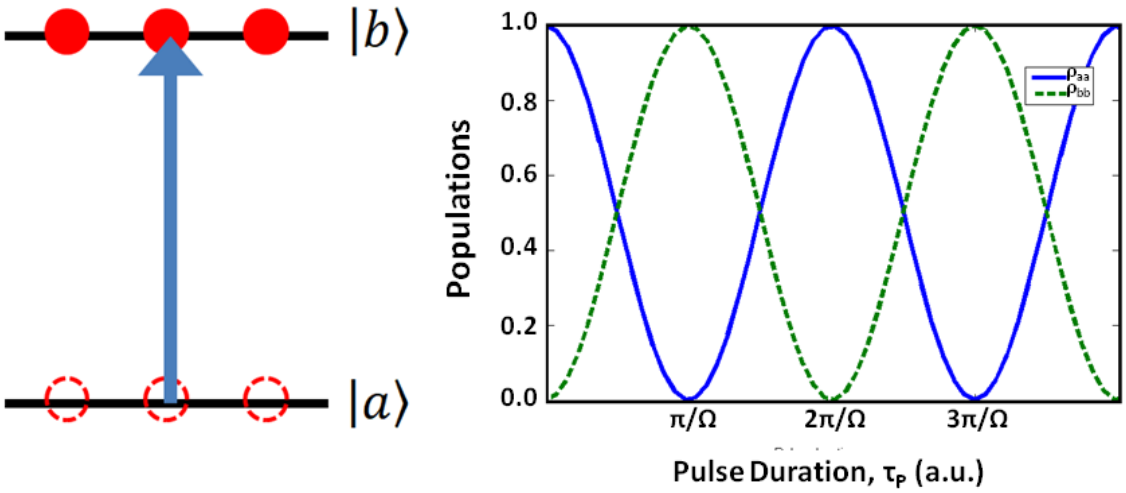

Figure 2.4: Rabi transfer between transitions in a two level system.

π-pulse control excitation scheme has been widely demonstrated to achieve optimal population transfer and even combined with other techniques like the adiabatic methods for transfer to highly excited states with single π-pulses [71 – 72].

At higher laser intensities, multiphoton processes using π-pulse scheme become possible [73] and have been used to demonstrate multiphoton interactions, more especially, the population of highly excited states and Rydberg states [74 – 76]. A major drawback is that these higher laser intensities produce large ac–Stark shifts, which move the energy levels of the interacting material in some way that amount to a form of detuning making it difficult to retain resonance [77]. This limitation can be averted by introducing multilevels by coupling the ground state to intermediate levels to achieve stronger coupling. Holthaus and Just [78] demonstrated a possible extension of the generalized π-pulse scheme to multilevel systems. Excitation using single and multiphoton pulses is shown in figure 2.5.

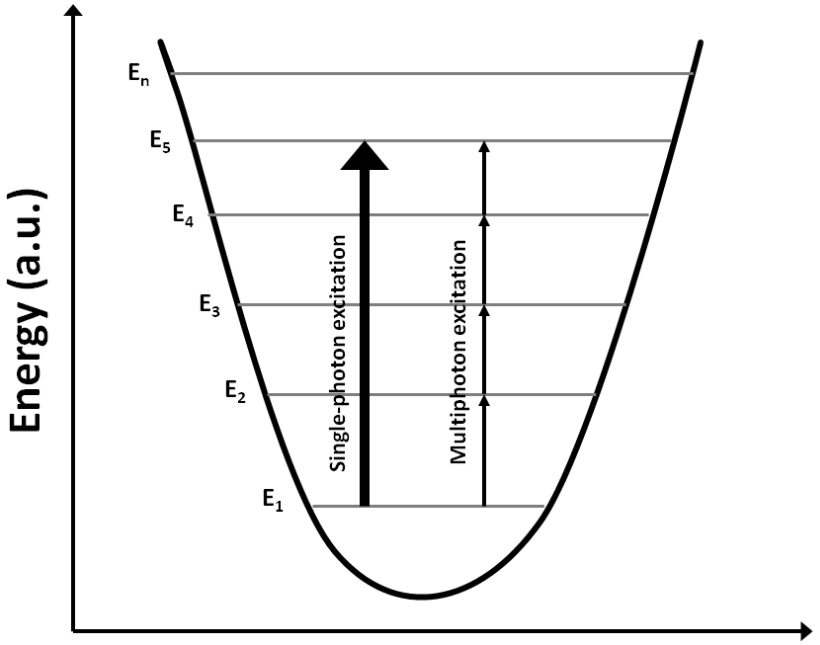

Figure 2.5: Demonstration of excitation of target vibrational states of a molecular system using a single pulse and Multiphoton pulse

2.3 Density Matrix (DM) Formalism

In this section, the density matrix formalism is described. First, we will take a look at the properties of the density operator and then we introduce the relaxation terms due to noise sources, collisions in gases and inhomogeneous broadening in an ensemble of atoms [79, 80]. Then, the density matrix in the Heisenberg picture is further considered, where the generalized Schrödinger equation (also known as the quantum Liouville or the Von-Neumann–Liouville equation) and the optical Bloch equations for the time evolution of the system is illustrated. Important physical quantities and approximations that can easily be introduced using the density matrix formalism are considered. Finally, the application to the simplest quantum system, a two-level system as it interacts with a coherent resonant or near-resonant light source is demonstrated. The application is further expanded to multilevels in subsequent chapters.

2.3.1 Properties of the density matrix

Density matrix is a semi-classical approach to understanding the interaction of ultrashort laser pulses with matter. The density matrix allows atomic and molecular systems to be classified as ensemble averages which is particularly convenient for most optically driven spectroscopic experiments. Reason is because unlike in the Schrödinger picture, where individual particles are prepared identically and requires an accurate aforementioned knowledge of the preliminary state of the system, these experiments are carried out on large ensembles of particles [81]. This is not the case for the density matrix as it surmises that the distribution of the system could initially be in different states, known as mixed states [80]. Practical examples are applications to statistical thermodynamics, where the distribution of molecules is due to Boltzmann probability function and thus, the molecules could initially be in different states [2, 80, 81]. Another example is complex systems like Oxazine [82, 83], where its modes could be summarized into fewer active modes and large number of reservoir modes. The concept of relaxation is easy to compute as these modes are coupled to each other and the statistical effect of the reservoir on the active mode is conveyed. For instance, in this study we summarized the levels of the system to a few active modes of a typical Oxazine system [84], See chapter 5.

As stated earlier one of the major advantages of the density operator is the possibility of describing both pure and mixed states. To fully describe the density matrix, we will start with the Schrödinger picture, using a wave function $|\Psi\rangle$ to describe a pure state and its evolution as seen in equation (2.24)

$$i\hbar\frac{d}{dt}|\Psi\rangle = \mathrm{H}|\Psi\rangle \qquad (2.24)$$

Where, the total Hamiltonian, H, is the sum of the unperturbed Hamiltonian, H_0 and the interaction part, H_I, i.e. $H = H_0 + H_I$. A good example to demonstrate this concept is a simple two level quantum system, having $|a\rangle$ as the ground state and $|b\rangle$ as the excited states, as seen in Figure 2.4(a). Therefore the wave function of the system can be written as:

$$|\Psi\rangle = P_a|a\rangle + P_b|b\rangle \qquad (2.25)$$

Where, P_a and P_b are the probability amplitudes for the ground and excited states. Also, it is worth taking into account that the sum of the modulus of the amplitudes is equal to 1, i.e.

$$|P_a|^2 + |P_b|^2 = 1 \qquad (2.26)$$

In the initial case where the system is free from interaction, the equation (2.24) will solely depend on the free Hamiltonian, H_0, which is:

$$H_0 = \sum_n \hbar\omega_n|n\rangle\langle n| \qquad (2.27)$$

By combining (2.24) with (2.27), the new equation becomes

$$i\hbar\frac{d}{dt}|\Psi\rangle = H_0|\Psi\rangle \qquad (2.28)$$

$$i\hbar\frac{d}{dt}|\Psi\rangle = \left[\sum_n \hbar\omega_n|n\rangle\langle n|\right]|\Psi\rangle \qquad (2.29)$$

The density operator can be introduced for a pure state as;

$$\rho = |\Psi\rangle\langle\Psi| \qquad (2.30)$$

$$|\Psi\rangle = \begin{pmatrix} P_a \\ P_b \end{pmatrix} \text{ and } \langle\Psi| = \begin{pmatrix} P_a^* & P_b^* \end{pmatrix} \qquad (2.31)$$

$$\rho = \begin{pmatrix} |P_a|^2 & P_a P_b^* \\ P_b P_a^* & |P_b|^2 \end{pmatrix} \qquad (2.32)$$

The density matrix is Hermitian i.e. $\rho^{*}_{mn} = \rho_{nm}$, therefore, substituting the density matrix elements for the probability amplitudes, we have

$$\rho = \begin{pmatrix} \rho_{aa} & \rho_{ba} \\ \rho_{ba} & \rho_{bb} \end{pmatrix} \qquad (2.33)$$

For mixed states, we have $\rho_{bb} = \sum_n Z_n |P_b|^2$, where the diagonal element, ρ_{bb} is a real positive integer representing the probability of the population of the upper state $|b\rangle$. The off-diagonal element $\rho_{ab} = \sum_n Z_n P_a P_b^*$ represents the coherent interference between the states, $|a\rangle$ and $|b\rangle$ and if $\rho_{ab} \neq 0$, it is considered to be the coherence between the states.

In the Heisenberg picture, a more generalized form is introduced representing the evolution equation of the time dependent density matrix, ρ(t)

$$\frac{d}{dt}\rho(t) = \frac{d}{dt}|\Psi\rangle\langle\Psi| + \frac{d}{dt}|\Psi\rangle\langle\Psi| \qquad (2.34)$$

$$\frac{d}{dt}\rho(t) = \frac{1}{i\hbar}H|\Psi\rangle\langle\Psi| + \frac{1}{i\hbar}|\Psi\rangle\langle\Psi|H \qquad (2.35)$$

Substituting equation (2.30) into (2.35), we get

$$\frac{d}{dt}\rho(t) = \frac{1}{i\hbar}(H\rho - \rho H) \qquad (2.36)$$

Written in terms of commutator defined for two operators $\hat{A}$ and $\hat{B}$ by $[\hat{A},\ \hat{A}] = \hat{A}\,\hat{B} - \hat{B}\,\hat{A}$, equation (2.36) becomes

$$\frac{d\rho}{dt} = \frac{1}{i\hbar}[H, \rho] \qquad (2.37)$$

As we already know ρ is the density operator and $H = H_0 + H_I$ is the total Hamiltonian. Equation (2.37) is known as the Quantum Liouville or Von-Neumann–Liouville equation.

One extra advantage of using the density matrix is its ability to estimate the expectation value of an observable quantity. Let's assume an observable, say Ø,

$$\langle Ø \rangle = \langle \Psi | Ø | \Psi \rangle \qquad (2.38)$$

$$\sum_{ab} \mathrm{P}_a \mathrm{P}_b^* Ø_{ab} = \sum_{ab} \rho_{ab} Ø_{ab} \qquad (2.39)$$

$$\overline{\langle Ø \rangle} = \mathrm{Tr}\{\rho Ø\} \qquad (2.40)$$

As in the case of molecular system interaction, the density matrix can be described as the trace over the reservoir modes [79 – 81, 85].

2.3.2 Light-Matter Interaction using the DM Formalism

The Von-Neumann–Liouville equation was introduced in the previous section (equation (2.37)). Imagine a condition where the 2-level system interacts with an excitation field, unlike the case of equation (2.28), the total Hamiltonian will involve both the free and interaction parts, i.e. $H = H_0 + H_I$. A further look at the interaction part of the total Hamiltonian, we have

$$H_I = -\vec{\mu} \cdot \vec{E} \qquad (2.41)$$

Where, $\vec{\mu}$ is the transitional dipole moment matrix element and $\vec{E}$ is the electric component of the excitation pulse described as $\vec{E} = E_0 \cos \omega t = \frac{1}{2}\left(e^{-i\omega t} + e^{i\omega t}\right)E_0$.

Recall, the Rabi frequency is given as $\Omega_R(t) = \mu E_0/\hbar$. Hence, introducing Ω, we have $H_I = -\frac{\hbar}{2}(\rho_{ab} + \rho_{ba})\left(e^{-i\omega t} + e^{i\omega t}\right)\Omega$. From the previous equation we can see that the slowly varying off-diagonal density matrix elements fluctuate in time with $e^{-i\omega_{ab}t}$ and $e^{i\omega_{ab}t}$. Hamiltonians oscillate containing components that fluctuate rapidly with frequency, $\omega + \omega_{ab}$ and the reverse sign of these components fluctuate slowly with frequency, $\omega - \omega_{ab}$

[80, 86]. In the framework of the Rotating wave approximation (RWA), we neglect the fast oscillating terms in the effective Hamiltonian and keep the slowly oscillating terms. The RWA is used in Chapter 5 for studying Oxazine systems with low intensity pulses. However, the majority of the thesis employs the density matrix equations integrated beyond the RWA to account for the entire Fourier components of the interaction pulses in the case of intense ultrashort pulses.

2.3.3 Density Matrix Time Evolution Equations

The time evolution equations, also referred to as the optical Bloch equations, represent the dynamics of the quantum system and illustrate how the system interacts with light. First, we consider a case where the pulse duration is far shorter than any form of relaxation emerging in the system, i.e. $\tau_p << T_1, T_2$, thereby neglecting relaxation [80], imputing all physical parameters and substituting $e^{i\omega t}\rho_{ab}$ with $\tilde{\rho}_{ab}$ and $\frac{d}{dt}\rho_{ab}$ with $\dot{\rho}_{ab}$ we have [86]:

$$\dot{\rho}_{aa} = \frac{iE(t)}{\hbar}\{\mu_{ab}(\tilde{\rho}_{ba} - \tilde{\rho}_{ab})\}$$

$$\dot{\rho}_{bb} = -\frac{iE(t)}{\hbar}\{\mu_{ab}(\tilde{\rho}_{ba} - \tilde{\rho}_{ab})\} \qquad (2.42)$$

$$\dot{\rho}_{ab} = -i\omega_{ab}\tilde{\rho}_{ab}\frac{iE(t)}{\hbar}\{\mu_{ab}(\rho_{bb} - \rho_{aa})\}$$

In a situation where the relaxation processes are relevant and having times close to the pulse duration, we consider their effects on the evolution of the system as it undergoes interaction. One of the major advantages of the density matrix as stated earlier is the convenience in introducing the relaxation terms [79, 81] which includes the relaxation and decoherence effects arising from numerous sources including spontaneous emission.

Assume our 2-level system (Figure 2.6), an excited state $|b\rangle$ experiences an exponential decay over time to the ground state at a rate given by γ_{ba}. This means $T_1 = {}^1/_{\gamma_{ba}}$ becomes the

lifetime of that energy level $|b\rangle$ and is referred to as the population relaxation time, as it is the time taken for the population to leave the upper level to the ground state [80].

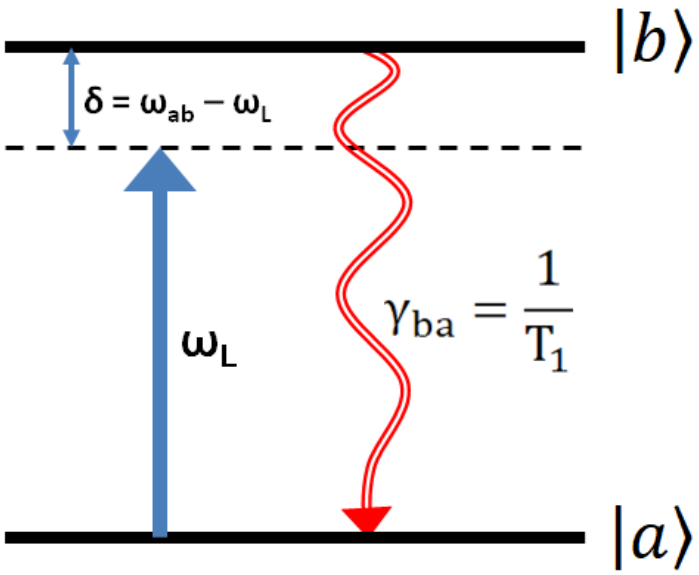

Figure 2.6: 2-level system demonstrating population decay terms γ_{ba}

Apart from the decay, an extra addition to the relaxation is observed as atomic dipole moment oscillates and slowly decays to zero. This type of decay of the off-diagonal terms does not necessarily affect the populations but reduces the coherences between the two states and is referred to as the dephasing [81]. The dephasing rate $\bar{\Gamma}_{ab}$ is given as $\frac{\gamma_{ba}}{2} + \Gamma_{ab}$, where Γ_{ab} is the purely dephasing rate. The dephasing time, $T_1 = {}^1/_{\bar{\Gamma}_{ab}} = {}^1/_{[\frac{\gamma_{ba}}{2} + \Gamma_{ab}]}$ and is widely depicted to be shorter than T_1 (i.e. $T_2 < T_1$) [80].

Incorporating parameters like the decay and dephasing rates, γ_{ba} and $\bar{\Gamma}_{ab}$ and the detuning, $\delta = \omega - \omega_{ab}$ into the time evolution equations, we have

$$\dot{\rho}_{aa} = -\gamma_{ba}\rho_{aa} + \frac{iE(t)}{\hbar}\{\mu_{ab}(\tilde{\rho}_{ba} - \tilde{\rho}_{ab})\}$$

$$\dot{\rho}_{bb} = \gamma_{ba}\rho_{aa} - \frac{iE(t)}{\hbar}\{\mu_{ab}(\tilde{\rho}_{ba} - \tilde{\rho}_{ab})\} \qquad (2.43)$$

$$\dot{\rho}_{ab} = (i\delta - \bar{\Gamma}_{ab})\tilde{\rho}_{ab} + \frac{iE(t)}{\hbar}\{\mu_{ab}(\rho_{bb} - \rho_{aa})\}$$

2.3.4 Numerical Implementation

Assume a completely resonant π-pulse with a wavelength of 800nm interacts with a two level system with a full width at half maximum, τ_{FWHM} of 5fs. Assuming all populations are initially in the ground state, a complete population transfer can be demonstrated as shown in Figure 2.7 using the aforesaid pulse with area, $\theta = \int_{-\infty}^{\infty} \Omega(t) d\tau = n\pi$ having a Gaussian profile i.e. $E(t) = E_0 e^{-t^2/\tau_p{}^2}$ with pulse duration $\tau_p = \tau_{FWHM}/\sqrt{2\ln 2}$. We have $E_0 = n\frac{\pi\hbar}{\mu\tau_p\sqrt{\pi}}$ taking μ_{ab} as 4.2×10^{-29} Cm.

In figure 2.7(a) we have our 2-level model with the ground $|a\rangle$ and excited $|b\rangle$ states, Figure 2.7(b) shows the Gaussian pulse for n = 1. Figure 2.7 Figure 2.7(c) shows the complete population transfer with n = 1 and $E_0 = 1.048 \times 10^9$ V/m. (d) demonstrates a complete population transfer and depopulation to the ground state with n = 2 with $E_0 = 2.095 \times 10^9$ V/m.

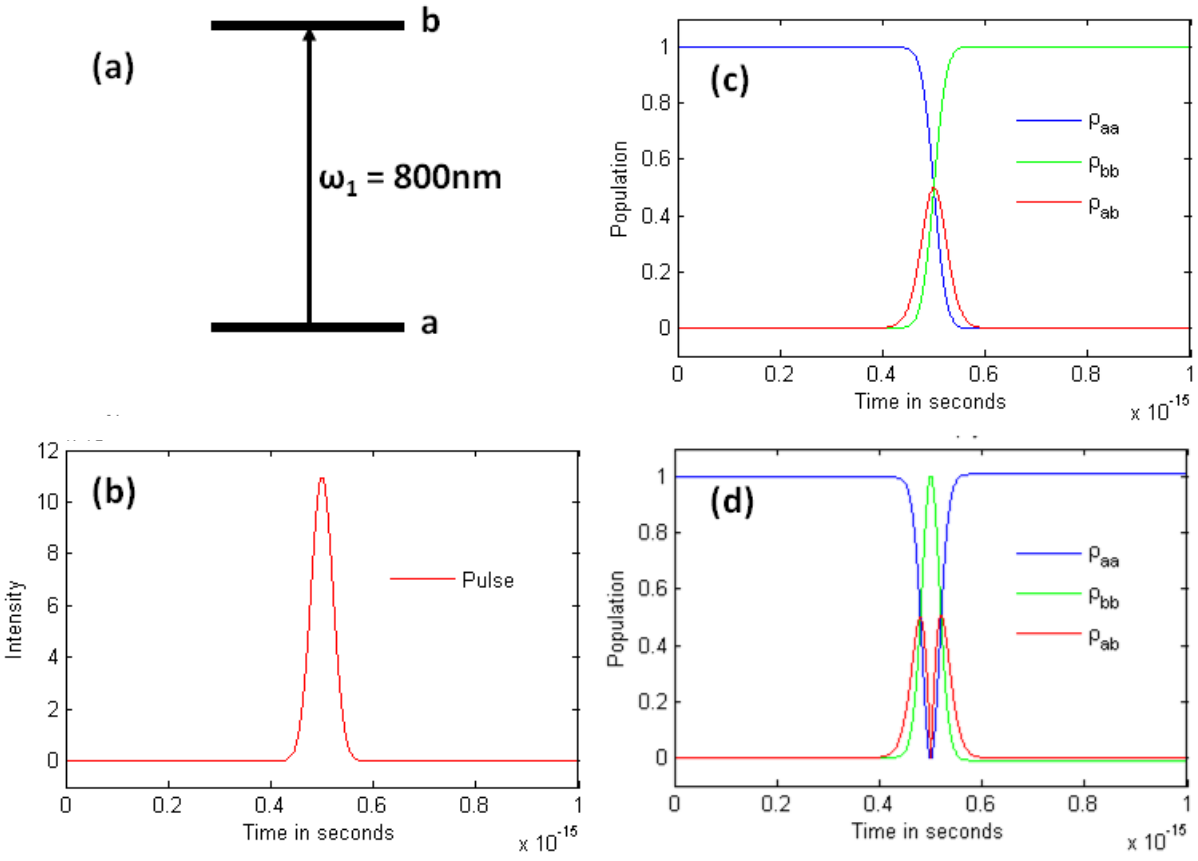

Figure 2.7: (a) 2-level system excited by a fully resonant π-pulse with a wavelength of 800nm (b) the Gaussian profile of the pulse with intensity in the order of 10^{11} W/cm^2 and E_0 = 1.048×10^9 V/m (c) Time evolution showing complete population transfer with the resonant π-pulse (d) Complete Rabi oscillation using a 2π-pulse, where the populations return completely back to the ground state b.

Chapter 3

Multiphoton π-pulse excitation schemes for Coherent Control

In this chapter, multiphoton π-pulse excitation scheme is presented as a more suitable alternative to single-photon excitation schemes for achieving enhanced selectivity and forestalling certain effects that hinder complete population inversion at higher laser intensities, thereby, optimizing the inversion in resonant and near-resonant cases. The chapter is divided into two main sections. The first section talks about the introduction of the polychromatic π-pulse scheme to a 3-level system, where a bi-chromatic π-pulse is used for excitation. The second part further extends this scheme to a 4-level system. In this work, the density matrix formalism is used to theoretically analyse the interaction of the bi- and tri-chromatic π-pulses with atomic sodium. Influence of key physical parameters like field detuning, pulse chirp and areas are demonstrated and discussed in detail.

3.1 Bichromatic π-pulse Scheme in a 3-Level System

In this section, extension of the density matrix formalism for population inversion in a 3-level system is demonstrated. The complete transfer is shown to be influenced by the field detuning and pulse chirp, specifically, the sign of the pulse chirp as demonstrated in the work of Serrat and Biergert [67]. First, a case of a bichromatic pulse in full resonance with the three-level system is considered, which the pulse area, i.e. $\theta = \int_{-\infty}^{\infty} \Omega(\mathrm{t}) d\tau = \sqrt{2}\pi$ as shown in Figure 3.1(a). After that, a near-resonant case is investigated where chirp and detuning is computed and the system is integrated beyond the RWA [67] as demonstrated in Figure 3.1(b).

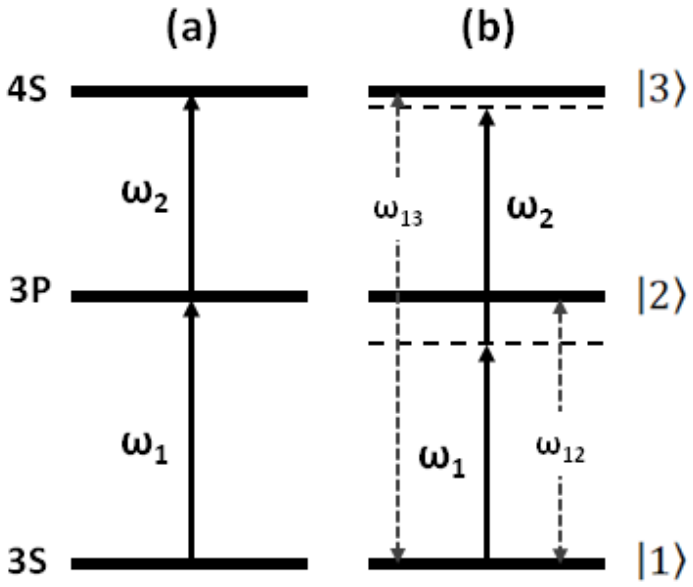

Figure 3.1: Schematic energy level configuration (Cascade configuration) (a) A fully resonant coherent interaction with the 3-level system. Here, the detunings, Δ_1 and $\Delta_2 = 0$ and pulse areas for each pulses are $\sqrt{2}\pi$ [15, 67]. (b) In a case where detuning and other parameters are considered. The detuning, Δ_1 is defined as $\omega_{12} - \omega_1$ and Δ_2 as $\omega_{13} - (\omega_1 + \omega_2)$, parameter values are shown in table 3.1.

3.1.1 System configuration

In the study, the control of atomic sodium is investigated and the energy levels of Na atoms are summarized to a 3-level system (Figure 3.1) with target excited state $|3\rangle$ representing the $4S_{1/2}$ state and the ground state $|1\rangle$, assumed to initially contain all the population, represents the $3S_{1/2}$ state. An intermediate level $|2\rangle$ is included between $|1\rangle$ and $|3\rangle$ which represents the $3P_{3/2}$ state in order to facilitate the two-photon excitation scheme. The goal is to completely steer the population from the $3S_{1/2}$ state to the $4S_{1/2}$ state as shown in Figure 3.2. In the case of Figure 3.1(a), the solution is completely analytical. Complete inversion using a bichromatic π-pulse can be achieved for resonant and near-resonant cases and is demonstrated in Figure 3.2 [13 – 15].

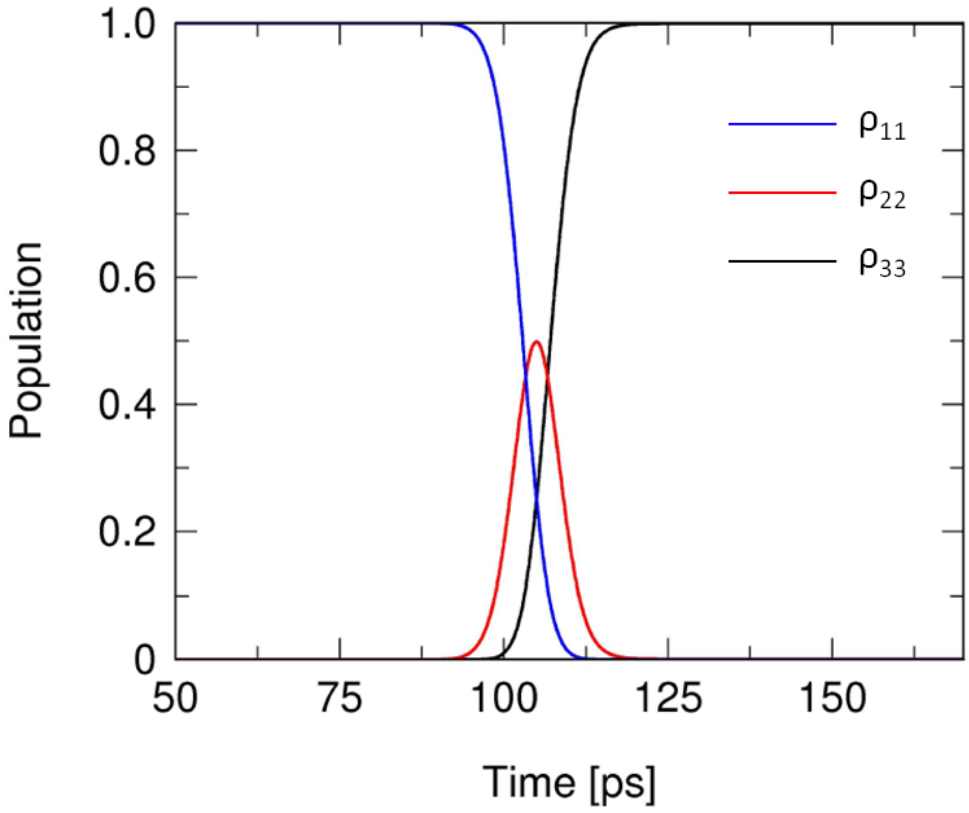

Figure 3.2: Complete population inversion achieved using optimal conditions for resonant and near-resonant cases [13 – 15].

In the case of near-resonant bichromatic laser pulses coherently interacting with the 3-level system (Fig 3.1(b)), certain physical parameters like chirp and detuning are considered, thereby creating a need for numerical integration of the system. The density matrix formalism is implemented without the RWA. It is considered that the interaction time, τ_p was shorter than any relaxation time of the system (i.e. $\tau_p << T_1, T_2$) thereby neglecting all decay T_1 and dephasing T_2 times.

3.1.2 Numerical Simulation and Physical Parameters

The non-perturbative time dependent density matrix equations for the 3-level system after neglecting all relaxation terms become equations (3.1(a) – (f));

$$\rho_{11} = \frac{iE(t)}{\hbar}\{\mu_{12}(\rho_{21} - \rho_{12})\}$$

$$\rho_{22} = \frac{iE(t)}{\hbar}\{\mu_{12}(\rho_{12} - \rho_{21}) + \mu_{12}(\rho_{32} - \rho_{23})\}$$

$$\rho_{33} = \frac{iE(t)}{\hbar}\{\mu_{23}(\rho_{23} - \rho_{32})\} \quad (3.1)$$

$$\rho_{12} = i\omega_{21}\rho_{12}\frac{iE(t)}{\hbar}\{\mu_{12}(\rho_{22} - \rho_{11}) - \mu_{23}\rho_{13}\}$$

$$\rho_{13} = i\omega_{31}\rho_{13}\frac{iE(t)}{\hbar}\{\mu_{12}\rho_{23} - \mu_{23}\rho_{12}\}$$

$$\rho_{23} = i\omega_{32}\rho_{23}\frac{iE(t)}{\hbar}\{\mu_{23}(\rho_{33} - \rho_{22}) - \mu_{12}\rho_{13}\}$$

3.1.3 Parameters Used

The diagonal terms ρ_{ii} (i.e. ρ_{11}, ρ_{22}, ρ_{33}) represent the populations of the different levels $|1\rangle$, $|2\rangle$ and $|3\rangle$ respectively while the off-diagonal terms, terms ρ_{ij} (i.e. $\rho_{12}, \rho_{13}, \rho_{23}$) are the coherences between the corresponding levels. μ_{ij} are the dipole coupling coefficients that correspond to the allowed transitions, and $\omega_{ij} = |E_j - E_i|/\hbar$ are the angular frequencies of the transitions, E_i and E_j represent the energies of their equivalent quantum states. The bichromatic pulse is considered to be a Gaussian pulse having two components with the total electric field E(t) being the sum of both components, $E_1(t)$ and $E_2(t)$ as shown in equation (3.2)

$$E(t) = E_1(t) + E_2(t) = e^{-(t/\tau)^2}\{E_{01}\cos(\omega_1 t) + E_{02}\cos(\omega_2 t)]\} \quad (3.2)$$

Where, the components $E_1(t)$ and $E_2(t)$ have peak amplitudes, E_{01} and E_{02}, and angular frequencies of , ω_1 and ω_2 respectively. Both components are considered to have the same duration $\tau_p = {\tau_{FWHM}}/{\sqrt{2\ln 2}}$. In the work of Serrat and Biergert [67], they show that a complete population inversion to $4S_{1/2}$ state [Figure 3.2] using the bichromatic pulse can be achieved with optimal parameters as in table 3.1 [67] without considering the effects of chirp.

Table 3.1: Optimal parameters for population inversion [67]

Parameters definition and unit	Value
Central wavelengths, ω	ω_1= 16978 cm^{-1} (589 nm) ω_2= 8762 cm^{-1} (1141 nm)
Peak amplitudes, E_i	E_1= 3.25 × 10^6 V/m E_2= 4.34 × 10^6 V/m
Atomic transitional dipole coupling coefficient, μ_{ij}	$\mu_{12} = \mu_{23}$ = 1.85 × 10^{-29} Cm
Pulse duration, τ_p	τ_p = 10 ps

In order to thoroughly understand the control of population inversion process in the chosen atomic system, chirp is taken into account. The chirp parameters a_1 and a_2 are included into the equation (3.3) as a_i/τ^2 to give

$$E(t) = e^{-(t/\tau)^2}\left\{E_{01}\cos[\omega_1 t - a_1\left(\frac{t}{\tau_p}\right)^2] + E_{02}\cos[\omega_2 t - a_2\left(\frac{t}{\tau_p}\right)^2]\right\} \qquad (3.3)$$

3.1.4 Results and Discussion

Introducing chirped pulses are beneficial in reducing peak intensity by broadening pulse duration to avoid certain effects that could limit population inversion with π-pulse control scheme [2, 70]. Studies show that coherent population transfer strongly depends on the pulse chirp, especially the chirp sign [87]. A positive up-chirped pulse (i.e. $a_i > 0$) can always invert more population than a negative down-chirped pulse (i.e. $a_i < 0$), so a positive-chirp can prove advantageous over a TL or negatively chirped pulse especially in molecular

excitation [70]. The influence of chirp is demonstrated where a combination of chirp parameters is studied to see its influence on the population inversion as shown in the contour map in Figure 3.3(a). In a case where both pulse chirps are positive there is a substantial enhancement of the population as compared to cases where one or both chirp signs are negative. The optimal transfer condition is seen with TL pulse where $a_1 = a_2 = 0$ achieving a complete transfer to $4S_{1/2}$ state with $\rho_{33} = 1$. A diagonal cut was used to simplify the results in the contour map as shown in Figure 3.3(b).

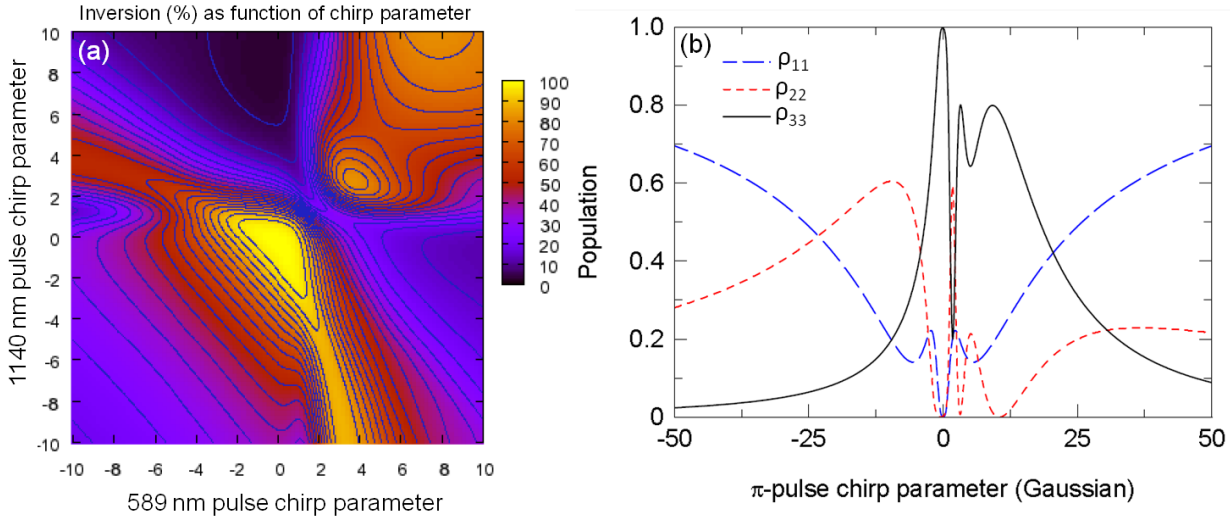

Figure 3.3: (a) Final population ρ_{33} (in %) as a function of the adimensional chirp parameter for the 589 nm (a_1) and the 1140 nm (a_2) bichromatic pulse components. For instance, a_i = 10 represents a chirp value of ≈ 0.14 ps^{-2}. (b) Final populations values for ρ_{11}, ρ_{22} and ρ_{33} as a function of the chirp parameter (in units of τ^{-2} i.e. 2ln 2/100ps^2) for $a_1 = a_2$. [**Source:** Ref 67]

The chirp influence on the population inversion can also be controlled by detuning the field excitation. The study can readily be extended to more complex multilevel systems for example, to a 4-level system of atomic sodium [88], which will be discussed in the section 3.2.

3.2 Trichromatic π-pulse Scheme in a Four Level System

The concept of polychromatic excitation using resonant or near-resonant π-pulses has been shown to achieve complete transfer to target states with demonstrations in three-level systems [13 – 14, 67, 89 – 98] and even to four-level systems with transfer schemes that combine the π-pulse method with adiabatic techniques [99]. Unlike, the two-photon excitation of a 3-level system, analytically solving differential equations of multilevel quantum systems interacting with coherent multiphoton excitation can be a complex task that often leads to expressions that lack any physical insight. This creates a need for the development of efficient numerical algorithms for the general solution of these systems [2].

In this work, a numerical solution for complete population inversion in a four-level ladder type system using a full π-pulse excitation scheme with completely resonant ultrashort phase-locked Gaussian laser pulses is presented. The full π-pulse scheme is preferred to the adiabatic method as they prove to be energetically more efficient as the intensities required for optimal excitation are on the order of the intensities for resonantly pumped single-photon transitions. A set of pulse area, $\theta = \int_{-\infty}^{\infty} \Omega(\mathrm{t}) d\tau$, is found to achieve complete population inversion in the chosen target state. The effects of detuning and chirp of the laser pulses on the complete transfer are studied using ultrashort pulses with durations in the order of pico- (ps) and femtosecond (fs) timescales.

3.2.1 System Configuration

Here, we demonstrate control of atomic systems extended to 4-levels using atomic sodium as the case study. The level structure chosen in this case corresponds to the energy levels of Sodium atoms, where the ground state $|1\rangle$ represents the $3S_{1/2}$ state, the intermediate states

$|2\rangle$ and $|3\rangle$ represent $3P_{1/2}$ and $4S_{1/2}$ respectively and the target upper state $|4\rangle$ is the 7P state. The goal is to completely drive all the populations, which are assumed to be in the ground state 3S to the 7P state. The transitional dipole moments μ_{ij} to couple these different levels are $\mu_{3s-3p} = 2.11 \times 10^{-29}$Cm, $\mu_{3p-4s} = 2.09 \times 10^{-29}$Cm, $\mu_{4s-7p} = 1.32 \times 10^{-30}$Cm, with the lifetimes in the order of nanoseconds.

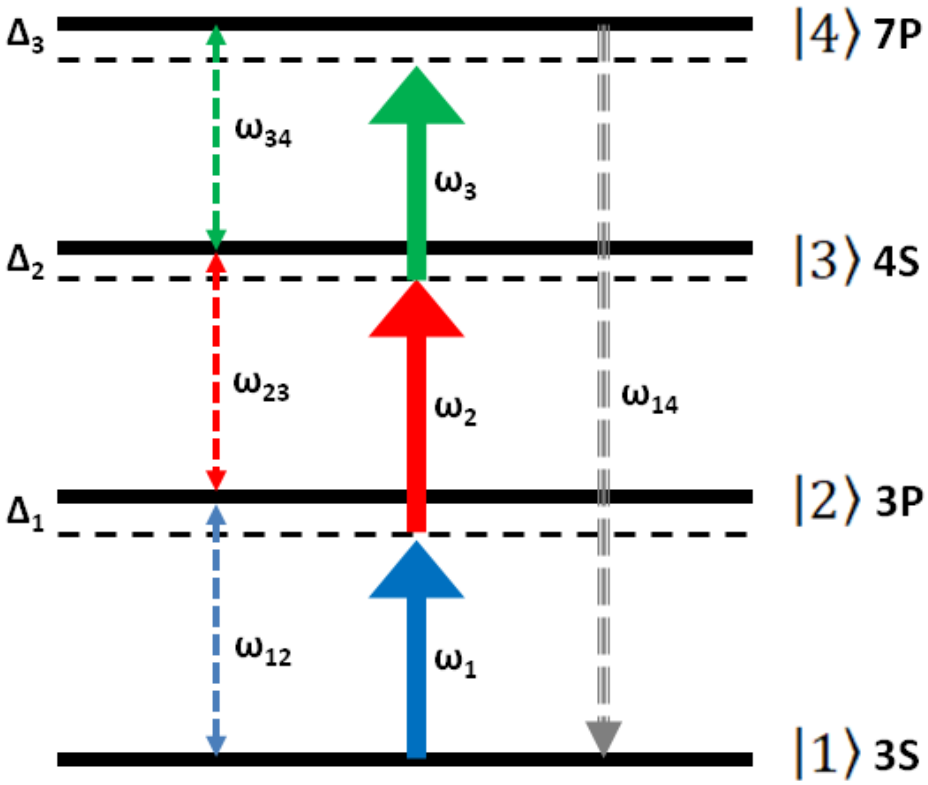

Figure 3.4: Energy level of atomic sodium showing the detuning parameters definitions discussed in section 3.2.5 II. An exponential decay from 7P to 3S states leads to a generation of UV radiation of 259 nm (ω_{14}).

3.2.2 Numerical Simulation

The Liouville equation was numerically solved for the 4-level cascade configuration shown in figure 3.4 when the system is in interaction with a trichromatic π-pulse. The density matrix equations are solved beyond the rotating wave approximation. Assumption beyond the RWA

enables the density matrix analysis to account for interaction of all the Fourier components of the pulses with all the permitted transitions in the system, and therefore in the study, the effects of large detuning and chirp of ultrashort pulses with a broad range of intensities can be evaluated. We take into account the relaxation terms, although which does not have much influence on the expected results as the interacting field has a duration of ps and fs while our decay times are in the order of ns. The final equations representing the dynamics of the system undergoing interaction are:

$$\dot{\rho}_{22} = -\gamma_{22}\rho_{22} + \gamma_{32}\rho_{33} + \gamma_{42}\rho_{44} + i\frac{E(t)}{\hbar}(\mu_{12}(\rho_{12} - \rho_{21}) + \mu_{23}(\rho_{32} - \rho_{23}))$$

$$\dot{\rho}_{33} = -\gamma_{33}\rho_{33} + \gamma_{43}\rho_{44} - i\frac{E(t)}{\hbar}(\mu_{23}(\rho_{32} - \rho_{23}) + \mu_{34}(\rho_{34} - \rho_{43}))$$

$$\dot{\rho}_{44} = -\gamma_{44}\rho_{44} + i\frac{E(t)}{\hbar}(\mu_{14}(\rho_{14} - \rho_{41}) + \mu_{34}(\rho_{34} - \rho_{43}))$$

$$\dot{\rho}_{11} = -\dot{\rho}_{22} - \dot{\rho}_{33} - \dot{\rho}_{44} \tag{3.4}$$

$$\dot{\rho}_{12} = -\bar{\Gamma}_{12}\rho_{12} + i\omega_{12}\rho_{12} + i\frac{E(t)}{\hbar}(\mu_{12}(\rho_{22} - \rho_{11}) + \mu_{14}\rho_{24}^{*} - \mu_{23}\rho_{13})$$

$$\dot{\rho}_{13} = -\bar{\Gamma}_{13}\rho_{13} + i\omega_{13}\rho_{13} + i\frac{E(t)}{\hbar}(\mu_{12}\rho_{23} - \mu_{23}\rho_{12} + \mu_{14}\rho_{34}^{*} - \mu_{34}\rho_{14})$$

$$\dot{\rho}_{14} = -\bar{\Gamma}_{14}\rho_{14} + i\omega_{14}\rho_{14} + i\frac{E(t)}{\hbar}(\mu_{14}(\rho_{44} - \rho_{11}) - \mu_{34}\rho_{13} + \mu_{12}\rho_{24})$$

$$\dot{\rho}_{23} = -\bar{\Gamma}_{23}\rho_{23} + i\omega_{23}\rho_{23} + i\frac{E(t)}{\hbar}(\mu_{23}(\rho_{33} - \rho_{22}) - \mu_{34}\rho_{24} + \mu_{12}\rho_{13})$$

$$\dot{\rho}_{24} = -\bar{\Gamma}_{24}\rho_{24} + i\omega_{24}\rho_{24} + i\frac{E(t)}{\hbar}(\mu_{12}\rho_{14} - \mu_{14}\rho_{12}^{*} + \mu_{23}\rho_{34} - \mu_{34}\rho_{23})$$

$$\dot{\rho}_{34} = -\bar{\Gamma}_{34}\rho_{34} + i\omega_{34}\rho_{34} + i\frac{E(t)}{\hbar}(\mu_{34}(\rho_{44} - \rho_{33}) + \mu_{23}\rho_{24} - \mu_{14}\rho_{13}^{*})$$

3.2.3 Simulation Parameters

ρ_{ii} are the populations of the levels i, the off-diagonal elements ρ_{ij} represent the coherences between levels i and j, μ_{ij} are the dipole coupling coefficients of the corresponding electronic

transitions, and $\omega_{ij} = \left|E_j - E_i\right|/\hbar$ are the angular frequencies of the transitions $i - j$, with E_i being the energies of the corresponding quantum states. The decay rates of the transitions $i - j$ are given by γ_{ij} and the population relaxation rates of the levels satisfy $\gamma_{22} = \gamma_{21}$, $\gamma_{33} = \gamma_{31} + \gamma_{32}$, $\gamma_{44} = \gamma_{41} + \gamma_{42} + \gamma_{43}$. The overall rate γ_{ii}, which is inversely proportional to the population decay time T_1 of level i ($T_1 = {\gamma_{ii}}^{-1}$), is thus given by the sum of each deactivation pathway in the four-level system. The decay rates of the coherences are defined by $\overline{\Gamma}_{12} = \frac{\gamma_{22}}{2} + \Gamma_{12}$, $\overline{\Gamma}_{13} = \frac{\gamma_{33}}{2} + \Gamma_{13}$, $\overline{\Gamma}_{14} = \frac{\gamma_{44}}{2} + \Gamma_{14}$, $\overline{\Gamma}_{23} = \frac{(\gamma_{22}+\gamma_{33})}{2} + \Gamma_{23}$, $\overline{\Gamma}_{24} = \frac{(\gamma_{22}+\gamma_{44})}{2} + \Gamma_{24}$, and $\overline{\Gamma}_{34} = \frac{(\gamma_{33}+\gamma_{44})}{2} + \Gamma_{34}$, which include the relaxation of the coherences and the pure coherence dephasing rates Γ_{ij}, which are defined as the inverse of the corresponding pure coherence dephasing times and vice versa ($T_2 = {\Gamma_{ij}}^{-1}$). The laser pulses used in our simulations are of Gaussian shape, with the electric field E(t) given by

$$E(t) = E_1(t) + E_2(t) + E_3(t) = e^{-\left(\frac{t}{\tau}\right)^2}\{E_{01}\cos(\omega_1 t) + E_{02}\cos(\omega_2 t) + E_{03}\cos(\omega_3 t)]\}$$

Where, E_{01}, E_{02} and E_{03} are the peak amplitudes of the three pulse components $E_1(t)$, $E_2(t)$ and $E_3(t)$, and ω_1, ω_2, and ω_3, are the respective optical angular frequencies. The duration of the pulses is given by $\tau_p = {\tau_{FWHM}}\Big/{\left(\sqrt{2\ln 2}\right)}$, where τ_{FWHM} is the full width at half maximum of the pulse intensity profile. In the present study we consider ultrashort pulses of ps and fs durations, so that considering an effective dipole coupling coefficient such as $\mu \sim 10^{-29}$ Cm for all transitions, the peak intensities for 2π pulses of 10 ps and 100 fs durations result in $\sim 10^5$ W/cm^2 and $\sim 10^{10}$ W/cm^2 respectively. First a trichromatic pulse with a duration of 10 ps composed of three resonant components with central wavelengths of 589 nm, 1141 nm and 781 nm was considered and subsequently, other pulse duration were studied.

3.2.4 4-Level Pulse Area Calculation

The area of the pulse ($\theta(t) \equiv n\pi$) is of crucial importance in achieving selective population transfer. The equations (3.4) are numerically integrated using a 4 – 5 order Runge-Kutta based algorithm which scans the areas of the three pulse components $E_1(t)$, $E_2(t)$ and $E_3(t)$ between 0 to 4π in steps of 0.01π. The simulation is carried out using the optimal parameters stated above. The only possible solution established for complete population inversion to the desired target stae 7P from the ground state 3S is the set of pulse areas $\sqrt{3}\pi$, 2π and $\sqrt{3}\pi$ for $E_1(t)$, $E_2(t)$ and $E_3(t)$ respectively. The complete population transfer is demonstrated in Figure 3.5. From this figure, it can be seen that the intermediate levels 3P and 4S are momentarily populated during the course of excitation but the population is optimally transferred at the end of the interaction process. In order to estimate the accuracy, tests were done to vary the vary the pulse area of the $E_1(t)$ and $E_2(t)$ components by ±5%, it was observed that the population inversion in the 7P state was reduced to approximately 98% and could reduce even further to 90% depending on the pulse area combination. The final verification of the accuracy of this set of areas was doubling the area of each pulse to check for the complete 2π Rabi cycle, with all the population returning back to the initial state after interaction, which was obtained and shown in the inset of Figure 3.5.

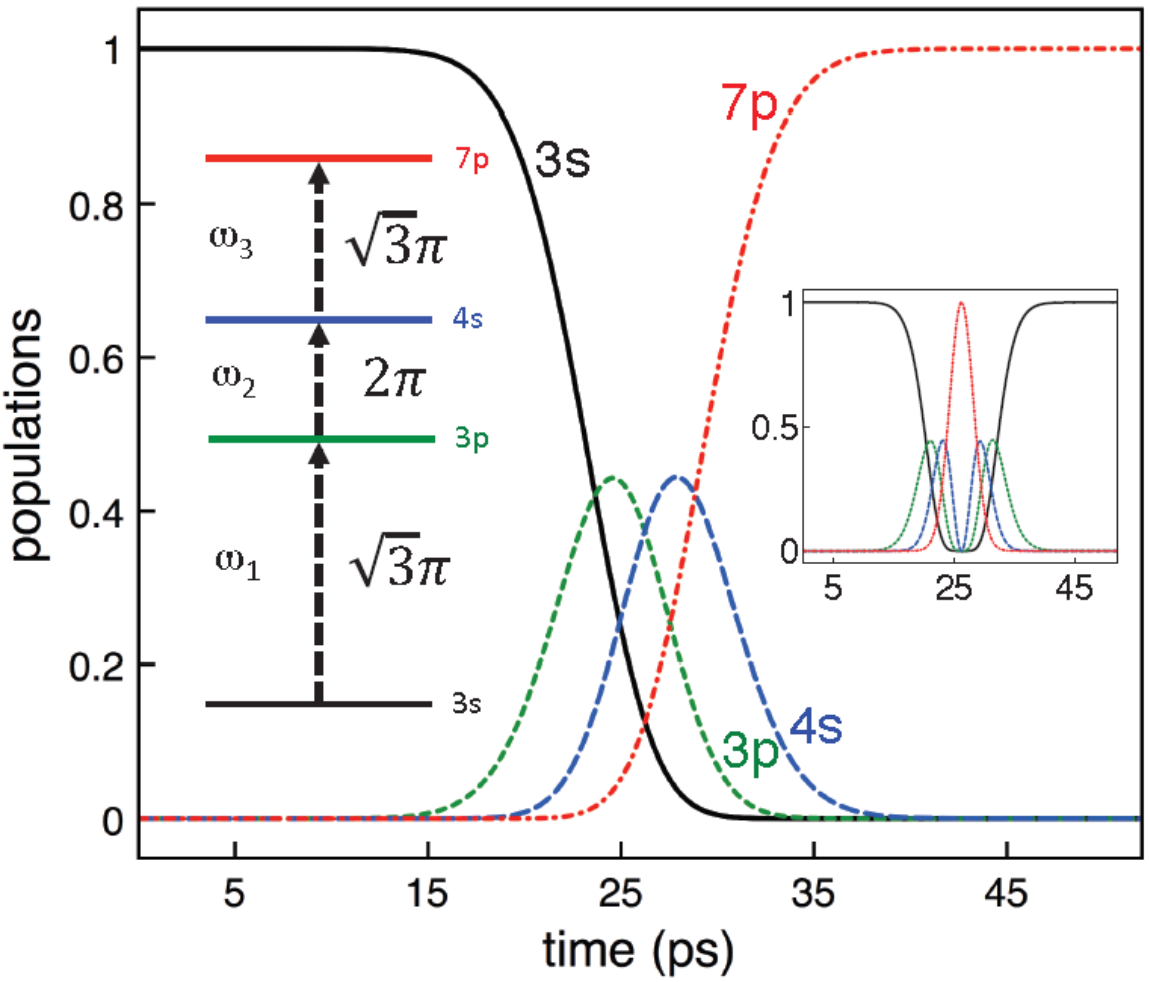

Figure 3.5: Time evolution of the populations of the four levels, as indicated, for a "π-pulse" transition produced by a tricolour resonant 10 ps Gaussian pulse of central angular frequencies ω_1, ω_2 and ω_3. The inset on the left shows a scheme of the four-level ladder system with the pulse areas that completely invert the population. Atomic sodium has been considered in our study as an example, with transition energies such as $\omega_{12} = \omega_1 = 16{,}978$ cm^{-1} (589 nm for 3s–3p), $\omega_{23} = \omega_2 = 8762$ cm^{-1} (1141 nm for 3p–4s), and $\omega_{34} = \omega_3 = 12{,}801$ cm^{-1} (781 nm for 4s–7p). The inset on the right shows a complete oscillation of a "2π-pulse", which is produced with the corresponding double pulse areas $2\sqrt{3}\pi$, 4π, and $2\sqrt{3}\pi$.

3.2.5 Results and Discussion

It was demonstrated in Figure 3.5 that a complete inversion of a target excited state in a 4-level ladder type system can be achieved and applied for other pulse durations shorter than 10 ps. As the areas are kept constant, some limitations to complete transfer using this scheme are observed and depend on some physical phenomena which will be looked at in detail.

I. Limitations of Study

The limitation of the results of our numerical solution is on the one hand dependent on the relaxation times and line broadening factors of the system which strongly limits the usability of long pulses. On the other hand, it depends on the combination of the value of the transitional dipole moments μ_{ij} and the pulse duration, τ_p, since weak coupling dipole moments with ultrashort pulses result in large peak intensities involving carrier field dynamics [100] and ac-Stark shifts that preclude the population inversion.

As an example, for values of the transition dipole moments in sodium as $\mu_{3s-3p} = 2.11 \times 10^{-29}$Cm, $\mu_{3p-4s} = 2.09 \times 10^{-29}$Cm, $\mu_{4s-7p} = 1.32 \times 10^{-30}$Cm, and considering 10 ps laser pulses, the peak intensity of the corresponding laser pulses stated earlier for $\sqrt{3}\pi$, 2π and $\sqrt{3}\pi$ illumination is $I_1 = 4.3 \times 10^5$ W/cm^2, $I_2 = 5.8 \times 10^5$ W/cm^2, $I_3 = 1.1 \times 10^8$ W/cm^2, which results in a population inversion to the 7p state of 99.3%. This population inversion is reduced to 98% for 5 ps pulses and to 84% for 1 ps pulses, which require pulse peak intensities of two more orders of magnitude. Dephasing times of the considered transitions in sodium are in general of the order of ns and therefore they do not influence the results obtained in the present study, which considers ps and fs pulses, but as commented above the complete density matrix equations including dephasing rates need to be computed for longer

pulses. An exponential decay from 7P to 3S states leads to a generation of UV radiation of 259 nm (ω_{14} in Figure 3.4).

II. Effect of Field Detuning

The robustness of the full π-pulse trichromatic scheme against detuning and chirp of the laser pulses is investigated by taking different durations into consideration. In order to study the effect of field detuning we define the following detuning parameters: $\Delta_1 = \omega_{12} - \omega_1$, $\Delta_2 = \omega_{12} + \omega_{23} - \omega_1 - \omega_2$ and $\Delta_3 = \omega_{12} + \omega_{23} + \omega_{34} - \omega_1 - \omega_2 - \omega_3$, with ω_{ij} corresponding to the energy transition of the i, j levels (1 = 3S, 2 = 3P, 3 = 4S, 4 = 7P, see Figure 3.4). Δ_3 = 0 corresponds to all field detunings that keep the three-photon resonance between levels 7P and 3S, Δ_2 = 0 means that the two-photon resonance between 3S and 4S is maintained, and Δ_1 = 0 means that the E_1 field is in resonance with the 3S–3P transition.

Figure 3.6 shows how complete population inversion from level 3S to level 7P is affected by detuning in the case of using 100 fs pulses. Figure 3.6(a) shows the results obtained when the three-photon resonance between 3S and 7P is kept (Δ_3 = 0). In the case shown in Figure 3.6(b) the two-photon resonance between 3S and 4S is maintained while the frequency of the three pulses is varied (Δ_2 = 0). In Figure 3.6(c) the results corresponding to having resonance in the lowest transition 3S–3P are shown (Δ_1 = 0). In these three first cases we observe a roughly symmetrical geometry around the centre of the figure where the detuning is zero (Δ_1 = Δ_2 = Δ_3 = 0), which shows the sensitivity of the complete inversion effect.

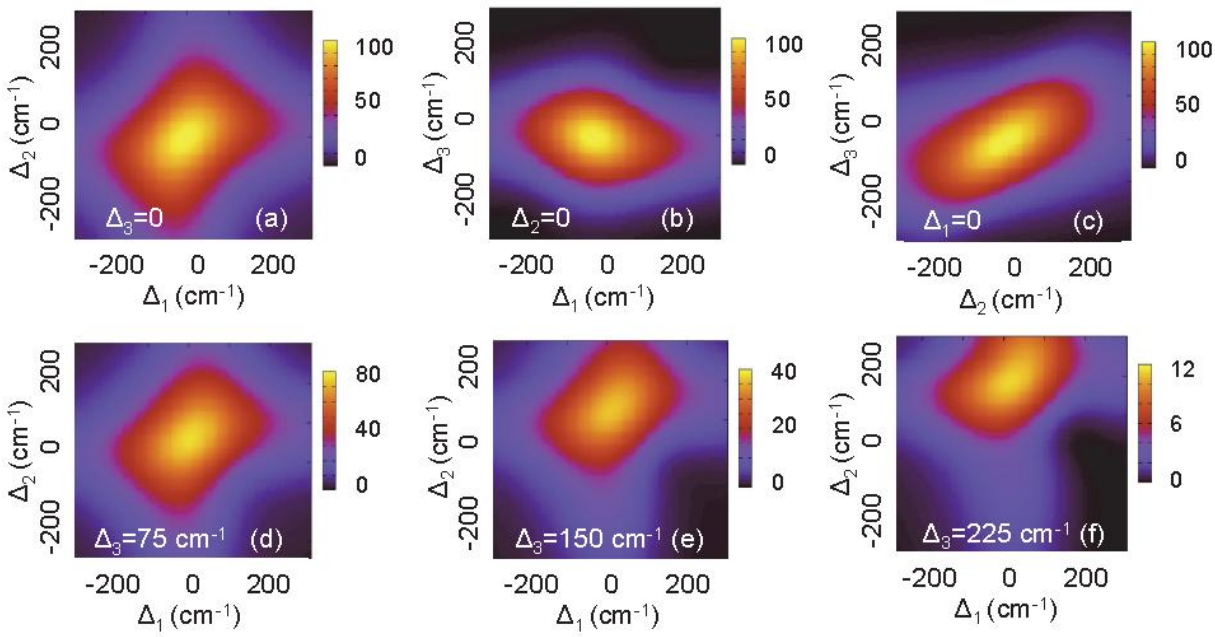

Figure 3.6: Study of the effect of field detuning on the population inversion from level 3s to level 7p in atomic sodium (see Figure 3.5) for 100 fs pulses. Note that in (a–c) the most yellow regions correspond to 100% population transfer; while in (d–f), they correspond to 80%, 40% and 12%, respectively.

.

We observe that for inversion to stay at values larger than 95% the system supports detuning of the order of about 100 cm^{-1}, which roughly corresponds to the width of the Gaussian 100 fs pulses used (147 cm^{-1}). In Figure 3.6(d)–(f) the three detuning parameters have been varied simultaneously. Figure 3.6(d) shows that for Δ_3 = 75 cm^{-1} a comparable detuning Δ_2 produces a population inversion as high as 80%. The combined effect of Δ_2 and Δ_3 is further shown in Figure 3.6(e) for a higher value of Δ_3 = 150 cm^{-1}, where a corresponding higher value of Δ_2 reduces the inversion to about 40%. For larger values of Δ_3 population inversion is basically suppressed, as it is shown in Figure 3.6(f), where the yellow colour in the plot represents only a 12% of inversion. For longer pulses the supported detuning is scaled accordingly with the duration of the pulses, as it was also reported in the case of a three-level system interacting with two phase-locked pulses [101]. This is, if a factor *m* is multiplied to the duration of the

pulse, the same factor *m* divides the scale of the supported detuning, which concurs with the fact the detuning should be comparable to the spectral width of the pulses. The optimal pulse duration for a particular application and the corresponding effect of detuning will therefore be dependent basically on the line-broadening factors of the system under consideration and the value of the dipole moments of the transitions, which for ultrafast population inversion have to be high enough not to involve too strong laser fields, as commented above.

III. Effect of Pulse Chirp

The pulse chirp on the three pulses interacting with the four-level system was considered and its effect for different transform limited (TL) pulse durations has been computed. In Figure 3.7 the effect of pulse chirp on the final populations is shown. The populations of the four levels after the pulse interaction are plotted as a function of the spectral chirp parameter φ'', which has been implemented in the Fourier domain as $\varphi(\omega) = 0.5\,\varphi''(\omega_l - \omega_0)^2$, with φ(ω) being the GDD added to the spectral phase of the pulse. Note that, as only the spectral phase of the laser pulse is varied in the study, the frequency content remains as the TL pulse for any value of the spectral chirp φ''. Recall that the time broadening of the pulse caused by chirp is given by $\tau_{p_c} = \sqrt{\tau_p{}^4 + 16\,(\ln 2)^2 \varphi''^2/\tau_\mathrm{p}}$, where, τ_{p_c} is the FWHM of the chirped pulse intensity profile [2], and therefore the regular effect produced by for instance propagating the laser pulse in a linear dispersive medium has been implemented. For GDD measurements of atmospheric and other gases with ultrashort pulses see, e.g., [102].

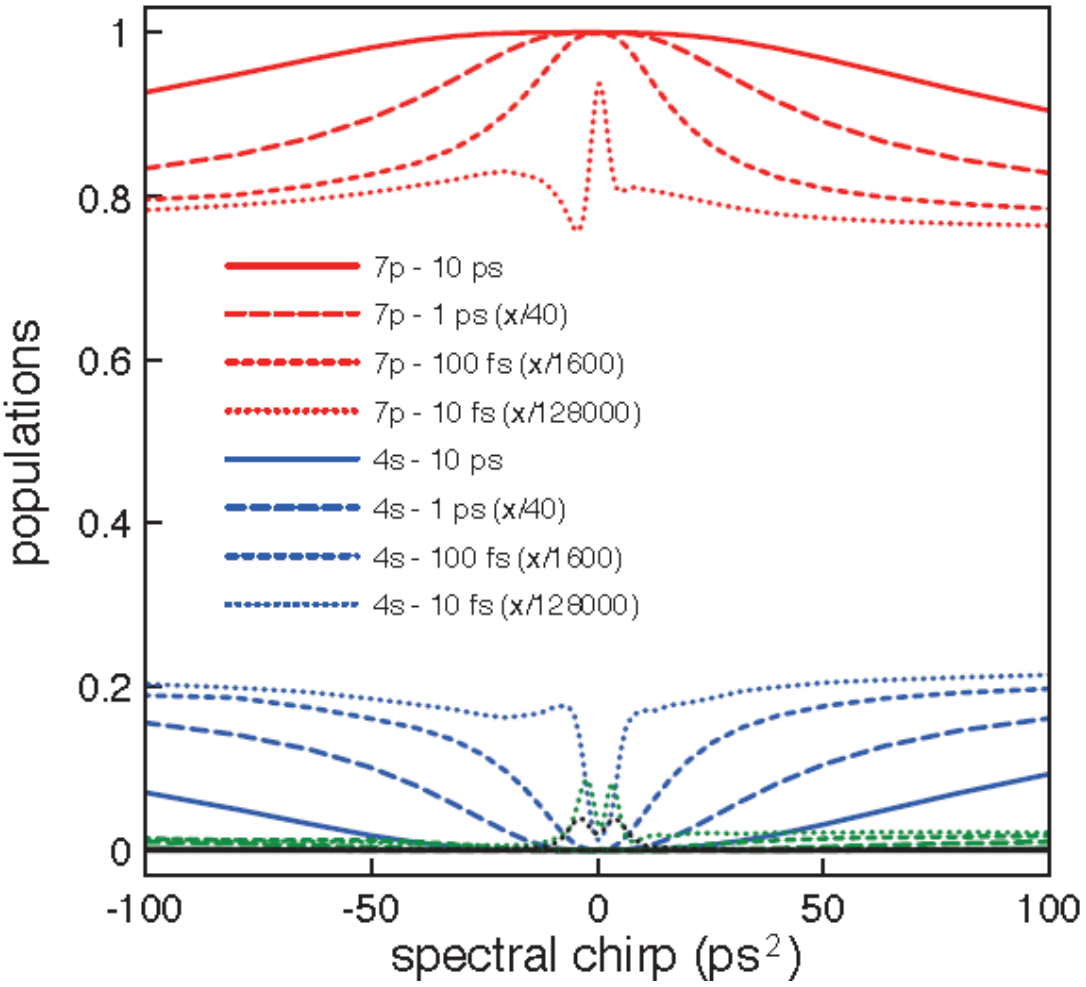

Figure 3.7: Effect of pulse chirp φ'' on the populations of the four levels after the interaction for different durations of the corresponding TL pulses. Indicated are the final populations of levels 7p (red lines) and 4s (blue lines); levels 3p and 3s become basically unpopulated in all cases (green and black lines). Note that the x-axis has been scaled for the different cases as indicated in the legend of the figure. Clearly, the population inversion produced by the longer pulses is less affected by chirp.

Table 3.2: Effect of Group Delay Dispersion

τ_p	φ''	τ_{p_c}	% Inversion
10 ps	100 ps^2	29.5 ps	≈ 92%
1 ps	0.94 ps^2	2.8 ps	≈ 92%
100 fs	9765 fs^2	289 fs	≈ 92%

In this study, the same amount of spectral chirp for the three frequency components of the interacting pulse have been considered and implemented with central frequencies resonant to their closest transition ($\omega_1 = \omega_{12}$, $\omega_2 = \omega_{23}$, $\omega_3 = \omega_{34}$). The red lines in Figure 3.7 correspond to the final population in level 7P, the blue lines show the final population in level 4S, and the green and black lines (close to zero) are the final populations in levels 3P and 3S. It is clear from Figure 3.7 that the main effect of pulse chirp in the case that we have considered is to bring part of the final population to level 4S, while levels 3P and 3S remain basically unpopulated. Note that the x-axis in Figure 3.7 has been scaled for the different pulse durations, as it is indicated in the legend of the figure. We observe that the trichromatic π-pulse effect is robust for spectral chirps of the order of ps^2 for TL pulses of 10 ps. In table 3.2 we show the GDD (φ'') values supported for the pulses with TL durations of tp = 1 ps, 10 ps and 100 fs for a reduction in the population inversion to values of ≈ 92%, together with the associated pulse broadening (τ_{p_c}). Clearly, the shorter pulses support a lower value of chirp, with a pulse broadening that corresponds roughly to three times the TL duration for the three cases. We finally observe that the large electric fields associated to shorter pulses of the considered pulse areas prevent complete population inversion, as shown for the case of 10 fs pulses by the red-dotted line in Figure 3.7.

3.3 Conclusions

In conclusion, the complete population transfer to target excited states has been described using polychromatic π-pulse scheme for multilevel system. In this work, particularly, three and four level cascade system configurations were considered. It is shown how much this control technique is affected by field detuning and pulse chirp. The study covers a valuable range of parameters useful for the extension of the control technique to other atomic and molecular systems and possible expansion to other applications.

Parameters, for instance fluctuations in the energy and duration of pulses or ionization rate associated with much shorter pulses need further studies to optimize the application for different experimental geometries.

This study based on polychromatic π-pulse method, shown to be more efficient, has hence provided a general numerical solution to a fascinating fundamental theoretical problem with numerous potential applications in variety of fields such as (i) quantum computing (ii) spectroscopy and microscopy (iii) quantum control of chemical and biochemical reactions (iv) control of nanosystems (v) effective generation of UV ultrashort pulse and pumping of UV lasers. Another advantage of the scheme is the excitation of highly excited states having large principal quantum numbers, known as Rydberg states. Excitation to these states will be described in Chapter 4.

Chapter 4

Control of Rydberg States of Hydrogen–like Alkali atoms Using Multiphoton π-pulse Scheme

4.1 Introduction

Highly excited atoms commonly referred to as Rydberg atoms have attracted numerous interests over the past few years. The study and excitation of Rydberg atoms particularly contributed to the development of practical experimental techniques in ultrasensitive high resolution spectroscopy and also in quantum information processing and computation on the MHz scale [45] like the implementation of fast quantum gates between neutral atom qubits [54]. These numerous interests are a result of the role played by the exaggerated properties of these kinds of atoms. The physical properties of atoms in Rydberg states are important in the presence of external fields [103, 104] and during collision or ionization processes [103 – 105]. The question is what are these Rydberg atoms and why are their properties so important.

In this chapter, the concept of Rydberg atoms is generally introduced. The properties are discussed and shown to be advantageous in applying to numerous fields. Multiphoton π-pulse scheme based on the density matrix formalism is used to demonstrate Rydberg excitation in Rubidium atoms. Certain physical parameters relating to control are tested to show how population inversion to Rydberg states can be influenced. Also, the advantage of using multiphoton π-pulse scheme over single π-pulse for excitation is shown. Finally, the effects of detuning, comparison between using the RWA and going beyond the RWA, and their influence on Rydberg excitation are demonstrated.

4.2 Rydberg atoms and their properties

Atoms excited to their Rydberg states are generally known as Rydberg atoms. These states are characterized by a high principal quantum number, n. Atoms can be made a Rydberg atom by enhancing their valence electron to a highly excited energy level [106] which are exceptionally long-lived states. On the average, a Rydberg atom decays to the ground state in orders of milliseconds (ms) as compared to an ordinary excited state that possesses a lifetime in the orders of microseconds (μs).

An interesting property of Rydberg atoms is their size. These atoms are estimated to have a diameter approximately 100,000 times that of atoms in the ground state. This means a diameter in the orders of a hundredth of a millimetre [105 – 106]. They also have very large radii as the radius of the orbit is equivalent to n^2 and a geometric cross sectional area corresponding to n^4. They have a Radiative lifetime that scale as n^3, this means the separation of the next energy level varies as $1/n^3$ leading to more closely spaced energy levels as they almost merge when approaching the Energy continuum. As the energy levels increases they are denoted by increasing values of n. These closely spaced merging Rydberg states create the Rydberg series [107]. As these states are closely spaced (as shown in Figure 4.1), an ultrashort pulse will excite a superposition of many Rydberg states forming what is known as the Rydberg wave packet [2].

Rydberg atoms are Hydrogen–like atoms in terms of their fundamental properties, hence, can be described by the Bohr model of atoms. The formula based on Bohr model that demonstrates the Binding energy E_B of Rydberg series [106] is given by:

$$E_B = -\frac{R_c}{n^2} \qquad (4.1)$$

Where, R_c represents the Rydberg constant, given as 1.0974×10^5 cm^{-1} and n represents the principal quantum number.

Another particularly interesting feature of Rydberg atoms is their sensitivity. Rydberg atoms are highly sensitive to their environment due to the large dipole moments, which foster long-range dipole–dipole interactions [Figure 4.1], thereby having extreme response to external fields [108]. They are so sensitive that even a weak electric field easily affects them and can be used to control and enhance their interactions with other Rydberg atoms. An adverse consequence of this sensitivity is that they are easily perturbed or ionized by collision, ionization and other decoherence sources like blackbody radiation which suppresses optimal excitation to Rydberg states.

These numerous properties have attracted increasing interest in channelling the application of Rydberg atoms into numerous fields like quantum computing and high precision spectroscopy [45, 109].

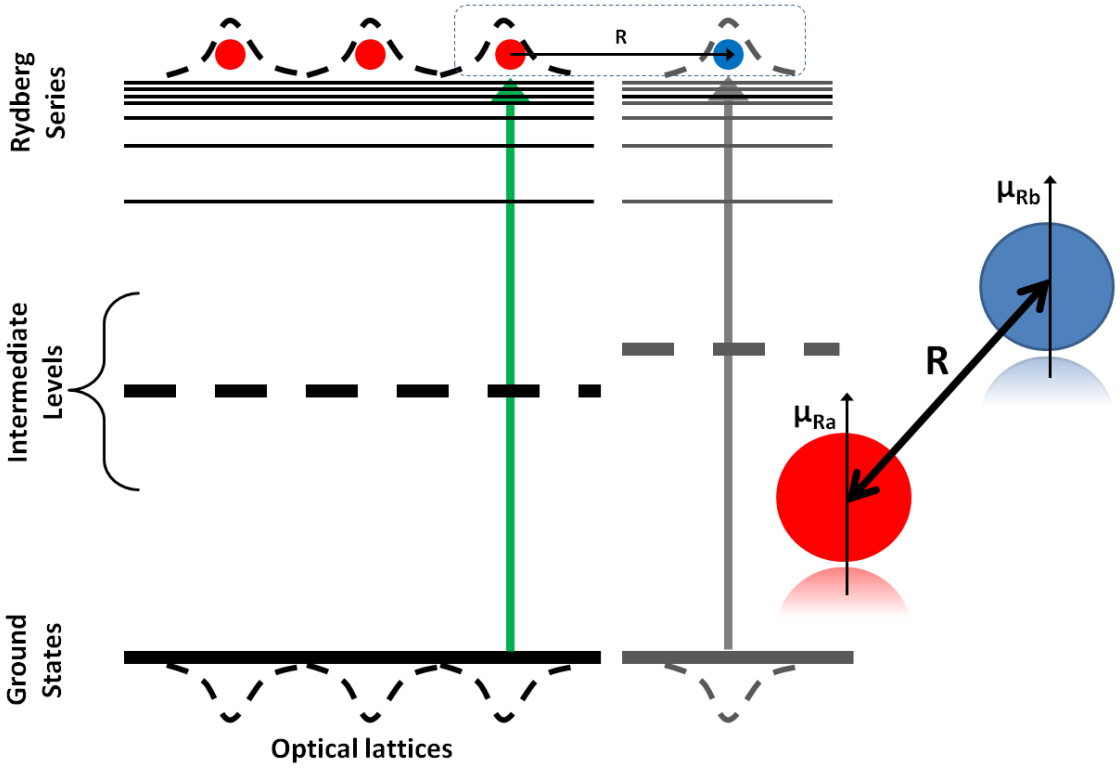

Figure 4.1: Rydberg dipole-dipole interaction between two atoms with an interatomic distance **R** between them. μ_x represents the transitional dipole moment of these atoms from their ground states.

4.3 Applications of Rydberg atoms

Numerous researches on Rydberg atoms have demonstrated wide range of applications in different fields such as astrophysics [110], high precision spectroscopy [109], ultracold quasi-neutral plasma by photoionization and control of electron temperatures in these ultracold plasmas of neutral Rydberg atoms [111] and most especially in quantum information processing (QIP) [44, 45].

One very important research field linked to Rydberg atoms is astrophysics [110]. This study by Gnedin *et al* shows the possible existence of Rydberg atoms in certain interstellar regions. Their goal was to demonstrate some astrophysical targets of Rydberg atoms and further show that some observed collision induced absorption and Radiative recombination of low-energy ions in interstellar media by molecular hydrogen are as a result of absorption by these atoms in highly excited Rydberg states.

Since the introduction of laser cooling and trapping, these atoms have been experimentally prepared in milli-kelvins (mK) regime by exciting these Rydberg atoms to foster strong interactions with other Rydberg atoms which has proven beneficial in numerous extended applications. These include potential for simulating quantum many-body system interactions and design of fast long-range two qubit gates. Proposals have been made to utilize the numerous advantages of the properties of these atoms to implement high fidelity quantum gates between neutral atom qubits based on Rydberg interactions [112]. According to

Saffmann [45, 112], the availability of these strong long-range interactions being able to be coherently tuned on and off is a useful tool for wide range applications in QIP.

Earlier protocols [54, 113 – 115] were based on Rydberg blockade mechanism, where the presence of excited Rydberg atoms prevent other atoms from being excited with gate operations being mediated by the excitation of Rydberg states [54]. Excitation to low-lying Rydberg states is particularly important for providing the required energy to perform gate operations [54]. As discussed by Safronova [44], decoherence poses to be a serious issue and hence, detrimental to gate operations. An advantage of implementing gates based on excitation to low-lying Rydberg states is that decoherence effects like blackbody radiation is almost negligible as the Radiative lifetimes of these states are overshadowed by spontaneous emission [116].

4.4 Control of Rubidium low-lying Rydberg states with trichromatic femtosecond π-pulses for ultrafast QIP.

In this section, an ultrafast femtosecond time scale trichromatic π-pulse illumination scheme for coherent excitation and manipulation of low-lying Rydberg states in rubidium is proposed. Selective population of $nP_{3/2}$ levels with principal quantum numbers $n \lesssim 12$ using 75 fs laser pulses is achieved. The density-matrix equations of a four-level ladder system beyond the rotating-wave approximation have to be solved to clarify the balance between the principal quantum numbers, the duration of the laser pulses and the associated ac-Stark effects for the fastest optimal excitation. The mechanism is robust for femtosecond control using different level configurations for applications in ultrafast quantum information processing and spectroscopy.

This section is organized as follows: in sub-section 4.4.1, a general introduction to the study of control of Rydberg states in rubidium is given. In sub-section 4.4.2, the mathematical model and the main results from the simulations are presented. In sub-section 4.4.3, the influence of the transitional dipole moments together with the pulse duration is discussed. In sub-section 4.4.4, the advantages of using π-pulse multiphoton processes over the single-photon excitations are shown. In sub-section 4.4.5, the influence of field detuning on the population inversion is investigated. In subsection 4.4.6, the need of avoiding the RWA in our simulations by comparing the results with the ones obtained in the RWA is discussed and finally, the conclusion is presented.

4.4.1 Introduction

Selective excitation and manipulation of Rydberg states plays a crucial role in quantum information processing, a field of rapid theoretical and experimental progress with a large number of proposals for quantum information processors being investigated [45, 112]. A central issue is the design of fast quantum gates, with recent proposals using neutral atoms and molecules that allow gate operation times set by the time scale of the laser excitation [54, 117, 118]. In the case of neutral atoms, the requirement that the gate operation time is short compared to the typical time of decoherence mechanisms, including spontaneous emission, collisions, ionization of the Rydberg states, transitions induced by black body radiation, or motional excitation of the atoms trapped in an optical lattice, leads to the search of state-selective Rydberg excitation schemes using femtosecond pulses.

Despite the fact that excitation to a single n-Rydberg level requires nanosecond or cw lasers with a narrow bandwidth, coherent control tools as control algorithms to optimally shape femtosecond laser pulses have been successfully used to address a single transition [119, 120],

as well as multipulse schemes using 150 fs pulses, which alone would populate about ten n-Rydberg levels, have shown the ability to selectively populate a single or a few levels [121, 122]. These different schemes address the excitation of relatively high Rydberg levels, typically of principal quantum numbers as $n \sim 30$. Several models have recently been proposed however to implement fast quantum gates in neutral atoms by using specific low-lying Rydberg states [54, 117], for which faster femtosecond time scale selective coherent excitation schemes are demanded.

The present study analyses a particular control scheme based on the Rabi flopping behaviour involving polychromatic π-pulses. For ultrafast control, π-pulse polychromatic control techniques benefit from the fact that no delay between pulses is involved as compared to adiabatic schemes, so that the interaction time remains of the order of the laser pulse temporal width. The control of population transfer between a pair of quantum states involving single or polychromatic transitions by illuminating the atom with resonant π-pulses has extensively been implemented using from long to ultrashort pulses [2, 67, 88]. For the case of a four-level ladder system, population transfer schemes combining adiabatic and π-pulse techniques have also been proposed [99].

Optimal π-pulse single photon excitation from the ground state to a low-lying Rydberg level with ultrashort femtosecond pulses is not feasible due to the small dipole coupling coefficients associated to UV transitions, which require a large electric field to produce a π area and result in ac-Stark splittings from all other allowed transitions, which frustrates the π-pulse excitation. In the present work, we show that this impediment can be circumvented by using trichromatic π-pulse excitation, an approach that was recently reported as a robust method for complete population inversion in a four-level system [88].

In this work, it is shown that the higher values of the dipole coupling coefficients associated to the transitions in a four-level scheme allow for ultrafast excitation of low-lying Rydberg

states, without the need of deep UV wavelengths and with field intensities that avoid significant ac-Stark effects. The study explores the possibilities of trichromatic π-pulse control for ultrafast selective excitation and manipulation of low-lying Rydberg states in rubidium (Rb), as a paradigmatic system for most experiments with Rydberg atoms. Figure 4.2 illustrates the basic control mechanisms of trichromatic π-pulse excitation in a four-level ladder system, as it was also reported in [88]. From left to right in Figure 4.2, complete population inversion from level 1 to level 4 is produced by simultaneous illumination of the atom with a set of pulses with areas as $\sqrt{3}\pi$, 2π, and $\sqrt{3}\pi$, which corresponds to the effect of a π-pulse in a two-level system. The intermediate levels 2 and 3 become temporally populated during the process and become completely de-populated at the end of the interaction. Complete de-excitation of the atom is accomplished by the same set of pulses, which is shown by the central interaction in Figure 4.2, while a two-level like 2π-pulse is produced with doubling the areas of the three pulses.

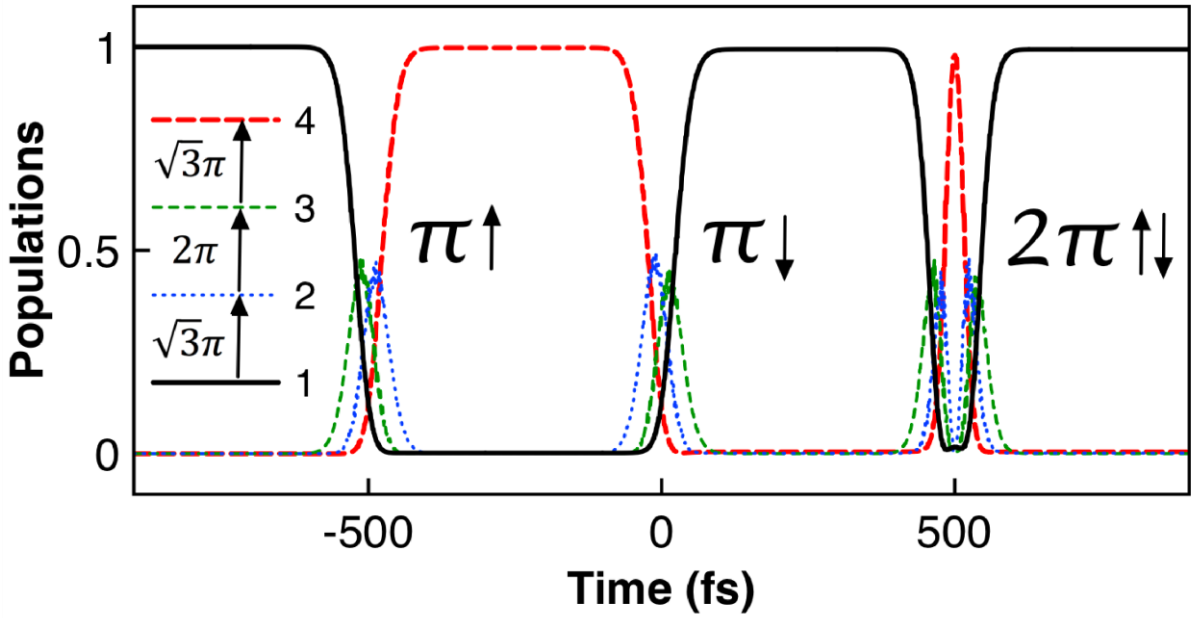

Figure 4.2: In analogy to the effect of a resonant π-pulse in a two-level system (as demonstrated in Chapter 2), which completely transfers the population from one state to the

other; the figure schematically shows the effect of a resonant "trichromatic π-pulse" in a four-level ladder system. A set of 75 fs pulses with areas $\sqrt{3}\pi$, 2π, and $\sqrt{3}\pi$, each one resonant with a particular transition as indicated, completely transfer the population from the lowest to the highest state (up-π-pulse, left), or in the other direction (down-π-pulse, center). Using "trichromatic 2π -pulses", this is of areas $2\sqrt{3}\pi$, 4π, and $2\sqrt{3}\pi$, the system is completely excited and then de-excited, as shown by the third interaction process in the figure (up-and-down-2π-pulse, right).

.

Different requirements have to be considered for the success of the trichromatic π-pulse scheme for ultrafast excitation of Rydberg states. On the one hand, the energies of the chosen atomic transitions have to be different enough compared to the spectral bandwidth of the laser pulses, so that each individual pulse interacts only with its corresponding transition. On the other hand, since the area θ of the pulses is fixed, with $\theta \propto \mu\tau E$, the product μτ of the electric dipole moment coefficients μ and the pulses duration τ has to be sufficiently large so that the envelope field E does not produce important ac-Stark effects. The spectral separation between adjacent levels in the low-lying Rydberg states region in Rb is suitable to accommodate the bandwidth of femtosecond pulses for optimal selective excitation, and as it will be shown in our calculations, the dipole moment coefficients in a four-level ladder scheme warrant its implementation for ultrafast complete population transfer in a trichromatic π-pulse configuration.

4.4.2 Model and Simulation

A 4-level cascade configuration has been chosen in the present study for Rubidium atoms as shown in Figure 4.3. Rubidium was chosen as it is an Alkali atom (hydrogen–like atom) having all its inner electrons along with the nucleus forming a unified core which makes it

seem like a heavy version of hydrogen. It is also a widely used atom for experimental realization of Rydberg excitation. However, the results of this work can be extended to other level configurations and other systems which will be demonstrated in the simulations below.

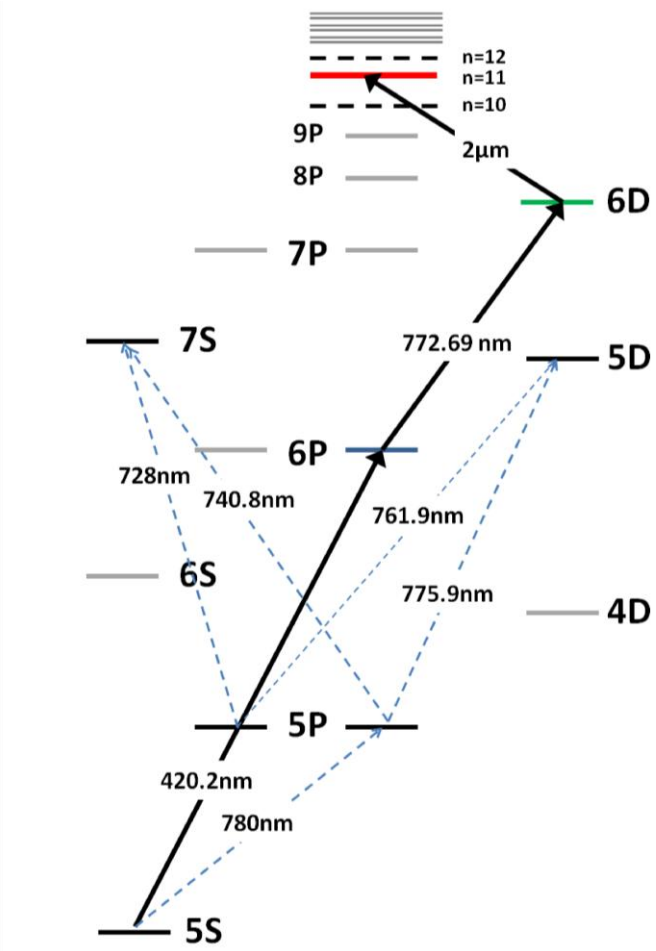

Figure 4.3: Energy levels configuration of the Rb atom chosen to excite the low-lying Rydberg states $nP_{3/2}$ with principal quantum numbers n ≲12

The ground state is the $5S_{1/2}$ level of Rb (level 1), which is coupled with a 420.2 nm laser pulse to the $6P_{3/2}$ (level 2), with μ_{12} = 0.54 × 10^{-29} Cm. The laser pulse has an area of $\sqrt{3}\pi$. The $6P_{3/2}$ level is coupled to the $6D_{3/2}$ (level 3) with a 772.69 nm laser pulse, with μ_{23} = 1.01 × 10^{-29} Cm. This laser pulse has an area of 2π. The precise value of the 3–4 transition energy does not vary the results, so that in our simulations we safely consider a wavelength of 2 μm for the transition from $6D_{3/2}$ to the $nP_{3/2}$ Rydberg state (level 4). The laser pulse

coupling this transition has an area of $\sqrt{3}\pi$. The value of μ_{34} sets the quantum number n of level 4 and it is varied in our study in the range $0.25 \times 10^{-29} < \mu_{34} < 1.25 \times 10^{-29}$ Cm. The precise values for the dipole matrix coefficients have been taken from the data in [123, 124], from which we also estimate $\mu_{14} = 0.02 \times 10^{-29}$ Cm for the allowed $5S_{1/2} \rightarrow nP_{3/2}$ transition, considering n ~ 11. We evaluate the balance between the principal quantum number n of the Rydberg states available for excitation and the duration of the pulses for optimal selective population inversion by trichromatic π-pulse excitation in the femtosecond time scale. For pulse durations $\lesssim$ 500 fs only decoherence processes of the order or faster than picoseconds can affect the coherent interaction. The natural decay times associated to a four-level system as in figure 4.3 are in the nanosecond and microsecond time scales and they can be neglected [125]. Collision and other possible broadening mechanisms are examined in our study by comparing the results for pure dephasing times as short as T_2 = 1 ns and T_2 = 1 ps. We obtain robust almost 100% selective excitation of the (n $\lesssim$ 12)$P_{3/2}$ levels of Rb with 75 fs pulses with pure dephasing of 1 ns, and ≈95% population transfer for 1 ps. The density-matrix equations of the four-level system have to be considered without the assumptions of the rotating-wave approximation (RWA), as it will be further discussed below. The equations read

$$\dot{\rho}_{22} = i\frac{E(t)}{\hbar}(\mu_{12}(\rho_{12} - \rho_{21}) + \mu_{23}(\rho_{32} - \rho_{23}))$$

$$\dot{\rho}_{33} = -i\frac{E(t)}{\hbar}(\mu_{23}(\rho_{32} - \rho_{23}) + \mu_{34}(\rho_{34} - \rho_{43}))$$

$$\dot{\rho}_{44} = i\frac{E(t)}{\hbar}(\mu_{14}(\rho_{14} - \rho_{41}) + \mu_{34}(\rho_{34} - \rho_{43}))$$

$$\dot{\rho}_{11} = -\dot{\rho}_{22} - \dot{\rho}_{33} - \dot{\rho}_{44}$$

$$\dot{\rho}_{12} = -\Gamma_{12}\rho_{12} + i\omega_{12}\rho_{12} + i\frac{E(t)}{\hbar}(\mu_{12}(\rho_{22} - \rho_{11}) + \mu_{14}\rho_{24}^{*} - \mu_{23}\rho_{13}) \qquad (4.2)$$

$$\dot{\rho}_{13} = -\Gamma_{13}\rho_{13} + i\omega_{13}\rho_{13} + i\frac{E(t)}{\hbar}(\mu_{12}\rho_{23} - \mu_{23}\rho_{12} + \mu_{14}\rho_{34}^{*} - \mu_{34}\rho_{14})$$

$$\dot{\rho}_{14} = -\Gamma_{14}\rho_{14} + i\omega_{14}\rho_{14} + i\frac{E(t)}{\hbar}(\mu_{14}(\rho_{44} - \rho_{11}) - \mu_{34}\rho_{13} + \mu_{12}\rho_{24})$$

$$\dot{\rho}_{23} = -\Gamma_{23}\rho_{23} + i\omega_{23}\rho_{23} + i\frac{E(t)}{\hbar}(\mu_{23}(\rho_{33} - \rho_{22}) - \mu_{34}\rho_{24} + \mu_{12}\rho_{13})$$

$$\dot{\rho}_{24} = -\Gamma_{24}\rho_{24} + i\omega_{24}\rho_{24} + i\frac{E(t)}{\hbar}(\mu_{12}\rho_{14} - \mu_{14}\rho_{12}^{*} + \mu_{23}\rho_{34} - \mu_{34}\rho_{23})$$

$$\dot{\rho}_{34} = -\Gamma_{34}\rho_{34} + i\omega_{34}\rho_{34} + i\frac{E(t)}{\hbar}(\mu_{34}(\rho_{44} - \rho_{33}) + \mu_{23}\rho_{24} - \mu_{14}\rho_{13}^{*})$$

where ρ_{ii} are the populations of the levels i, the off-diagonal elements ρ_{ij} represent the coherences between levels i, j, μ_{ij} are the dipole coupling coefficients of the corresponding transitions, and $\omega_{ij} = |E_j - E_i|/\hbar$ are their angular frequencies, with E_i being the energies of the corresponding states. The relaxation of the coherences is considered by pure dephasing rates $\Gamma_{ij} = T_2^{-1}$. The laser pulses are of Gaussian shape, with the electric field E(t) given by

$$E(t) = E_1(t) + E_2(t) + E_3(t)$$

$$= e^{-\left(\frac{t}{\tau}\right)^2}\{E_{01}\cos(\omega_1 t) + E_{02}\cos(\omega_2 t) + E_{03}\cos(\omega_3 t)]\} \qquad (4.3)$$

where E_{01}, E_{02} and E_{03} are the peak amplitudes of the three pulse components $E_1(t)$, $E_2(t)$ and $E_3(t)$, and ω_1, ω_2 and ω_3 are the optical angular frequencies coupling the transitions 1–2, 2–3, and 3–4, respectively. The duration of the pulses is given by $\tau_p = \tau_{FWHM}/(\sqrt{2\,ln\,2})$, where τ_{FWHM} is the full width at half maximum of the pulse intensity profile. In the present simulations all pulses are considered of the same duration.

4.4.3 Influence of Dipole moment and Pulse duration

As discussed above, the selection of pulse duration plays a crucial role in achieving selective manipulation of the desired Rydberg state [126]. Figure 4.4 shows the final population of level 4 that is obtained by trichromatic π-pulse illumination of the system, this is, by simultaneously sending a set of resonant pulses with areas$\sqrt{3}\pi$ in the first transition ($5S_{1/2} \rightarrow$

$6P_{3/2}$), 2π in the second transition ($6P_{3/2} \rightarrow 6D_{3/2}$), and $\sqrt{3}\pi$ in the third transition ($6D_{3/2} \rightarrow nP_{3/2}$). As discussed above and as shown in Figure 4.2, for sufficiently long $\mu\tau$ products and negligible decoherence this illumination scheme completely transfers the population from the ground state $5S_{1/2}$ to the Rydberg state $nP_{3/2}$. The final population ρ_{44} is evaluated in figure 4.4 as a function of the pulses duration for $\tau_p < 500$ fs, and for different values of the μ_{34} transition dipole coupling coefficient.

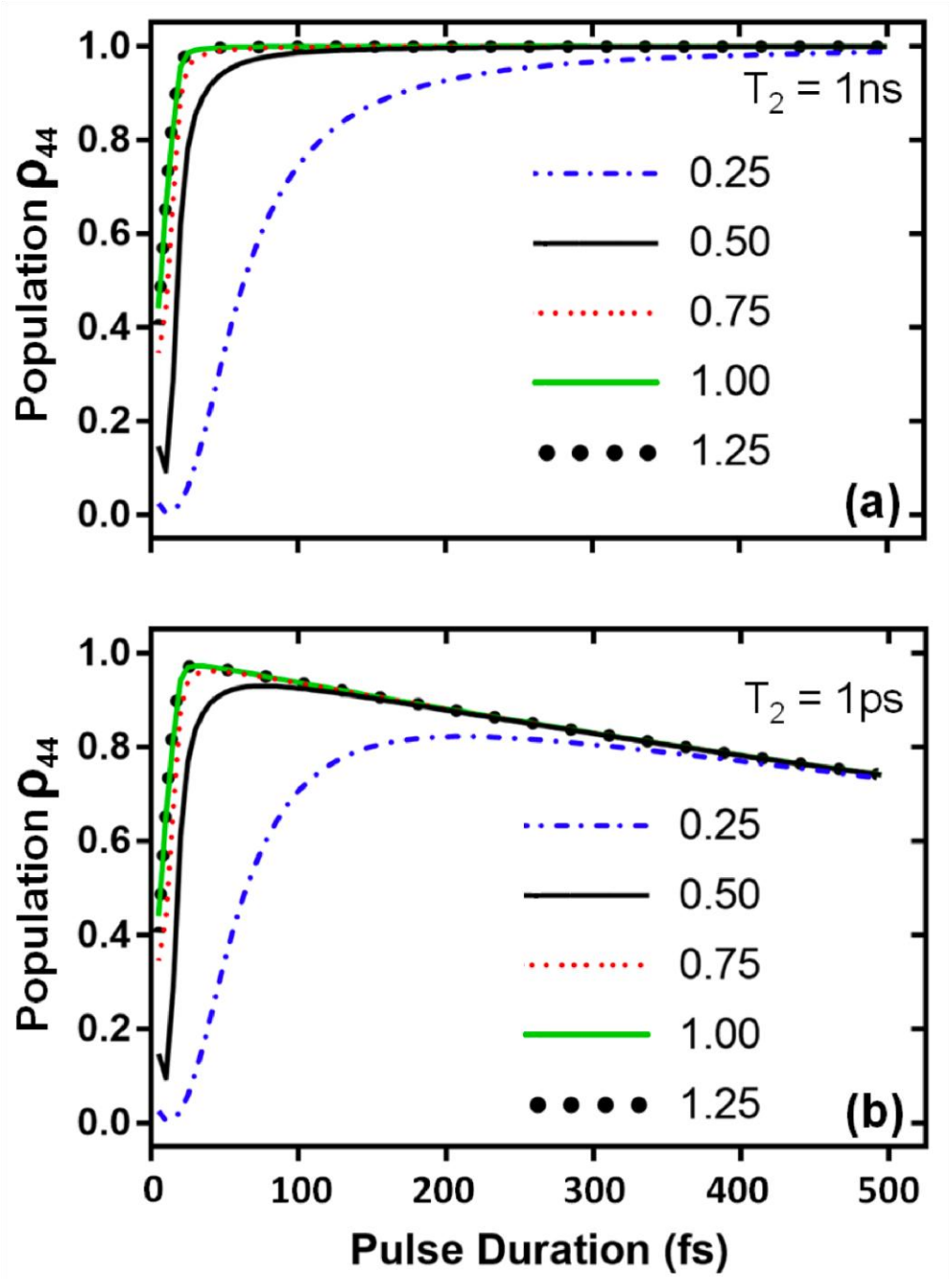

Figure 4.4: Final population of the excited Rydberg state (ρ_{44}) as a function of pulse duration, for dephasing times (a) T_2 = 1 ns and (b) T_2 = 1 ps, and for μ_{34} = 0.25, 0.50, 0.75, 1.00, 1.25, as indicated, in units of 10^{-29} Cm.

Figure 4.4 (a) shows the results for a pure dephasing of 1 ns and Figure 4.4 (b) considers a faster dephasing of 1 ps. We observe that, in both cases, for laser pulse durations shorter than

about 25 fs, the population transfer to the highest state (level 4) is strongly suppressed. This can be explained by the ac-Stark effect produced in the different transitions of the system, which can only be properly computed by considering the density-matrix equations beyond the RWA. With fixed pulse areas, such short pulses ($\tau_p \lesssim 25$ fs) involve high electric fields that produce significant ac-Stark shifts which destroy the trichromatic π-pulse population inversion process. As shown in figure 4.4(a), population transfer to level 4 is not effective either for a transition dipole value as small as $\mu_{34} = 0.25 \times 10^{-29}$ Cm and for pulse durations $\tau_p \lesssim 300$ fs, which is due to the same effect i.e. the electric field in the 3–4 transition becomes too large. Since the μ_{34} transition dipole coupling coefficient decreases as the Rydberg state quantum number n increases, the value of μ_{34} eventually sets the highest $n\mathrm{P}_{3/2}$ Rydberg state that can be optimally accessed for a given duration of the laser pulses. This is clear for dephasings of 1 ns as shown in figure 4.4(a) and also for the 1 ps dephasing in figure 4.4(b). Figure 4.4(b) shows how the fast 1 ps dephasing degrades the population transfer as the duration of the pulses increases, as it can be expected since the dephasing time becomes shorter than the full interaction time.

As mentioned above, our goal is to selectively populate the highest $n\mathrm{P}_{3/2}$ Rydberg state with the shortest femtosecond pulse. The results in figure 4.4 suggest to consider a value of the dipole moment larger than approximately $\mu_{34} = 0.5 \times 10^{-29}$ Cm, which corresponds to the ($n \lesssim 12$)$\mathrm{P}_{3/2}$ low-lying region of the Rydberg states in Rb [123, 124]. To be selective in the excitation process, we further need a spectral bandwidth of the pulses sufficiently narrow compared to the separations between the levels in the region that we are considering, which are 702 cm^{-1} for $9\mathrm{P}_{3/2} - 10\mathrm{P}_{3/2}$, 460 cm^{-1} for $10\mathrm{P}_{3/2} - 11\mathrm{P}_{3/2}$, and about 300 cm^{-1} for $11\mathrm{P}_{3/2} - 12\mathrm{P}_{3/2}$. Therefore, our simulations show that laser pulses of about 75fs, which have a linewidth of 195.7 cm^{-1}, will produce the desired ultrafast selective population inversion

process from the $5S_{1/2}$ ground state to the (n $\lesssim$ 12)$P_{3/2}$ low-lying region of Rydberg states in Rb. A further impediment for the success of the ultrafast process is the possible weak coupling of the used laser pulses to other non-resonant transitions of the system. For instance, in the present case, the ground state $5S_{1/2}$ couples to the $5P_{3/2}$ level with 780 nm (see figure 4.3), which is close to the 772.69 nm laser used in our scheme but is still sufficiently a part to be strongly involved. A system with a larger number of levels than the four-level system considered here should be used to consider the quantitative effect of all close transitions. Nevertheless, these undesirable non-resonant couplings would ultimately be reduced by using some longer laser pulses. Population transfer from level 1 to level 4 in more than 99% is hence achieved with 75 fs pulses and μ_{34} = 0.5 × 10^{-29} Cm (n ∼ 11) for 1 ns dephasing [figure 4.4(a)], which is reduced to ≈95% in the case of the fast 1 ps dephasing [figure 4.4(b)]. This optimal case is also shown in figure 4.5.

4.4.4 Advantages of multiphoton π-pulse scheme over single π-pulse scheme

Poor selectivity is obtained when attempting direct excitation using single deep ultraviolet (UV) wavelengths of laser [127], although these shortcomings may be averted by using a multistep excitation via some intermediate states [128, 129]. In this section we show the advantage of using a multiphoton π-pulse over a single π-pulse scheme for driving the population to the targeted Rydberg state.

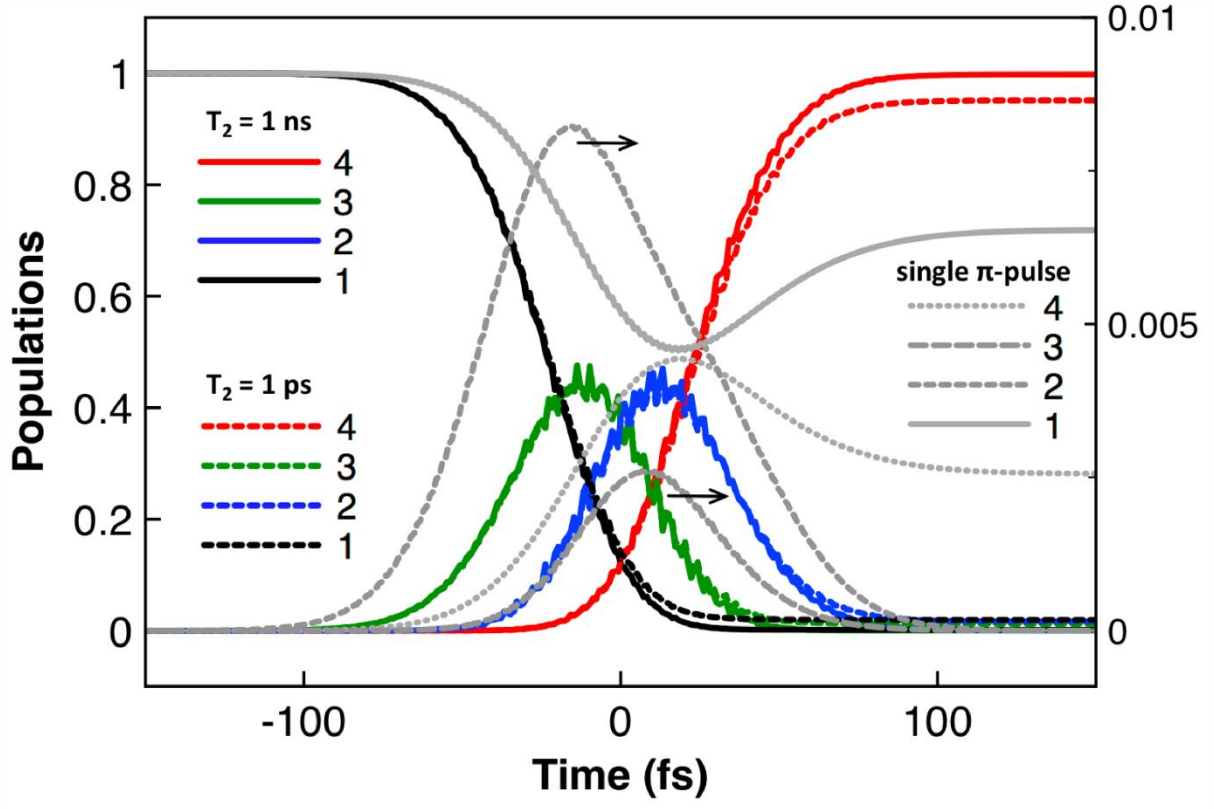

Figure 4.5: Time evolution of the populations for the interaction with 75 fs laser pulses with μ34= 0.5×10^{-29} Cm (n ~ 11), for T_2 = 1 ns and T_2 = 1 ps, as indicated. The black-thin lines (legend on the right) show the case of illumination with a single pulse of area π resonant with the 1–4 transition, considering μ_{14} = 0.02×10−29 Cm and T_2 = 1ns. Note that levels 2 and 3 become slightly populated during the interaction (right y-axis).

Figure 4.5 shows the time evolution of the four populations for optimal illumination with 75 fs laser pulses with $\mu_{34} = 0.5 \times 10^{-29}$ Cm, and for dephasing times of 1 ns and 1 ps. The resulting peak intensities of the optimal 75 fs pulses with $\sqrt{3}\pi$, 2π, and $\sqrt{3}\pi$ areas are 1.17×10^{11} W/cm^2, 0.44×10^{11} W/cm^2 and 1.37×10^{11} W/cm^2, respectively. As required for optimal population inversion, partial population and depopulation of the intermediate levels is not affected by spontaneous emission during the process for these pulse durations, which is advantageous compared to other three-photon excitation schemes with narrower linewidth

lasers [130–135]. As also shown in figure 4.5, although most population is transferred to level 4 at the ending of the pulses, where the field intensity is low, at time about 20 fs – which is within the FWHM of a 75 fs Gaussian pulse – the population in the final Rydberg state is already ~50%, and therefore ionization from the Rydberg states might weakly affect the process. A quantitative study of the effect of ionization would however depend on the particular conditions and geometry [136] and it is beyond the scope of the present analysis.

The grey lines in figure 4.5 show the evolution of the populations in the case of illuminating the system with a single 75 fs π-pulse resonant with the UV 1–4 transition ($5S_{1/2} \rightarrow 11P_{3/2}$). Considering the dipole coupling coefficient μ_{14}= 0.02 × 10^{-29} Cm [123, 124], the peak intensity of the π-pulse results in 2.85 × 10^{13} W/cm^2. In a two-level system (i.e. if levels 2 and 3 were not present), this resonant π-pulse would produce complete population inversion from level 1 to level 4. However, due to the effect of the pulse on the intermediate levels in the four-level system, the π-pulse complete population inversion is frustrated by the ac-Stark shifts produced in the non-resonant transitions involving levels 2 and 3. The coupling of the pulse with the other transitions is apparent in figure 4.5 (right y-axis) since levels 2 and 3 become slightly populated during the interaction. The ac-Stark shift produced by a field of peak amplitude |E| resonant with the 1–4 transition on the 1–2 transition, which is far from resonance, is given by [137]

$$\Delta\omega = \frac{\mu_{12}|E|}{2\hbar}\left(\frac{1}{\omega_{12}+\omega_{14}}+\frac{1}{\omega_{12}-\omega_{14}}\right), \qquad (4.4)$$

which gives −160.6 cm^{-1} for the single 75 fs π-pulse. This frequency shift of the transition is hence of the order of the linewidth of the 75 fs laser pulse (195.7 cm^{-1}) and, as it was also discussed in [88], it prevents optimal π-pulse population inversion (see grey lines in Figure 4.5). For a higher value of dipole coupling in the 1–4 transition, such as $\mu_{14} \gtrsim 0.1 \times 10^{-29}$ Cm, the resulting electric field is already weak to substantially affect the system ($\lesssim 1.14 \times$

10^{12} W/cm^2), in this case $|\Delta\omega| \lesssim 6.42$ cm^{-1} and the π-pulse complete inversion is recovered. It is therefore clear how the single π-pulse population inversion is not effective for a direct ultrashort UV excitation from $5S_{1/2}$ to $nP_{3/2}$.

4.4.5 Influence of detuning:

Detuning as shown in previous chapters is a parameter which greatly demonstrates the robustness of the scheme [88] especially being applied to Rydberg excitation and blockade mechanism in quantum computation most particularly with the numerous hyperfine structures present in the Rubidium atoms and also the packed energy states in the Rydberg series. The π-pulse trichromatic scheme is shown to be robust against frequency variations of the laser central frequency, as it is shown in figure 4.6(a) and (b). Basically, effective population transfer is suppressed for values of field detuning comparable to the linewidth of the laser pulses of 75 fs, which in this case is as large as ~200 cm^{-1}. This is shown in figure 4.6(b) for T_2 = 1 ns (solid line) and T_2 = 1 ps (dashed line).

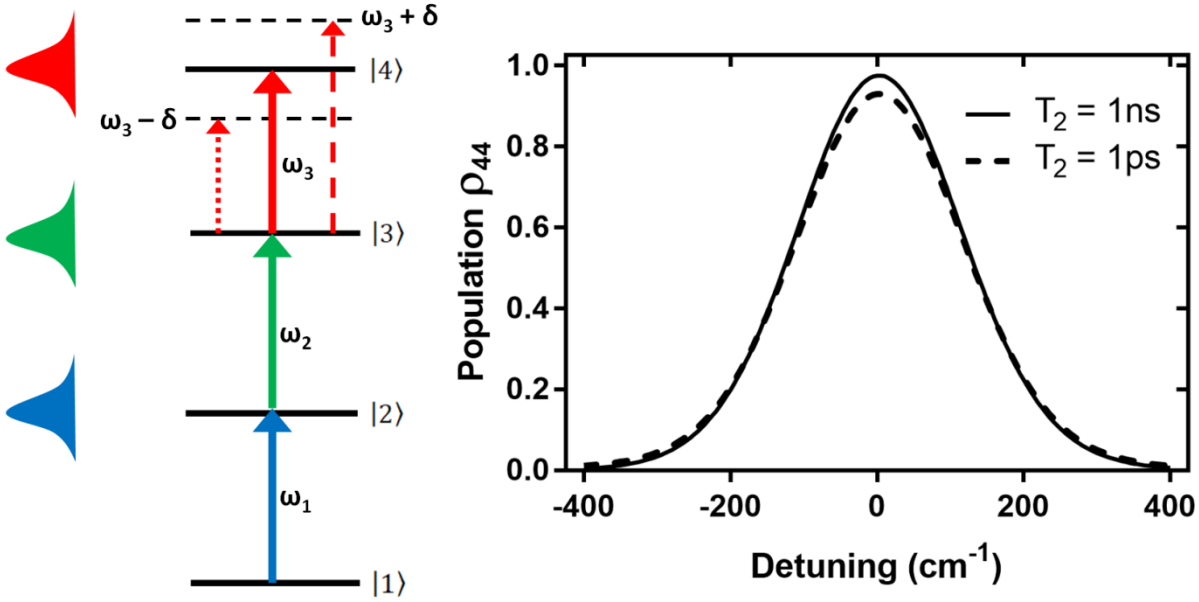

Figure 4.6: (a) Definition of detuning terms, detuning was applied only to the Rydberg state (b) Final population of the excited Rydberg state (ρ_{44}) as a function detuning in the 3–4 transition ($\delta_{34} = \omega_3 - \omega_{34}$), considering the interaction with 75 fs laser pulses with μ_{34} = 0.5 × 10^{-29} Cm. The calculations are shown for T_2 = 1 ns (solid line) and T_2 = 1 ps (dashed line).

4.4.6 Comparison between RWA and beyond RWA

The results that we have obtained with 75 fs pulses hence involve pulse Fourier components that can substantially interact with all the dipole allowed transitions of the system, and therefore it becomes necessary to consider the density matrix equations beyond the RWA. Figure 4.7 shows a comparison of the simulations performed without the RWA with simulations performed considering the RWA. In the RWA the fields are coupled only to their respective transitions, and therefore the effect on the other transitions is absent, so that complete inversion is obtained for all pulse durations [Figure 4.7 (a)]. The disagreement between the two theories is clear for pulses shorter than ∼ 100 fs for μ_{34} = 0.5 × 10^{-29} Cm. For μ_{34} = 0.25 × 10^{-29} Cm the results converge for durations ≳ 500 fs [see also Figure 4.7(a)]. Figure 4.7(b) shows how the coupling of the pulse with the other transitions results in population left in levels 2 and 3 after the interaction, which is only seen without the RWA.

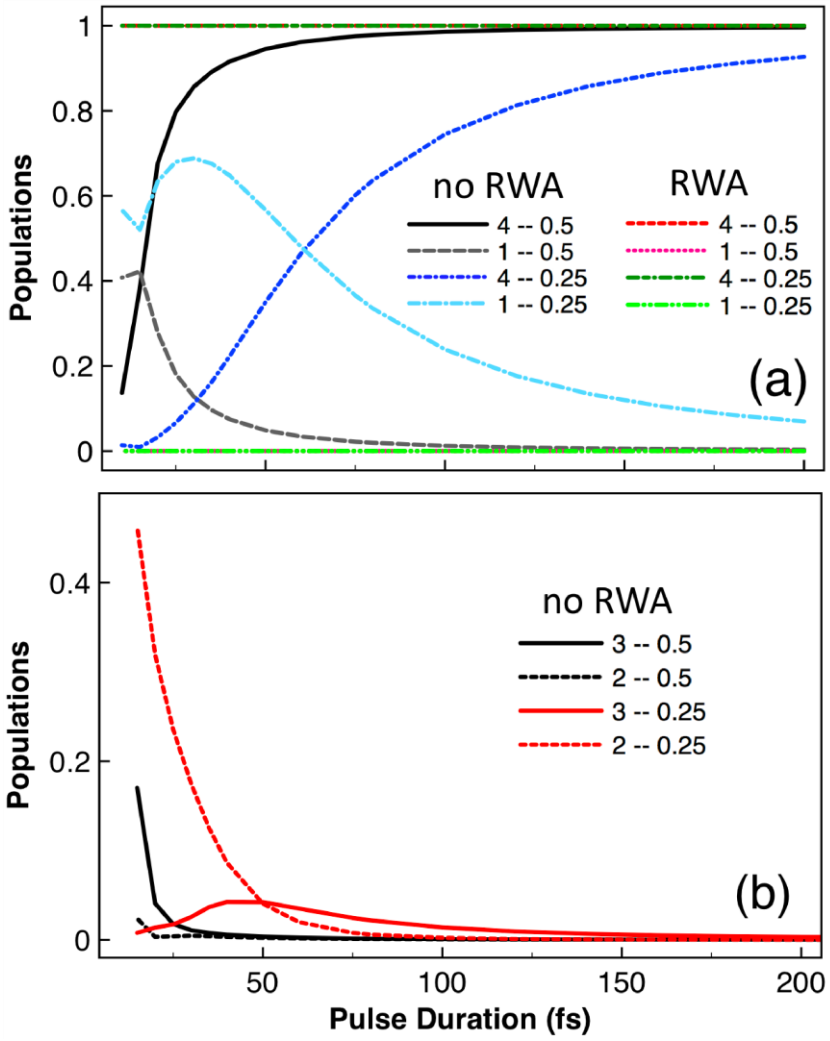

Figure 4.7: Comparison of the calculations without and with the RWA. (a) The final populations of levels 1 and 4 are shown, considering trichromatic π-pulse excitation and the level configuration of Fig. 4.3, for μ_{34} = 0.5 and 0.25, as indicated – in units of 10^{-29} Cm, and considering T_2 = 1 ns. (b) Final populations of levels 2 and 3 without the RWA. Levels 2 and 3 become empty using the RWA in all cases.

4.5 Conclusions

Summing up, the inapplicability of single-photon UV excitation to reach and control Rydberg states with femtosecond laser pulses leads to the need of using multiphoton processes.

Ultrafast selective population of rubidium low-lying Rydberg states using trichromatic π-pulse excitation is demonstrated. 75 fs laser pulses with areas such as $\sqrt{3}\pi$, 2π, and $\sqrt{3}\pi$ produce purely coherent excitation of ($n \lesssim 12$)$P_{3/2}$ Rb Rydberg states due to the short time scale involved in the interaction. The study shows that some higher-n Rydberg states might also be reached by using the same technique but with some longer pulses, which would also reduce the possible non-resonant couplings with other transitions involved in the system. Therefore, although we have chosen a particular configuration of Rb, the fundamental mechanism can readily be extended to other configurations and using different geometries. To the best of our knowledge, this is the fastest scheme that has been proposed for coherent excitation and manipulation of low-lying Rydberg states which display properties that show key applications in quantum information technology and high precision spectroscopy.

Chapter 5

Density Matrix Analysis of Multi-dimensional time-Resolved Spectroscopy and Transient Absorption Spectroscopy

5.1 Introduction

In this chapter, a brief overview on the concepts of Multidimensional time-resolved spectroscopy (MTRS) and transient absorption spectroscopy (TAS) will be presented. Coherent control and quantum control spectroscopy will be further applied to demonstrate control of population transfer and vibrational coherences using both TL and shaped pulses in Oxazine systems. Four-level time-dependent density matrix formalism will be employed to simulate the pulse interaction with these types of systems. The density matrix equations will be used to analyze mode enhancement of population and coherences. The brief relationship between the theoretical approach and the TAS will be discussed. Finally, the influence of numerous parameters on the enhancement and suppression of the population and vibrational states will be discussed.

Multidimensional time-resolved spectroscopy is an important application of coherent control which involves techniques producing spectra that show the magnitude of an optical signal as a function of two or more pulsed laser frequencies. These spectra can be obtained in either frequency or temporal domain. An advantage of these multidimensional spectroscopic methods is the degree of control they provide as the signal primarily depends on multiple input and output beams. [138]

These techniques from multidimensional spectroscopy includes four wave mixing [139], transient absorption involving pump-probe methods [40, 41, 47, 50]. However, the transient absorption spectroscopy is of huge interest and will be discussed next.

5.1.1 Transient Absorption Spectroscopy

Transient absorption spectroscopy is a dynamic time-resolved spectroscopic technique involving two pulses (pump and probe) whereby a portion of the molecule investigated is steered to an excited electronic state by the former. Among different MTRS methods, the TAS is preferred in so many experiments due to its adaptability in carrying out spectroscopic study on numerous types of systems over broad ranges of frequencies and pulse durations (from slower timescales to much faster timescales like sub-attosecond timescales) [140].

Pump-probe method allows for proper control and manipulation of the dynamics of molecular systems, as the laser frequencies required to meet the corresponding transition frequencies of these molecules are readily available with this technique. The idea of the pump-probe technique is that two pulses produced from a laser system are used to excite and probe a sample light absorbing molecule. The initial pump pulse serves as the excitation pulse which is spectrally or temporally modified to cause a change in the dynamics of the system being investigated, for example, by using a liquid crystal (LC) shaper [141]. The delayed second pulse, which is the probe pulse, is almost completely transform limited and is used to cross-examine the initial excitation pulse in order to measure the time-dependent absorption change (transient absorption spectrum). A typical schematic representation of the transient absorption pump-probe measurement is shown in figure 5.1. The transmitted intensity difference between the pump and probe pulse measured by the photodetector and the transient absorption signals are extracted from these measurements. There are three main contributions to the pump-probe signal, which are all equivalent to the final population of the excited state and simultaneously

decay to the lower state. [Figure 5.1(b)]. The first contribution is the ground-state bleaching (GSB), when the molecule is excited, parts of the molecule are steered to the excited state causing a reduction in the ground state distribution of the molecule.

The second is the stimulated emission (SE) for optically allowed transitions where photons of the probe pulse fosters emission from the excited state of sample molecule. The last contribution is excited state or induced absorption (ESA). This stage occurs when molecules in the excited state absorb more protons and are further steered to a higher excited state. There are other possible contributions as molecules undergo more processes after excitation. The information relating to population and vibrational coherences are extracted from the transient absorption signal levels and oscillatory components appearing in the transient absorption signal. This will be further discussed in section 5.2.

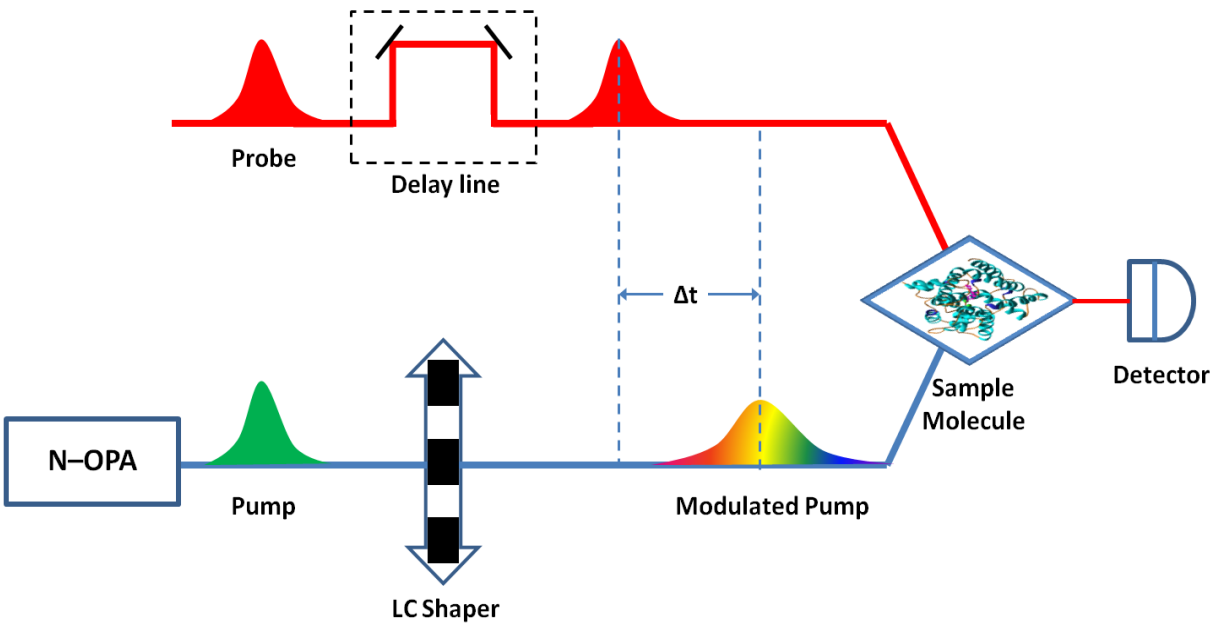

$$I \propto \left|\tilde{E}\right|^2 \qquad (5.1a)$$

$$\tilde{E}_{out}(\omega) = \tilde{E}_{in}(\omega)\exp[i\varphi(\omega)] \qquad (5.1b)$$

The tailored electric field in the time domain will be given as

$$\tilde{E}_{out}(t) = \mathfrak{F}^{-1}\{\tilde{E}_{out}(\omega)\} \qquad (5.1c)$$

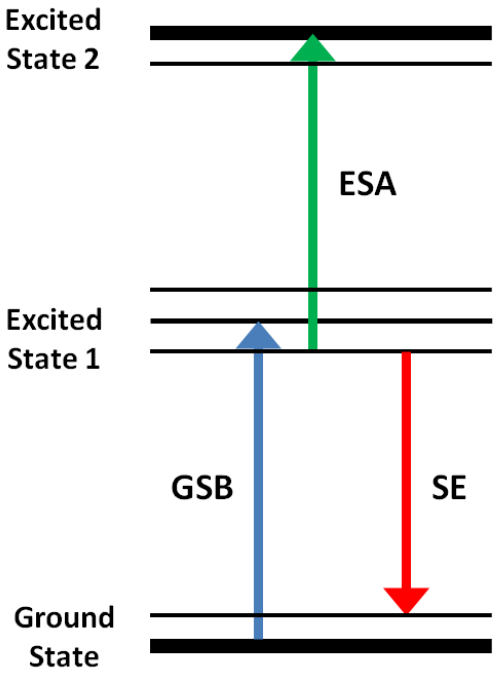

Figure 5.1: Schematic representations of **(a)** the femtosecond pump-probe spectroscopy showing the delay Δt between the two pulses. The pump pulse is modulated using an LC shaper for instance, LCM and focused on a sample molecule. The probe pulse is left unmodulated and used to measure the dynamic changes made by the pump pulse **(b)** the main contributors to the transient absorption signal; ESA, GSB and SE.

5.2 Relationship between the TAS measurement and the Density Matrix Formalism

Intensity is vital when dealing with molecules and their interaction with laser light. Information related to the time evolution of the population and vibrational coherence can be extracted from the transient absorption signal level and oscillation amplitudes. The signal level is as a result of absorption of an electronic state. If the system is excited by an ultrashort laser pulse, it could promote the creation of vibrational wavepackets as stated much earlier which could modulate the absorption leading to presence of oscillations in the transient signal [141]. The study of these molecules can be simplified by summarizing the active modes to a

4-level system which is theoretically analyzed using the density matrix formalism. In this work, the 4-level system has two electronic states, each having two vibrational states; therefore, the signal level can be separated into the ground-state absorption ($\rho_{11} + \rho_{22}$) and the excited-state absorption ($\rho_{33} + \rho_{44}$) that describes the transient effects.

Other important parameters include the characteristic decay and pure dephasing times of the populations (ρ_{ii}) and coherences (ρ_{ij}) given by $\mathrm{T}_1 = \gamma_{ii}^{-1}$ and $\mathrm{T}_2 = \Gamma_{ij}^{-1}$ respectively. Values related to the coupling coefficient and vibrational frequency (i.e. the separation between vibrational levels obtained from the period of the oscillatory motion in the transient absorption signal or the ring breathing mode of the molecule being investigated) can directly be measured in the pump-probe experiments. These different parameters can directly be inputted into the density matrix simulation as shown in subsection 5.3.2.

5.3 Quantum Control of Population Transfer and Vibrational States via Chirped Pulses in Four Level Density Matrix Equations

In this section, the effect of chirped excitation and the excitation detuning on the coherent control of population transfer and vibrational states in a four-level system is investigated. Density matrix equations are studied for optimally enhanced processes by considering specific parameters typical of Oxazine systems. Our simulations show a strong dependence on the interplay between chirp and excitation detuning and predict enhancement factors up to 3.2 for population transfer and up to 38.5 for vibrational coherences of electronic excited states. The study of the dynamics of the populations and vibrational coherences involved in the four-level system allows an interpretation of the different enhancement/suppression processes observed.

5.3.1. Introduction

Tailoring of the optical phase of femtosecond pulses has been used in several applications in photochemistry and time-resolved spectroscopy [39, 50, 142–155]. In general, tailored pulses can be applied using two different approaches: Coherent Control (CC) or Quantum Control Spectroscopy (QCS). Closed-loop learning algorithms are exploited in CC to generate complex optical phases in order to optimize specific reaction pathways. CC has been used as a tool in the control of dynamic processes [3, 30, 156–158], and it explains how a specific state can be selectively populated, for example, to attain 100% population transfer [159–162], and recent studies have shown the possibility of having enhancements even higher than 100% [163–172]. QCS also exploits tailored excitation but differs from CC in its applications [167, 173]. Its goal is to simplify complex molecular dynamics by tailoring excitation pulses to enhance or suppress specific molecular signal features by comparing molecular transient between TL and modulated pulses. A central aspect in both approaches, CC and QCS, is the control of population transfer between the ground and excited states, as well as the generation of vibrational coherence in both potential surfaces. By controlling the population transfer or by suppressing specific molecular vibrational coherences, a photochemical reaction channel can be selectively chosen [41, 164, 166, 169, 174–185], or a certain mode in a multidimensional time-resolved signal can be suppressed [174, 186–191].

The control of population transfer and vibrational coherences in molecules in general is challenging since several molecular and optical parameters play a role. Indeed, the molecular system under study dictates the displacement of the addressed levels and the vibrational and electronic dephasing rates. While the electronic dephasing rates can in some cases be influenced by the choice of the solvent [192–195], the displacement between the ground and the excited states is generally fixed. Pulse characteristics can be more easily tailored than molecular properties. Crucial parameters are the spectral detuning of the excitation with

respect to the molecular absorption region as well as the temporal shape of the excitation, which is tailored by using phase and/or amplitude shaping. In the present paper we address the coherent control of population transfer and vibrational states in laser dye Oxazine systems. We have chosen Oxazine systems since these systems are being extensively studied in spectrally and time-resolved transient absorption spectroscopy experiments, in the femtosecond time regime, to elucidate the fastest fundamental processes in photochemistry and photobiology, like isomerization and electron and photon transfer [196]. In particular, we analyze the response of a four-level system, consisting of two electronic states both including two vibrational sub-states (see Figure 5.2), to the excitation of chirped and detuned femtosecond laser pulses. We will show that the basic processes producing enhancement/suppression factors on the population transfer and vibrational coherences can be understood from this relatively simple molecular model by studying the dynamics of the density matrix elements, and will compare our results with previous theoretical studies and experimental measurements.

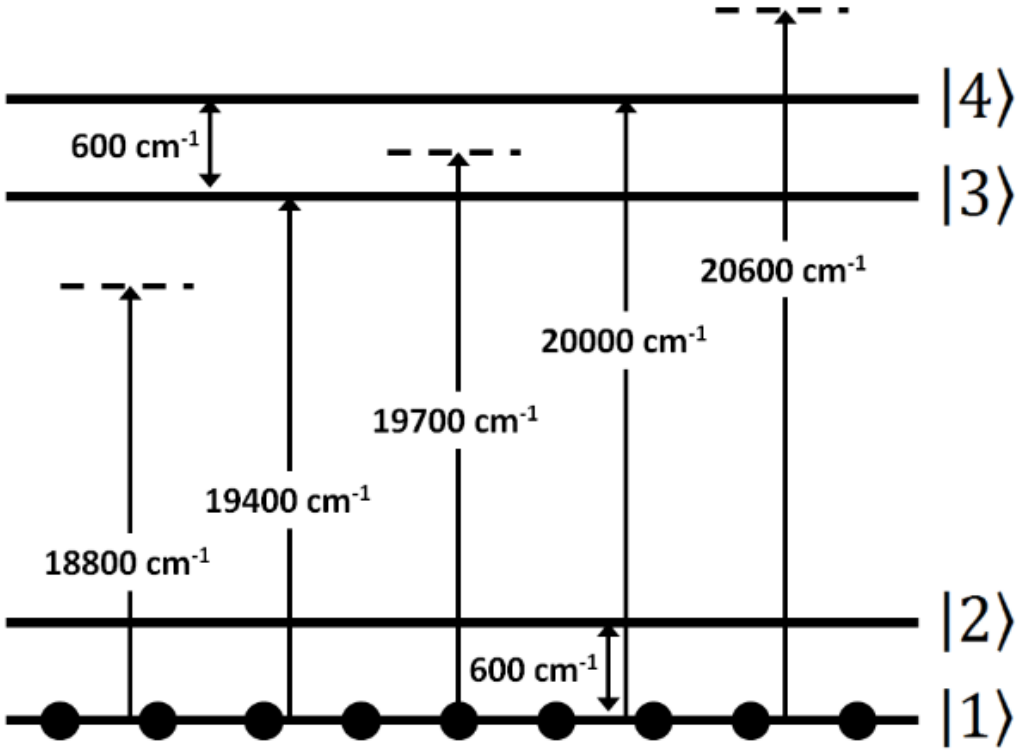

Figure 5.2: Schematic representation of the four level system showing the transition wavenumbers considered and different excitation frequencies.

Indeed, an asymmetry in the molecular response to chirped pulses was first predicted theoretically by Ruhman and Kosloff [197] and observed experimentally by Bardeen et al. [198]. They explained how the excitation of a vibration in the ground state of a molecular system can be accomplished by negatively chirped pulses in an intrapulse pump-dump process. A similar scheme was implemented by Cao et al. [199] for quantum coherent control of population transfer. They demonstrated theoretically that electronic population inversion probabilities of up to 99% in molecular systems can be achieved by using intense positively chirped broadband laser pulses. Their results are robust with respect to thermal and condensed phase conditions and are supported by experimental evidence. For instance, solvent environment was recently shown to be sensitive to positively chirped pulses, and a dependence of the optimal chirp with respect to the displacement between excited and ground state's molecular potentials was also found. On the way to find the optimal chirp for coherent manipulations, the electronic dephasing rate is theoretically studied to take both effects into account. It is found that for increasing dephasing times, the coherence is enhanced especially if negative chirp is added [200].

In this work the influence of chirp, detuning and dephasing on the enhancement in population transfer and vibrational coherence in a four level system (Figure 5.2) is studied in detail. The density matrix model is first described and the parameters used are given in Section 5.3.2. As mentioned above, the parameters used to solve the system are specific for the case of Oxazine; however, due to the simplicity of the mathematical model that we consider, the physical mechanisms elucidated in this study are of a fundamental type and can therefore be extended to other systems. In Section 5.3.3 the main results obtained from the simulations is shown. Maps showing the enhancement in the populations and the vibrational coherences

have been produced by varying the incident spectral phase chirp from -10^3 fs^2 to 10^3 fs^2 and the excitation spectral detuning from -5×10^3 cm^{-1} to 5×10^3 cm^{-1}. The most relevant regions in these maps are then studied in detail by plotting the evolution in time of the respective density matrix elements for the important specific cases (enhancement/suppression), and an interpretation of the observed effects is given. In Section 5.3.4 a study of the influence of the duration of the laser pulse on the observed enhancement effects is presented. The influence of the laser peak intensity in some specific cases is shown in Section 5.3.4(2), and in Section 5.3.4(3) the important effect of electronic dephasing is investigated. Finally, the overall conclusions of the chapter are given in Section 5.4.

5.3.2 Density Matrix Simulations

A non-perturbative, time-dependent density matrix approach is used to simulate the interaction of a femtosecond laser pulse with a four level system consisting of 2 electronic states — ground and excited state, each containing two vibrational levels (Figure 5.2).

All simulations were carried out under the slowly-varying envelope (SVEA) and rotating-wave (RWA) approximations, by using a 4–5 order Runge-Kutta algorithm (see also Section 3.2.4 [88],). The laser temporal pulse shape is a direct input to the code, and the system allows the laser pulse to interact with all electronic transitions. The model can be written as follows:

$$\begin{aligned}
\dot{\rho}_{22} &= -\gamma_{22}\rho_{22} + \gamma_{32}\rho_{33} + \gamma_{42}\rho_{44} + i\{\mu_{23}(\rho_{32}\Omega^* - \rho_{23}\Omega) + \mu_{24}(\rho_{42}\Omega^* - \rho_{24}\Omega)\} \\
\dot{\rho}_{33} &= -\gamma_{33}\rho_{33} + \gamma_{43}\rho_{44} + i\{\mu_{13}(\rho_{13}\Omega - \rho_{31}\Omega^*) + \mu_{23}(\rho_{23}\Omega - \rho_{32}\Omega^*)\} \\
\dot{\rho}_{44} &= -\gamma_{44}\rho_{44} + i\{\mu_{14}(\rho_{14}\Omega - \rho_{41}\Omega^*) + \mu_{24}(\rho_{24}\Omega - \rho_{42}\Omega^*)\} \\
\dot{\rho}_{11} &= -\dot{\rho}_{22} - \dot{\rho}_{33} - \dot{\rho}_{44} \qquad (5.2) \\
\dot{\rho}_{12} &= -\bar{\Gamma}_{12}\rho_{12} + i\omega_{21}\rho_{12} + i\{\mu_{13}\rho_{32}\Omega^* - \mu_{23}\rho_{13}\Omega + \mu_{14}\rho_{42}\Omega^* - \mu_{24}\rho_{14}\Omega\} \\
\dot{\rho}_{13} &= -\bar{\Gamma}_{13}\rho_{13} + i(\omega_{31} - \omega_1)\rho_{13} + i\Omega^*\{\mu_{13}(\rho_{33} - \rho_{11}) + \mu_{14}\rho_{43} - \mu_{23}\rho_{12}\}
\end{aligned}$$

$$\dot{\rho}_{14} = -\bar{\Gamma}_{14}\rho_{14} + i(\omega_{41}-\omega_1)\rho_{14} + i\Omega^*\{\mu_{14}(\rho_{44}-\rho_{11}) + \mu_{13}\rho_{34} - \mu_{24}\rho_{12}\}$$

$$\dot{\rho}_{23} = -\bar{\Gamma}_{23}\rho_{23} + i(\omega_{32}-\omega_1)\rho_{23} + i\Omega^*\{\mu_{23}(\rho_{33}-\rho_{22}) + \mu_{24}\rho_{43} - \mu_{13}\rho_{21}\}$$

$$\dot{\rho}_{24} = -\bar{\Gamma}_{24}\rho_{24} + i(\omega_{42}-\omega_1)\rho_{24} + i\Omega^*\{\mu_{24}(\rho_{44}-\rho_{22}) + \mu_{23}\rho_{34} - \mu_{14}\rho_{21}\}$$

$$\dot{\rho}_{34} = -\bar{\Gamma}_{34}\rho_{34} + i\omega_{43}\rho_{34} + i\{\mu_{13}\rho_{14}\Omega - \mu_{14}\rho_{31}\Omega^* + \mu_{23}\rho_{24}\Omega - \mu_{24}\rho_{32}\Omega^*\}$$

I. Parameters of the Density Matrix Simulation

The diagonal elements ρ_{ii} are the populations of the levels, the off-diagonal elements ρ_{ij} represent the coherences between levels, and μ_{ij} are the dipole coupling coefficients of the electronic transitions. $\omega_{ij} = |E_j - E_i|/\hbar$ are the angular frequencies of the transitions $i-j$, with $E_{i,j}$ being the energies of the quantum states i and j (see Figure 5.2). $\Omega(t) = E(t)\exp[i\varphi(t)]/\hbar$ represents the input slowly-varying complex amplitude of the electric field. E(t) is the slowly varying real field envelope, and $\varphi(t)$ is the slowly varying phase, which for transform limited pulses is chosen constant. The decay rates of the transitions $i-j$ are given by γ_{ij} and the relaxation rates of the levels satisfy $\gamma_{22} = \gamma_{21}$, $\gamma_{33} = \gamma_{31} + \gamma_{32}$, $\gamma_{44} = \gamma_{41} + \gamma_{42} + \gamma_{43}$. The decay rates of the coherences are defined by $\bar{\Gamma}_{12} = \frac{\gamma_{22}}{2} + \Gamma_{12}$, $\bar{\Gamma}_{13} = \frac{\gamma_{33}}{2} + \Gamma_{13}$, $\bar{\Gamma}_{14} = \frac{\gamma_{44}}{2} + \Gamma_{14}$, $\bar{\Gamma}_{23} = \frac{(\gamma_{22}+\gamma_{33})}{2} + \Gamma_{23}$, $\bar{\Gamma}_{24} = \frac{(\gamma_{22}+\gamma_{44})}{2} + \Gamma_{24}$, and $\bar{\Gamma}_{34} = \frac{(\gamma_{33}+\gamma_{44})}{2} + \Gamma_{34}$, which include the relaxation of the coherences and the pure dephasing rates Γ_{ij}The parameters used are summarized in Table 5.1.

Table 5.1: Parameters used in the simulations

Parameters	**Value**
Transitional dipole coupling coefficient (μ_{ij})	$4.22 \times 10^{-29}\ Cm$
Peak amplitude of field, E	$8.7 \times 10^{7}\ V/m$
Vibrational Frequency ($\tilde{v}_{12}$ and $\tilde{v}_{34}$) $\tilde{v}_{12} = \tilde{v}_{34} = 600\ cm^{-1}$	600 cm^{-1}

Wave numbers of the different transitions.		
$\tilde{\upsilon}_{13}$	$\|1\rangle \rightarrow \|3\rangle$	19400 cm^{-1}
$\tilde{\upsilon}_{14}$	$\|1\rangle \rightarrow \|4\rangle$	20000 cm^{-1}
$\tilde{\upsilon}_{23}$	$\|2\rangle \rightarrow \|3\rangle$	18800 cm^{-1}
Spectral chirp φ''		$-1000\ fs^2$ to $1000\ fs^2$
Purely dephasing rates (Γ_{ij})		$\Gamma_{12}^{-1} = \Gamma_{34}^{-1} = 1.7\ ps$
		$\Gamma_{13}^{-1} = \Gamma_{14}^{-1} = \Gamma_{23}^{-1} = \Gamma_{24}^{-1} = 100\ fs$
Decay rates of the transitions, i − j (γ_{ij})		$\gamma_{ij}^{-1} = 1\ ns$
Duration (full width at half maximum, FWHM) of the Gaussian TL (transform limited) pulses		30 fs, 17 fs

The non-diagonal terms $\rho_{13}, \rho_{14}, \rho_{23}$ and ρ_{24} define the electronic coherences and include dispersive and absorptive properties in the optical transitions, while ρ_{12} and ρ_{34} represent the vibrational coherences of the ground and excited states, respectively.

II. Enhancement Factors

The enhancement factors are defined by the ratio between the values calculated using a chirped pulse (PS) and the ones calculated with a transform limited (TL) Gaussian pulse as:

Enhancement of population in the ground states

$$\frac{(\rho_{11+}\rho_{22})_{PS}}{(\rho_{11+}\rho_{22})_{TL}} \qquad (5.3a)$$

Enhancement of vibrational coherence in the ground states

$$\frac{|\rho_{12}|_{PS}}{|\rho_{12}|_{TL}} \qquad (5.3b)$$

Enhancement of population in the excited electronic state

$$\frac{(\rho_{33+}\rho_{44})_{PS}}{(\rho_{33+}\rho_{44})_{TL}} \qquad (5.3c)$$

Enhancement of vibrational coherence in the excited electronic state

$$\frac{|\rho_{34}|_{PS}}{|\rho_{34}|_{TL}} \qquad (5.2d)$$

The initial population is in level $|1\rangle$ in all the simulations.

5.3.3 Main Results Obtained from the Simulations

In order to resolve the dependence on the central input pulse frequency and the amount of chirp on the transfer of population and the creation of vibrational coherences in the system, the central wavenumber of the input pulse is considered from $\tilde{\nu}$ =15,000 cm^{-1} to 25,000 cm^{-1} (see Figure 5.2), in steps of 100 cm^{-1}, and the values of the spectral phase chirp have been taken from $\varphi'' = -10^3$ fs^2 to 10^3 fs^2, in steps of 10 fs^2. The spectral chirp parameter φ'' has been implemented in the Fourier domain and is defined as $\varphi(\omega) = 0.5\ \varphi''\ \omega^2$, with $\varphi(\omega)$ being the group delay dispersion (GDD) added to the spectral phase of the pulse. Therefore, since only the spectral phase of the laser pulse is varied in our study, the frequency content and the power remains as in the TL pulse for any value of the spectral chirp φ'', as it is usually the case in the experiments. The rephasing of the spectral components produces a time broadening of the pulse given by $\tau_{p_c} = \sqrt{\tau_p^4 + 16(\ln 2)^2\varphi''^2}/\tau_p$, where τ_{p_c} is the FWHM of the chirped pulse intensity profile and τ_p is the duration corresponding to the TL pulse [2].

Figure 5.3 shows the results for the enhancement/suppression factor of the population in the ground state (Figure 5.3a), the vibrational coherence in the ground state (Figure 5.3b), the population in the upper state (Figure 5.3c) and the vibrational coherence in the upper state (Figure 5.3d), sufficiently long after the interaction of the system with the laser pulse.

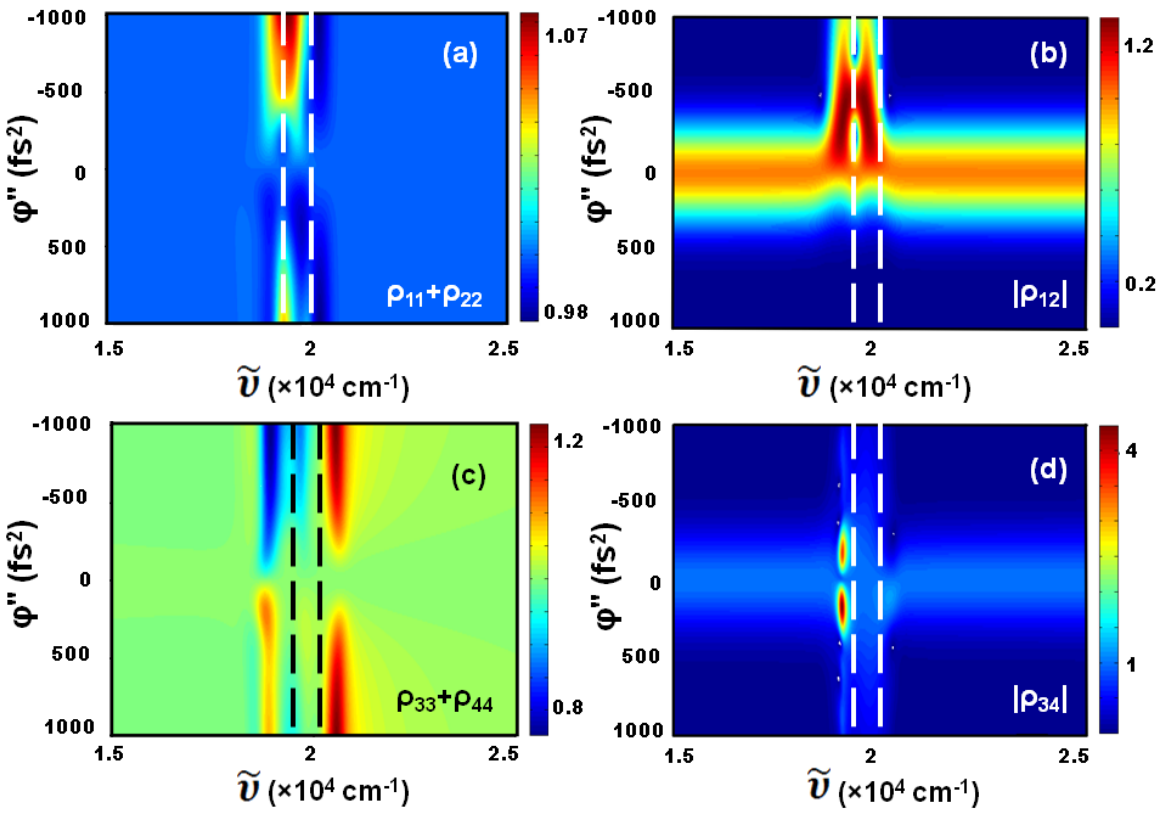

Figure 5.3: Enhancement/suppression factor of (**a**) population in the ground state; (**b**) vibrational coherence in the ground state; (**c**) population in the upper state; and (**d**) vibrational coherence in the upper state. Dashed lines indicate the position of the excited states (see Figure 5.2).

As is clear from Figure 5.3, the interplay between chirp and excitation detuning is crucial for the coherent control of the population transfer and the enhancement or suppression of the vibrational coherences. We can observe regions with more than a 2% enhancement/suppression in the case of the population in the excited state (Figure 5.3c), and enhancement factors as high as 4 for the vibrations in this state (Figure 5.3d). In order to understand the origin of the processes involved in the calculations of Figure 5.3, the different time-scales involved in the interaction need to be considered. On the one hand, the period of the vibration both in the ground and the excited states, which in our simulations is $T_{vib} = 1/(c\tilde{\nu}) \simeq 60$ fs. On the other hand, we note that the duration of the 30 fs laser pulse with $\varphi'' =$

$\pm 10^3$ fs^2 is $\simeq$ 94 fs. For the values of the peak field amplitude and dipole coupling that we have considered, the period associated to the Rabi oscillations is $T_{Rabi} = h/(\mu E) \simeq$ 180 fs. Also important is the spectral width of the 30 fs Gaussian laser pulse, which is $0.441/(c\tau_p) \simeq$ 490 cm^{-1}, which is to be compared with the 600 cm^{-1} of the vibrations, considered in our simulations. The fastest dephasing rate in the simulations shown in Figure 5.3 is 100 fs, which therefore allows in this case for purely coherent processes, since all the interaction is basically finished before that time. We study the influence of the dephasing rates on the enhancement effects in the last part of the paper. We next describe in detail and provide an interpretation of the main results shown in Figure 5.3.

I. Population in the ground state (ρ11 + ρ22):

The peak enhancement of the population in the ground state (Figure 5.3a) is $\simeq$ 1.073 at a chirp value of $\varphi'' = -10^3$ fs^2 and for an excitation wave number of $\tilde{\nu} \simeq$ 19,520 cm^{-1}, which is red-detuned and close to the resonance of the first upper vibrational state at $\tilde{\nu}$ = 19,400 cm^{-1}. The highest suppression is obtained at a chirp of 10^3 fs^2 with a laser central wavenumber of $\tilde{\nu} \simeq$ 20,320 cm^{-1}, which is blue-detuned to the resonance of the second upper vibrational state at $\tilde{\nu}$ = 20,000 cm^{-1}. The asymmetry of the enhancement with respect to the sign of the chirp can be understood as follows. The first half of the interacting laser pulse promotes population inversion, which can be available for stimulated emission depending on the shape of the laser pulse and its spectral components. In the case of the highest enhancement of the population $\rho_{11} + \rho_{22}$, for instance, if we consider that the upper state is first excited at a wave number at $\tilde{\nu} \simeq$ 19,765 cm^{-1}, which corresponds to the beginning of the laser pulse, a vibrational wave packet will be created in the upper state, which will initiate its oscillation between the upper state vibrational sublevels at this particular frequency. The round trip of the wave packet to

the highest vibrational level at $\tilde{\nu}$ = 20,000 cm^{-1} and back to $\tilde{\nu} \simeq$ 19,765 cm^{-1} will take about 23.5 fs. From that time, the resonant transitions of the excited atom or molecule available for stimulated emission will be smaller than 19,765 cm^{-1}, and therefore the red shifted frequencies of the negatively chirped laser pulse will meet them and stimulated transfer back to the ground state will be promoted. This is therefore an adiabatic intra-pulse pump-dump scenario that explains the enhancement observed for negatively chirped pulses. For a laser pulse positively chirped, e.g., at this same central pulse frequency of 19,520 cm^{-1}, however, the later higher frequencies of the pulse cannot promote the system down and will instead continue exciting the system to the upper states. Consequently, the population of the ground state when the laser pulse is gone is not enhanced for positively chirped pulses, as it can be seen in Figure 5.3(a). The results that we obtain with our simple four-level system are therefore fully corroborated by the previous theoretical studies and experimental measurements [197–199]. In Figure 5.4 we have plotted the evolution in time of the populations at some specific values of the central laser pulse wavenumber and chirp. Figure 5.4(a) shows how the maximum enhancement obtained for negatively chirped pulses at 18800 cm^{-1} presents an oscillatory behaviour of $\rho_{11} + \rho_{22}$, while the TL pulse at this wavenumber induces a pump-dump scenario. Note that the transferred population is small at this detuning ($\simeq$5%). This behavior is qualitatively different from the more resonant cases in Figure 5.4b,c, where the pump-dump processes are not that clear and the population transfers become $\simeq$40%.

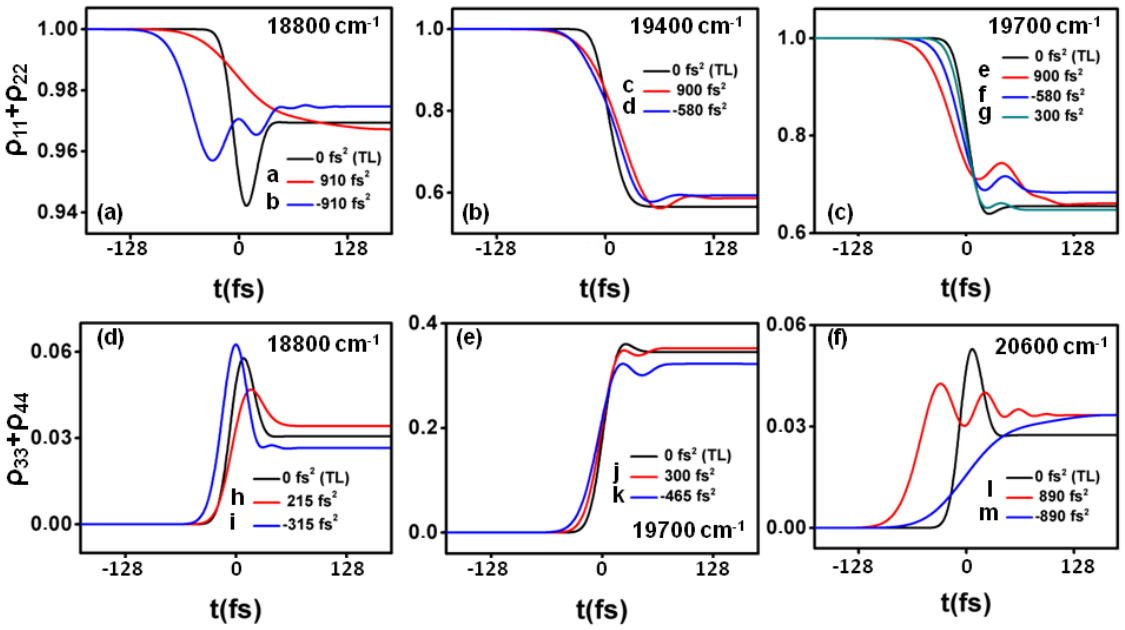

Figure 5.4: Time evolution of the populations in the ground state (**a**–**c**), and in the upper states (**d**–**f**), for specific parameter values, as indicated. Note that the lines, which are named with letters, correspond to the parameter values detailed in Figure 5.6a,e.

II. Coherence in the ground state $|\rho_{12}|$:

The highest enhancement of the coherence in the ground state is ≃1.35 and is obtained at a negative chirp of $\varphi'' \simeq -430$ fs^2 and at the excitation wavenumbers of $\tilde{\nu} \simeq 19{,}660$ cm^{-1} and $\tilde{\nu} \simeq 19{,}150$ cm^{-1} (see Figure 5.3b). The enhancement of the vibrational coherence in the ground states therefore responds basically to the same phenomena that the one for the ground state population, i.e., the pump-dump intra-pulse mechanisms are promoted for negatively chirped pulses and suppressed for positive chirp. The details of the precise values of the two central laser pulse wavenumbers that produce the maximum enhancement are intriguing intra-pulse mechanisms which have not been clarified completely. Our result is in accordance with the

studies made in [196], where it is observed for Oxazine 1 systems in ethanol that ground-state vibrational coherences are enhanced predominantly by negatively chirped pulses. Figure 5.5 shows the evolution in time of the coherences at some specific values of the central laser pulse wavenumber and chirp. In Figure 5.5a the time evolution of the vibrational coherence in the ground states for the two different wave numbers that produce enhancement at negative chirp can be seen, and also the reduction of the coherence $|\rho_{12}|$ after the interaction of the first half of the pulse in the case of positively chirped pulses.

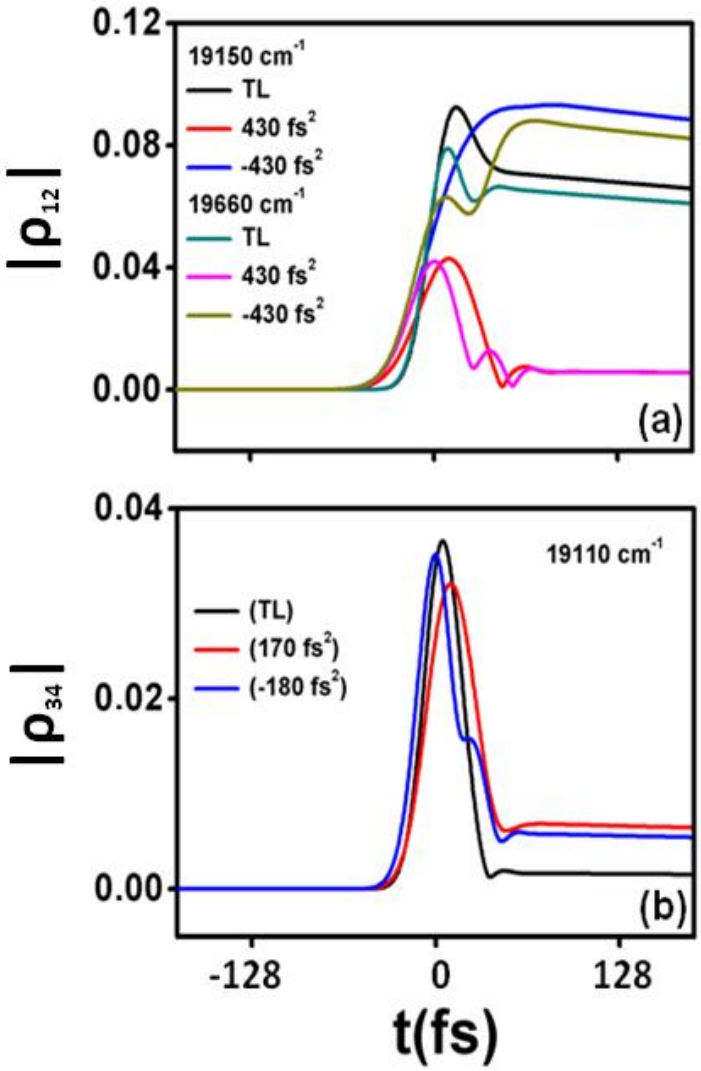

Figure 5.5: Time evolution of the vibrational coherences in the ground state (**a**); and in the upper states (**b**), for the indicated parameter values.

III. Population in the upper states ($\rho_{33} + \rho_{44}$):

Figure 5.3c shows that the peak enhancement in population transfer to the upper states is ≃1.23 at the chirp values $\varphi'' = \pm 10^3$ fs^2 and for an excitation wave number of $\tilde{\nu} \simeq 20{,}550$ cm^{-1}. A qualitatively different smaller enhancement of ≃1.1 is also obtained at the positive chirp $\varphi'' = 260$ fs^2 and for an excitation wave number of $\tilde{\nu} \simeq 18{,}840$ cm^{-1}. The highest suppression is obtained at a close wave number of $\tilde{\nu} \simeq 18{,}920$ cm^{-1} for a negative chirp of $\varphi'' = -10^3$ fs^2. On the one hand, the symmetric enhancement with respect to chirp at $\tilde{\nu} \simeq 20{,}550$ cm^{-1} can be understood by the evolution in time of the population in the upper states for the TL and the chirped pulses at this particular central laser pulse wavenumber, in Figure 5.4f. The behaviour can be seen as the opposite to the effect in the ground state and for red detuned pulses (Figure 5.4a). In this case the oscillatory behaviour corresponds to the positively chirped pulse. On the other hand, the enhancement obtained for red detuned pulses at $\tilde{\nu} \simeq 18{,}800$ cm^{-1} is the consequence of an optimized pump-dump transition, as shown in Figure 5.4d, which as opposed to the enhancement of the population in the ground state; it is favoured by positively chirped pulses, as was also observed in [193–195].

IV. Coherence in the upper states $|\rho_{34}|$:

Figure 5.3d shows two narrow peaks of the upper vibrational coherence that are obtained at a pulse central frequency of $\tilde{\nu} \simeq 19{,}110$ cm^{-1} and for spectral phase chirps as $\varphi'' \simeq -180$ fs^2 and $\varphi'' \simeq 170$ fs^2. The corresponding values are ≃3.56 and ≃4.34, respectively, and therefore a slightly higher enhancement is obtained with positively chirped pulses. Of relevance is the narrow parameters window observed in this case. The nearly symmetric values of the upper vibrational coherence observed in our simulations, however, shows that the vibrational states in the upper levels can be enhanced by relatively small positive or negative chirp values, with a central laser pulse wavenumber red shifted with respect to the resonance of the upper

vibrational levels. This result is partially in accordance with the studies made in [196], where it is shown that excited state vibrational coherences are enhanced predominantly by positively chirped pulses. Figure 5.5b shows the evolution in time of the coherence $|\rho_{34}|$ at the relevant parameter values. It is clear that the two chirped pulses after the interaction of the first half of the pulse are able to retain the $|\rho_{34}|$ coherence as compared to the TL pulse.

5.3.4 Discussion

I. Influence of the Duration of the Laser Pulse

Although a systematic study of all the parameters involved is far from the scope of the present work, we have evaluated the effect of the TL laser pulse duration by repeating some of our simulations using a shorter laser pulse durations (17 fs), and then comparing the results to the ones obtained with the TL 30 fs pulse. Figure 5.6 shows the output obtained for five specific different laser pulse excitation wavenumbers (18,800 cm^{-1}, 19,400 cm^{-1}, 19,700 cm^{-1}, 20,000 cm^{-1} and 20,600 cm^{-1}). As it is indicated, in the left-hand part of the figure (Figure 5.6a,c,e,g) the simulations have been performed with a laser pulse of 30 fs, as in Figure 5.3. The right hand panels (Figure 5.6b,d,f,h) show the results obtained by keeping all the same parameters but using the shorter laser pulse.

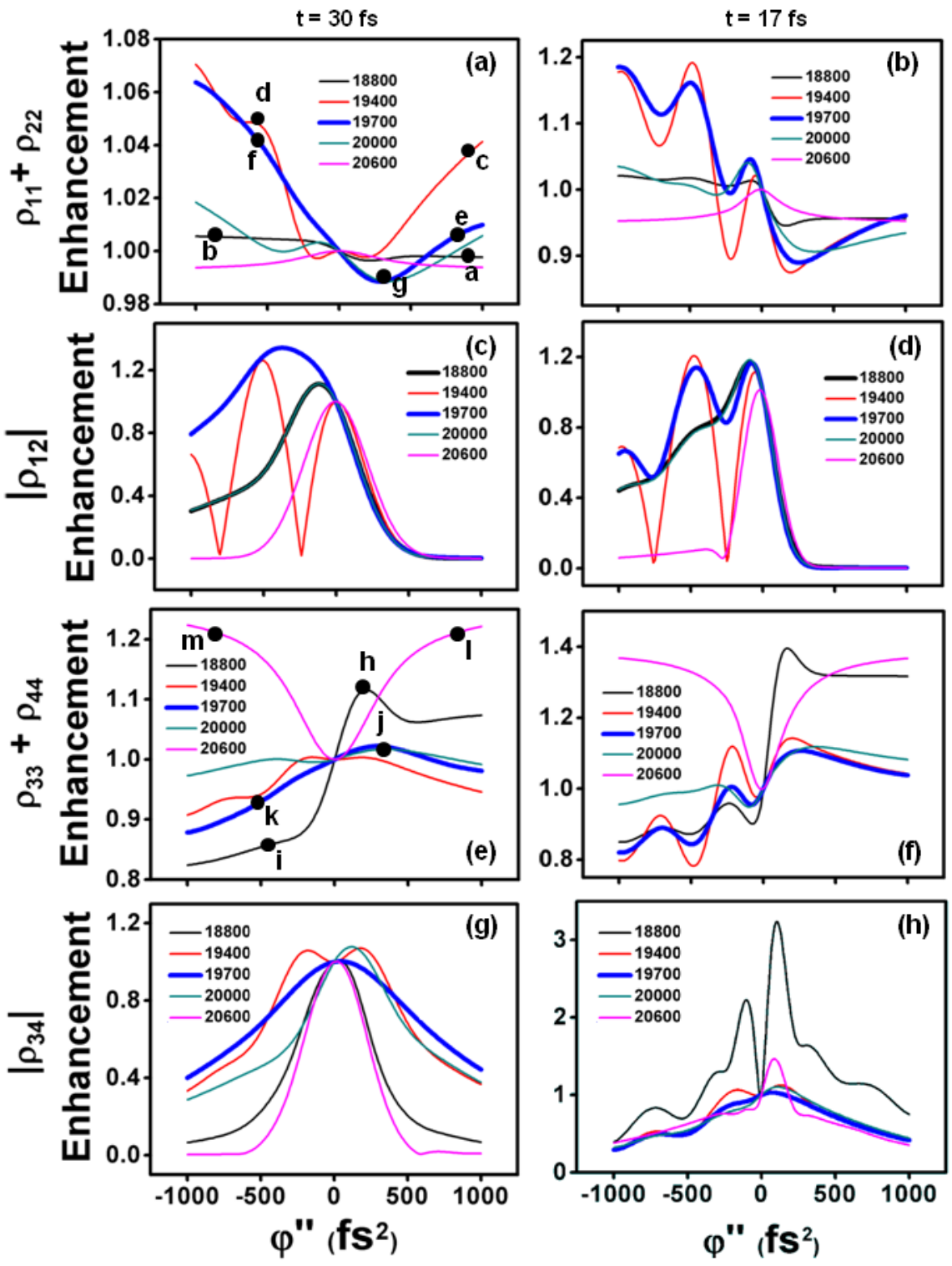

Figure 5.6: Enhancement/suppression factors of (**a**,**b**) population in the ground state; (**c**,**d**) vibrational coherence in the ground state; (**e**,**f**) population in the upper state; and (**g**,**h**) vibrational coherence in the upper state. The right hand panels are for a laser pulse of 30 fs and the right hand panels for 17 fs, as indicated. The coloured

lines represent the different excitation frequencies: 18,800 cm^{-1} (black line), 19,400 cm^{-1} (red line), 19,700 cm^{-1} (blue line), 20,000 cm^{-1} (dark cyan line), and 20,600 cm^{-1} (magenta line). The electronic dephasing time is 100 fs for all cases. A bold (blue) line has been chosen for the excitation wavenumber of 19,700 cm^{-1}, in order to clarify the comparisons with Figure 5.8.

The results in the left hand side of Figure 5.6 are cuts of the density maps shown in Figure 5.3 at specific excitation wavenumbers. The right hand side panels obtained for 17 fs show basically the same qualitative behaviour as the ones obtained for 30 fs, except that we observe some undulations of the enhancement factors as the chirp is varied. An overall increase in the value of their maximum is also observed. The observed undulation may occur due to the larger effect of chirp on the shorter 17 fs pulse, since its duration for $\varphi'' = \pm 10^3$ fs^2 results in $\simeq$159 fs, i.e., it is longer than the 94 fs that correspond to the 30 fs pulse at these chirp values. The longer time broadening of the 17 fs pulse hence allows the upper state vibration to make several oscillations ($T_{vib} \simeq 60$ fs) during the intrapulse interaction, and can thus explain the observed enhancement undulations. The overall highest value of the enhancement factors obtained can be explained by the broader spectral wavelength of the 17 fs laser pulse ($\simeq$ 865 cm^{-1}), which in this case covers all the resonant energies of the upper states, and therefore more resonant transitions become available. The maximum enhancement obtained with positively chirped pulses for the population in the upper state is in this case $\simeq$1.4, at $\tilde{\nu}$ = 18,800 and with φ'' = 168.5 fs^2 (Figure 5.6f). For the coherence in the upper state the maximum enhancement is $\simeq$3.2 at $\tilde{\nu}$ = 18,800 and for φ'' = 168.5 fs^2 (Figure 5h).

II. Influence of the Laser Peak Intensity

It is also worth noting that the Rabi period in the present simulations, as mentioned above, is $\simeq$180 fs, which means that during the interaction times that we have considered ($\lesssim$90 fs) the

system is in the exciting half of the Rabi cycle. We have performed simulations by doubling the amplitude of the interacting pulse so that the Rabi period becomes of ≃90 fs. We would expect a response of the system to the fact that most of the interaction is produced during a whole Rabi cycle, but the results that we obtain are qualitatively the same as those described for a Rabi period of ≃180 fs. The only difference that we observe is quantitative, as shown in figure 5.7a – d. We obtain a higher enhancement factor of ≃3.2 for the population in $\rho_{11} + \rho_{22}$. The maximum enhancement of $|\rho_{12}|$ results in ≃1.6, and for $\rho_{33} + \rho_{44}$ is ≃2.1. Of relevance, however, is the maximum enhancement factor in $|\rho_{34}|$, which becomes in this case ≃38.5. This large value is observed close to the resonance of the first vibrational upper state level, with $\tilde{\nu} \simeq 19{,}365\ \mathrm{cm}^{-1}$ and for two almost symmetric chirp values, namely $\varphi'' \simeq -210\ \mathrm{fs}^2$ and $\varphi'' \simeq 220\ \mathrm{fs}^2$ (see Figure 5.7e).

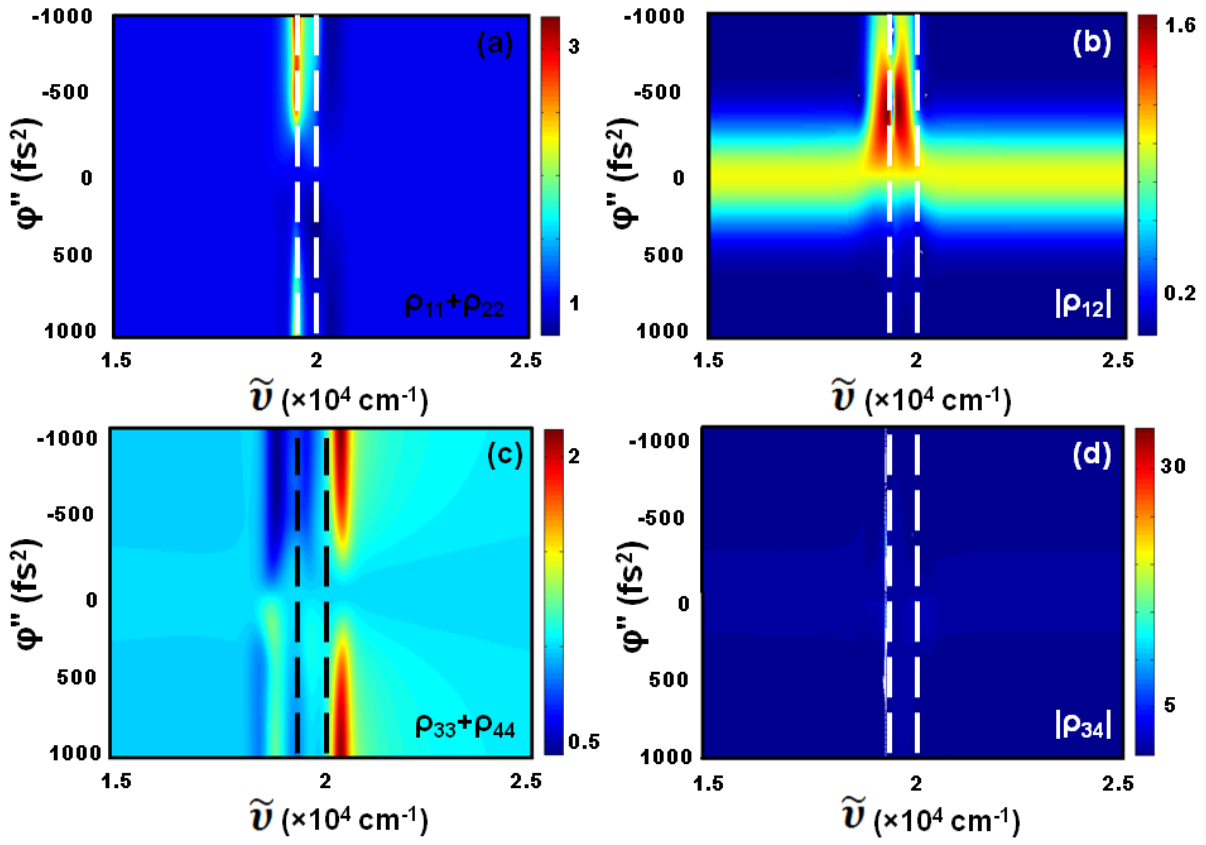

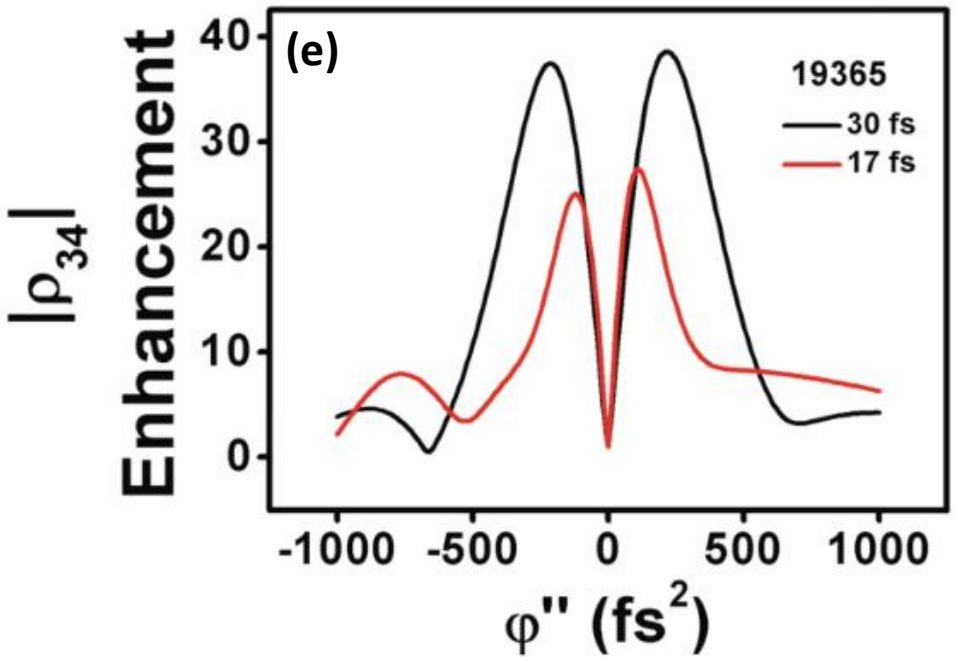

Figure 5.7: Enhancement/suppression factor for complete Rabi oscillation of (**a**) population in the ground state; (**b**) vibrational coherence in the ground state; (**c**) population in the upper state; and (**d**) vibrational coherence in the upper state. Dashed lines indicate the position of the excited states (see Figure 5.2). **(e)** Enhancement of in $|\rho_{34}|$ with $\tilde{\nu} \simeq 19{,}365\ \mathrm{cm}^{-1}$ and for pulse durations of 30 fs and 17 fs, as indicated.

III. Influence of the Electronic Dephasing

In all simulations above, the electronic dephasing ($T_{2,elec} \equiv \Gamma_{ij}^{-1}$) was kept constant at 100 fs. The role of the electronic dephasing, however, has been already experimentally observed and theoretically discussed in several coherent control experiments of small and large molecular systems. In general, the magnitude of electronic dephasing of a given electronic transition determines how fast the induced dipole coherently oscillates after interacting with the laser electric field. In this regard, molecular systems with very fast electronic dephasing rates will be potentially less affected by, e.g., long tailored excitations than by shorter laser pulses, since

the electronic coherence already dephases faster in the former case. We have considered the influence of electronic dephasing by studying the specific values $T_{2,elec}$ = 5 fs, 25 fs, 50 fs, 100 fs and 200 fs with a TL laser pulse of 30 fs centered at 19,700 cm^{-1}. The case of $T_{2,elec}$ = 100 fs corresponds to the one considered in Figure 5.6 (left panels) and it is shown with thicker blue lines, both in Figures 5.6 and 5.8, for a clearer comparison.

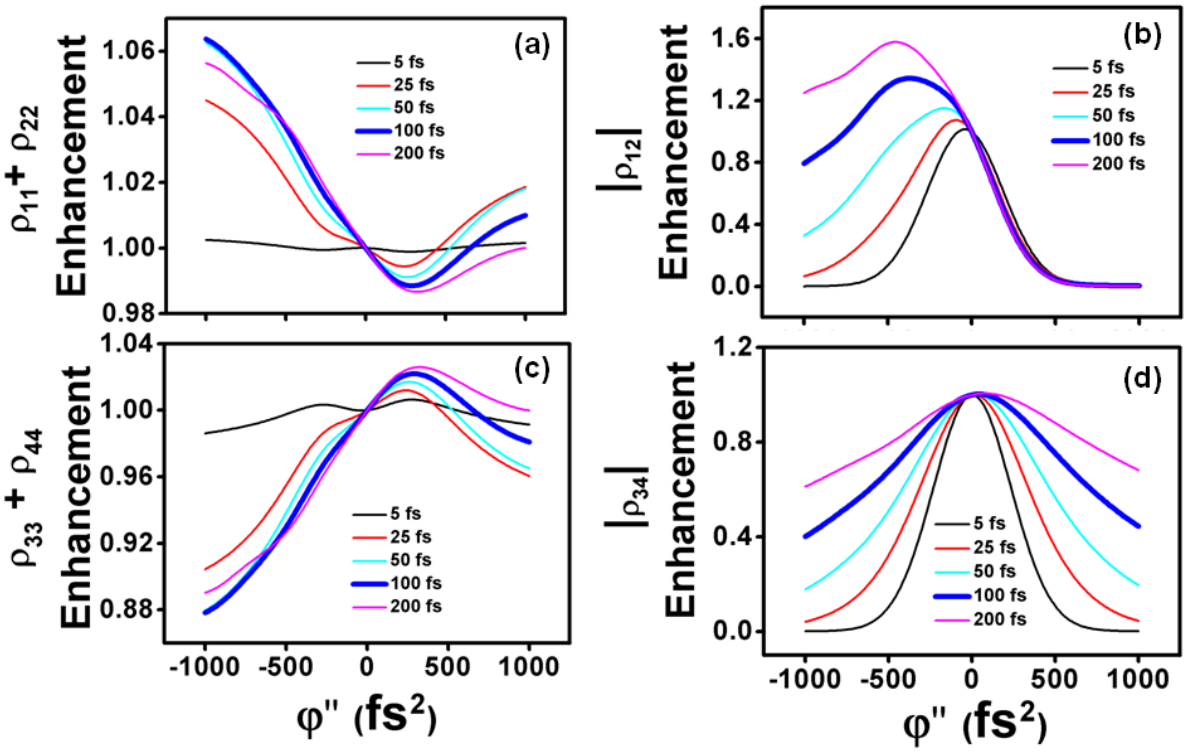

Figure 5.8: Influence of electronic dephasing ($T_{2,elec}$ = 5 fs, 25 fs, 50 fs, 100 fs and 200 fs, as indicated) on the enhancement of (**a**) population in the ground state; (**b**) vibrational coherence in the ground state; (**c**) population in the upper state; and (**d**) vibrational coherence in the upper state, considering an excitation frequency of 19,700 cm^{-1}. The bold blue lines show the electronic dephasing time $T_{2,elec}$ = 100 fs for a clearer comparison with Figure 5.6.

The results in Figure 5.8 are basically expected. They show how a faster electronic dephasing destroys the enhancement/suppression effect of the chirped pulses both in the populations of

the ground and excited states (Figure 5.8a,c), so that for $T_{2,elec}$ = 5 fs no enhancement/suppression is obtained. This is clearly due to the lack of population transfer at this fast dephasing time. The vibrational coherences of the ground and upper states show a decrease in the enhancement in all cases as the dephasing times are reduced, and they also show a clear symmetric reduction for increasing positive and negative values of chirp as compared with the TL interaction (Figure 5.8b,d).

5.4 Conclusions

The numerical calculations reported in this work produced two major results. The first one is the clear enhancement of population and vibrational coherence for near-resonant excitation obtained by using chirped laser pulses (Figure 5.6a,b,e,f). The enhancement of the population and the vibrational coherences in the upper and ground states differ, though, in the sign of the chirp and the direction of the detuning. While population transfer due to pump-dump processes from the ground and back to the ground states is maximized for negative chirp, when the laser is tuned near the lowest upper vibrational state (level $|3\rangle$), enhancement of the population in the excited states is obtained both for positive and negative chirps, with a central laser wavelength slightly tuned above the upper vibrational states. The simulations show that the enhancement of the ground vibrational states is obtained by negatively chirped pulses slightly tuned above and below level $|3\rangle$, while the enhancement of the excited state vibrations is observed in a tiny region with both positive and negative small chirps and the laser slightly tuned below level $|3\rangle$.

The second major result is the absence of population enhancement in the upper states using chirped pulses, when their spectra are resonant with the transition (Figure 5.6e,f). Also important is the lack of any substantial change in the population enhancement with resonant chirped pulses when molecular electronic dephasing is increased to 200 fs (Figure 5.8c). This

clearly indicates how robust this result is for a wide range of molecular systems. Perhaps even more importantly, these findings hint at why coherent control experiments of photochemical reactions in electronic excited states, which often use electronic resonant tailored excitations, have been challenging in many cases [49, 201, 202].

In conclusion, a numerical study on coherent control via chirped pulses in a four-level system was performed by considering specific parameters typical of Oxazine systems. We have studied in detail the influence of the detuning of the laser input pulse with respect to the electronic transitions. We have evaluated in some particular cases the effect of the duration of the laser pulse, its peak intensity, and also the influence of the electronic dephasing. It is shown that the time ordering of frequencies inside a pulse makes a fundamental difference in the population transfer and vibrational coherence generation, which can be computed with our four-level model. Intra-pulse adiabatic mechanisms explain most of the enhancement effects that we have observed. Although the results that have been presented are obtained for specific parameter values, the numerical model that has been studied is sufficiently simple to allow for an extension of these findings to other systems. An advance in the understanding of these light-matter interaction processes could open up new pathways and ideas in the field of nonlinear quantum control spectroscopy [141].

Chapter 6

Attosecond Transient Absorption Spectroscopy of Krypton Using the Density Matrix Formalism

Transient absorption spectroscopy has been a ubiquitous measurement technique in the femtosecond timescale and recently extended to the attosecond regime by means of high harmonic generation (HHG) [57] in terms of electron dynamics as it unfolds on few femtosecond (1 fs = 10^{-15} s) to attosecond (1 as = 10^{-18} s) timescales. Pump-probe technique allows for the study of ultrafast atomic and molecular behaviour/dynamics on different wavelengths from the ultraviolet (UV) to near infrared (NIR) wavelengths. With the introduction of XUV pulses, attosecond transient absorption spectroscopy (ATAS) using pump-probe method can be employed to study the electronic motion of atoms on their natural occurring timescale. ATAS has been used to demonstrate numerous time-resolved studies and control of electron dynamics in the core of atoms [203], molecules [204] and even in solid-state systems on attosecond temporal resolutions. Studies like motion of electron wavepacket during ionization process and control of population and quantum phases of ionic states can be achieved using ATAS [205].

In this chapter, we will present simulations using the density matrix formalism that support experimental measurements performed by the group of Professor Jozsef Seres in Vienna (Austria). We will first take a look at the concept of ATAS and how extension to the attosecond timescale has broadened our comprehension of the dynamics of atomic and molecular systems. Some applications of ATAS will be discussed. The theory of ATAS and its relationship with the density matrix formalism will be presented. For instance, the need for avoiding the RWA will be explained and some relevant parameters that influence the study

will be discussed. Finally, the joint theoretical and experimental study of attosecond physics will be presented.

From the theoretical view, we are going to apply the density matrix analysis to examine core transitions of krypton using attosecond pulse trains from a HHG source. The dressing process is modelled using the DM equation to theoretically describe the experimentally observed XUV transmission dynamics and both the linear and non-linear dressing oscillations. The study is carried out for cases of weak and strong ionization and atomic polarization response (material response) in krypton core transition is examined. Quantum beats between the sub-levels of krypton are discussed. Experimentally, two measurement techniques are utilized; transient absorption spectroscopy and Fourier-transform spectroscopy. The former is used to study laser dressing dynamics in Kr for spectral ranges 205 – 230 eV where transient spectroscopy of Kr had not been covered before especially with attosecond resolution. The latter is used to experimentally identify quantum beats between 3d and 3p sub-levels of Kr.

6.1 Theory of Attosecond Transient Absorption spectroscopy

ATAS similar to femtosecond transient absorption using pump-probe method involves two pulses (one for probing and the other for excitation) with a delay between these pulses. In the case of ATAS, the goal is to achieve interior shell excitation in the target atomic system by extending the excitation and probing field photon energies to extreme ultraviolet (XUV) and x-ray regimes [205]. ATAS is used to study electron motion in atoms in few femtosecond and attosecond timescales and corresponds to excitation energies of sub-eV to several eV respectively. This can enable us to extract more information about the populations and

quantum phases of ionic states [206] which can in turn facilitate probing and extraction of electron dynamics on their natural timescale.

As stated earlier, two pulses are involved in ATAS. The first pulse is a strong field NIR sub-cycle fs pulse used for excitation causing certain changes in the electronic dynamics of the target atom by modifying unoccupied levels of the atom, this process is referred to as the laser dressing. The delayed second pulse is a weak field attosecond XUV pulse which could be a single XUV pulse or train of XUV pulses used for interrogating the observed changes of the newly laser dressed atom [as shown in figure 6.1]. A controlled temporal delay exists between these pulses with an attosecond time resolution that can be varied. The variation induces a delay-dependent XUV absorption spectrum, which together with the induced macroscopic polarization $\vec{P}(t)$ gives information about the dynamics induced by the IR field.

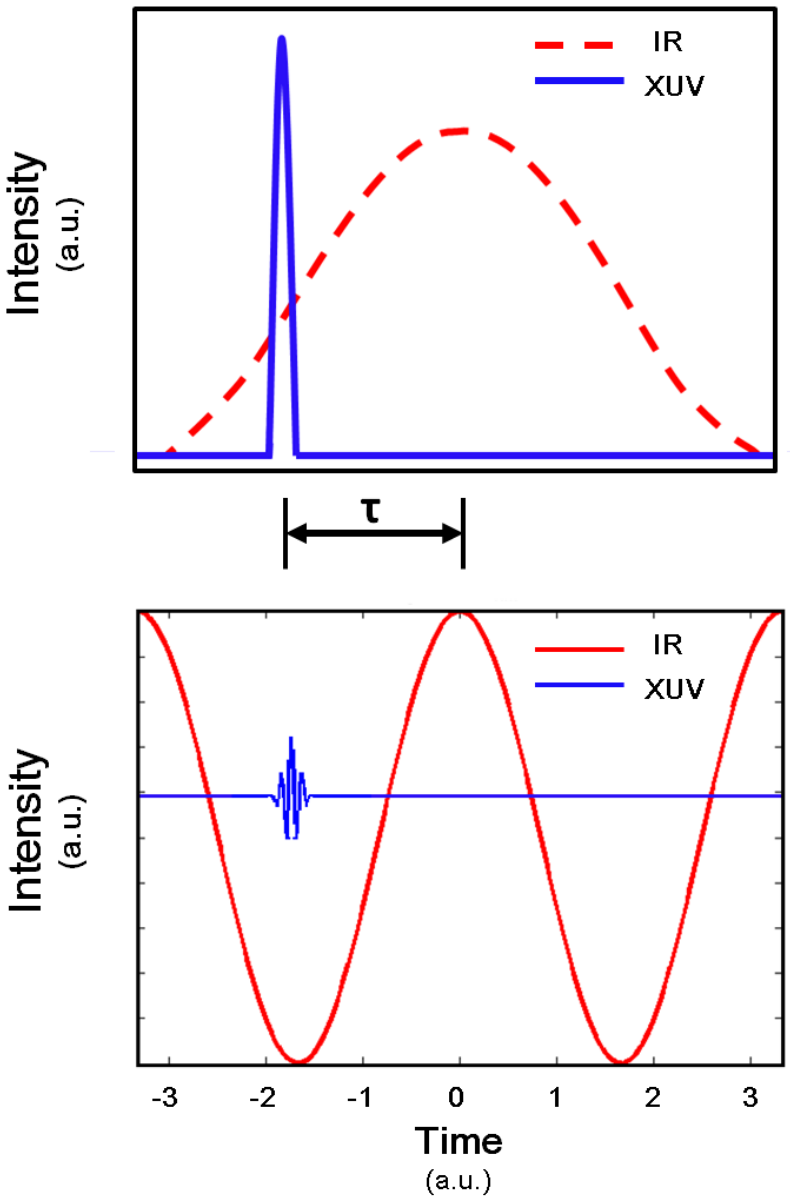

Figure 6.1: Schematic representation of the fs IR pulse and as XUV pulse in the frequency and time with a delay τ between both pulses for the ATAS experiments.

I. High harmonic generation (HHG) and XUV pulses

HHG is a non-perturbative process where an intense optical IR field (with intensity exceeding 10^{14} W/cm^2 for attosecond pulse generation) interacting with a gas atom, undergoes certain frequency conversion through a highly non-linear processes [80]. The HHG process is used to generate the attosecond XUV radiation as single pulses or as a train of pulses which

synchronizes with the IR pulse [207]. The higher-order harmonics that create these ultrashort XUV fields with very broad spectral bandwidth (in the range of tens of electron volts, eV) are due to strong field non-linear interactions between intense laser pulses with high electric field strength and the noble gas target (an example is jet of Neon gas) [208].

A prominent description of the generation of XUV fields by HHG is the 3-step model introduced by Corkum [208] which involves electrons being ionized due to the strong IR field (typically by tunnel ionization), driven in the continuum by the IR field, and finally recombining with the parent ion to produce XUV photons. Several methods using HHG have been proposed to generate isolated attosecond XUV pulses or train of pulses for the primary aim of electron dynamics probing [209] on relevant timescales, which has opened pathways for numerous applications. Formation of hole wavepackets and measurement of coherence of the hole wavepackets have been demonstrated using ATAS [210]. Other applications of ATAS include observation of AC Stark shifts of excited states in Argon [211] and Krypton [212], probing population transfer and coherence generation between ionic states through ion density matrix of atoms [213]. An important application is the study of the time-resolved electronic dynamics of autoionizing states like hole creation dynamics and electron motion in the valence shell of these atomic systems.

II. Mathematical representation

In attosecond absorption spectroscopy, a strong IR electromagnetic field together with a weak XUV pulse interact with an atom target. In order to elucidate the temporal-dependent XUV absorption spectrum, the field is treated classically and the target atom quantum mechanically, resulting in a semi-classical analysis of the dynamic processes. In this thesis, we analyse these processes using the density matrix formalism beyond the RWA, which in this case cannot be applied due to the high intensity of the IR pulse and the short timescales involved [214]. First,

the intensity I_{out} after interaction can be represented by the relationship between the transmission signal, T and the incident pulse, I_{in} as

$$I_{out} = I_{in} \exp\left\{-\frac{4\pi\omega NL}{c}\mathrm{Im}\left(\frac{\tilde{P}(\omega)}{\tilde{E}_{in}(\omega)}\right)\right\} \qquad (6.1)$$

$$T = \exp\left\{-\frac{4\pi\omega NL}{c}\mathrm{Im}\left(\frac{\tilde{P}(\omega)}{\tilde{E}_{in}(\omega)}\right)\right\} \qquad (6.2)$$

$$T = \frac{I_{out}}{I_{in}} \qquad (6.3)$$

In cases of experimental measurements, the absorption, A, is vital and is related to the Transmission signal in equation (6.2) and (6.3) by the Beer-Lambert's law [215] given by

$$A = -\ln \mathrm{T} = -\ln\left\{\frac{I_{out}}{I_{in}}\right\} \qquad (6.4)$$

$$A = \frac{4\pi\omega NL}{c}\mathrm{Im}\left(\frac{\tilde{P}(\omega)}{\tilde{E}_{in}(\omega)}\right) \qquad (6.5)$$

Where, N is the density of the target atomic system, L is the interaction length. $\widetilde{\mathrm{P}}$ is the polarization, $\widetilde{\mathrm{E}}_{\mathrm{in}}$ is the electric field strength of the incident laser pulse. $I_{in} = \left|\tilde{E}_{in}\right|^2$ and $I_{out} = \left|\tilde{E}_{out}\right|^2$ are the incident and transmitted pulse intensities.

As commented above, in the density matrix analysis, we have to study the light-matter interaction processes by going beyond the RWA. Indeed, experiments involving HHG field are very sensitive to the field waveform rather than the envelope of the field, thereby laying emphasis on precise phase control.

The polarization $\widetilde{\mathrm{P}}$ can be calculated by taking a trace of the product of the density matrix ρ and the transitional dipole matrix, $\vec{\mu}$, given by

$$\tilde{P} = \mathrm{Tr}\,(\rho \cdot \vec{\mu}) = 2\mu_{ij}\mathrm{Re}\{\rho_{ij}\} \qquad (6.6)$$

The equation (6.6) represents the atomic polarization response.

The density matrix will be used to interpret precisely the dynamics of the laser dressed system observed in the experiments, which will be demonstrated for core-transitions in krypton.

6.2 Attosecond sublevel beating and nonlinear dressing on core-transitions in krypton

Extreme ultraviolet (XUV) transient absorption spectroscopy has been widely used to examine the quantum effect of intense laser fields on atoms, molecules and solids. It is known as laser dressing and the examined object is illuminated with a laser field strong enough to modify, by its electric field, the unoccupied quantum levels. A weak XUV field is used as probe to measure the changes of the levels by means of time-resolved (or transient) x-ray absorption spectroscopy.

Krypton atoms were experimentally examined by illuminating them with ultrashort laser pulses within a wide intensity range of 4×10^{13} W/cm² to 6×10^{14} W/cm². The dynamics of the two laser dressed transitions $3d_{5/2}$–$5p_{3/2}$ and $3p_{3/2}$–$5s_{1/2}$ at photon energies of 91.3 eV and 210.4 eV, respectively, and their spectral surrounds were examined with attosecond temporal resolution using attosecond pulse trains generated in Ne gas by a Ti:sapphire laser. The dressing process was modelled with density matrix equations and the experimental and theoretical results were compared. It was demonstrated that density matrix equations describe very accurately the experimentally observed femtosecond and attosecond-scale transmission dynamics and also the linear and second order non-linear dressing oscillations at 0.75 PHz

and 1.5 PHz frequencies. Furthermore, quantum beats between the $3d_{5/2}$ and $3d_{3/2}$ sub-levels at 0.3 PHz and between the $3p_{3/2}$ and $3p_{1/2}$ sub-levels at 2.0 PHz were experimentally identified and resolved.

6.2.1 Introduction

Intense laser fields interact with atoms, molecules and even solids non-adiabatically by producing transient changes in their occupied or unoccupied electronic quantum states. The response of the material to this so called dressing is typically very fast lying in the few PHz and sub-PHz frequency range. Attosecond transient absorption spectroscopy (ATAS) [216] is a suitable spectroscopy tool to follow and study such a fast material responses. Revealing PHz-scale responses of materials helps in developing and improving coherent extreme ultraviolet (XUV) [59, 217, 218] and soft X-ray (SXR) [219-221] light sources by means of high harmonic generation (HHG) and to extend the operational speed of different optoelectronic detectors [222].

Nowadays, ATAS is extensively applied to study intense laser field dressed solids like Si [223, 224], diamond [225], Zr [224], by probing valence or core electrons. Gases like helium [226-229], neon [230] and H_2 [231] were mainly probed by their valence electrons at around and below 20 eV with attosecond or femtosecond resolution. Probing core level electronic states in atoms or molecules is more challenging because they require HHG sources with much higher photon energies, where the conversion efficiency of HHG is typically low. Consequently, mainly Xe gas [214, 232, 233] and two-electron transitions in He [234] have been studied at around 60 eV, and time resolved spectroscopy at higher photon energies were rare [235-238] and gave mainly femtosecond resolution even in solids [239-241].

The aim was to measure the time-resolved XUV absorption of neutral Kr gas. ATAS of krypton was earlier measured [235] at its ionized states. In the case of neutral krypton, a

strong absorption can be observed between 90 and 95 eV containing several transitions between the occupied 3d inner-shell and the unoccupied np levels [242, 243], and transitions from the 3p inner-shell at around 210 eV have also been measured [244-246].

The generated HHG spectrum that was used as probe covered the spectral range from 70 eV to 230 eV, making it possible to study both types of core level transitions i.e. the excitations from the sublevels of the 3d and 3p electronic states. The study of these transitions in Kr was motivated by the fact that the distance between the 5s and 5p levels is 1.52 eV, which is within the bandwidth of the dressing laser pulse (central energy was at 1.55 eV). Consequently, the 5s and 5p levels were resonantly coupled by the dressing laser field and a strong dressing effect was predicted for both the $3d_{5/2}$-to-$5p_{3/2}$ and $3p_{3/2}$-to-$5s_{1/2}$ transitions at 91.3 eV and 210.4 eV, respectively. Furthermore, since the 5p and 6p levels have an energy-difference of 1.3 eV, it was also close to resonance with the laser field.

6.2.2 Experimental setup and examined transitions of krypton

In the experimental arrangement, similarly to earlier measurements [224], a concentric mirror-pair focused the 25-fs-long pulses of a Ti:sapphire laser system to two gas sources, see figure 6.2(a). The inner mirror focused the 6 mJ/pulse portion of the laser beam to a jet containing Ne gas for HHG serving as probe pulse. The beam diameter in the focus was 110 μm giving a peak intensity of about 1.5×10^{15} W/cm², a suitably large one to produce harmonics up to the cut-off energy of about 300 eV. Zr thin-film filter was placed before the XUV spectrograph (McPherson 248/310G with multichannel plate) to suppress all light below 50 eV. The gas jet was a tube with small holes and had a diameter of 1 mm to block the laser beam as little as possible, focused by the outer mirror. The generated harmonic spectrum covered a wide spectral range from about 70 eV to 230 eV [figure 6.2(b)] at the optimal backing pressure of

the Ne gas of 1.6 bar. Harmonic lines at different parts of the spectrum are well recognizable. For calibration purpose, 100-nm-thick Si foil was used in certain measurements of which L-edge can be seen in figure 6.2(b) at about 100 eV.

The generated divergent HHG beam passed through the 1 mm diameter hole of the second gas jet (tube with 3 mm diameter) placed 500 mm from the HHG source. This contained the examined Kr gas and the HHG beam probed the transmission change in Kr produced by the dressing laser field. For dressing/pump, the outer mirror focused a conical beam to the Kr gas. In the focus, the outer mirror produced a ring structure with a well distinguishable intense central beam part. The laser energy reaching the outer mirror was controlled with a motorized aperture. In the experiments, the estimated laser peak intensity in the Kr gas was varied between 4×10^{13} and 6×10^{14} W/cm². Using a suitable distance between the gas jets, the intensity originated from the divergent laser beam of the inner mirror added less than 2% to the dressing intensity, what was negligible since it was comparable or less than the shot-to-shot fluctuation of the laser system. The internal movable mirror allowed scanning the delay between the generated harmonic pulses and the dressing laser beam.

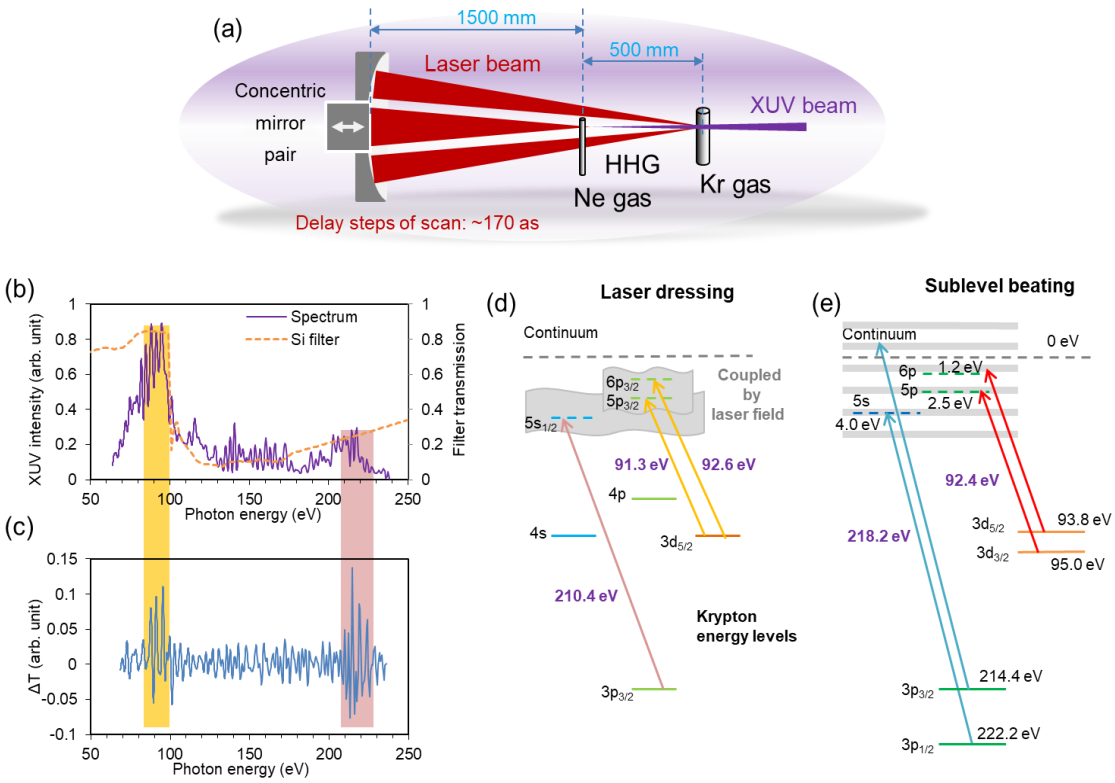

Figure 6.2: (a) In the experimental setup, a concentric mirror pair focused the inner and outer parts of the laser beam to two gas jets serving as HHG source for probe and for pump. (b) The high harmonic spectrum generated for probe covered the spectral range from about 70 eV to 230 eV. (c) The averaged change along the delay scan shows the two spectral ranges where the effect on the Kr gas was observed, namely between 85-100 eV and 205-230 eV. (d) Within these spectral ranges, two laser dressed transitions: the transition from $3p_{3/2}$ to the dressed $5s_{1/2}$ at 210.4 eV and the transition from $3d_{5/2}$ to the dressed $5p_{3/2}$ at 91.3 eV furthermore beating between 3p and 3d sublevels were examined. The few occupied (solid lines) and unoccupied (dashed lines) states of the krypton atom being within our interest are given.

The generated harmonic spectrum was well suitable to probe the two laser-dressed transitions in Kr gas presented in figure 6.2(d) or the sublevel beating presented in figure 6.2(e). The backing pressure of Kr was chosen to 1.2 bar to be mainly transparent but to produce measurable absorption at the two transitions $3d^{-1}5p$ at 91.3 eV and $3p^{-1}5s$ at 210.4 eV [243, 246]. The transmission change along a delay scan was averaged in Fig. 6.2(c) to determine and demonstrate the spectral ranges where laser dressing and beating took effect. Well distinguished changes can be observed in the spectral range of 85-100 eV and 205-230 eV, around the two particular transitions. Some weaker change can also be observed between the two spectral ranges, which can be attributed to the effect of the laser dressing to the 3d to continuum transitions and is out of the interest of the present study.

In the experiment, an attosecond pulse train (APT) was used to probe transient absorption. Since the probe pulses are weak, i.e. the absorption can be considered as linear (no saturation of absorption), and the temporal distance between the pulses in the APT is uniform, APT is suitable for attosecond pump-probe measurements. It can measure processes with time constant shorter than the optical half-cycle or longer than the optical pulse, what was within the scope of the experimental measurements.

6.2.3 Beating between 3p and 3d sublevels in krypton

Beating can be expected when two transitions are possible at the same time with close photon energies. As presented in figure 6.2(e), two possible beating channels are possible in the spectral range of this study: between the $3d_{3/2}$ and $3d_{1/2}$ sublevels and between the $3p_{1/2}$ and $3p_{3/2}$ sublevels. In the case of 3d shell, the distance between the two sublevels is 1.2 eV, which means a beat frequency of $2\nu_B = \Delta E/h$ = 0.29 PHz, what is within the ±0.02 PHz measurement accuracy of the observed 0.3 PHz frequency. Because the 1.3 eV distance

between 5p and 6p levels was almost the same as the distance between the 3d sublevels, the transitions $3d_{1/2} - 5p_{3/2}$ and $3d_{3/2} - 6p_{1/2}$ and their dressed levels were probed at the same time giving one of the possible channels of beating, which had to appear periodically in the spectrum. This channel is noted with red arrows in figure 6.2(e). The other possible beating channel was the transitions from both sublevels into the continuum, and the associated beating had to appear continuously above 95 eV.

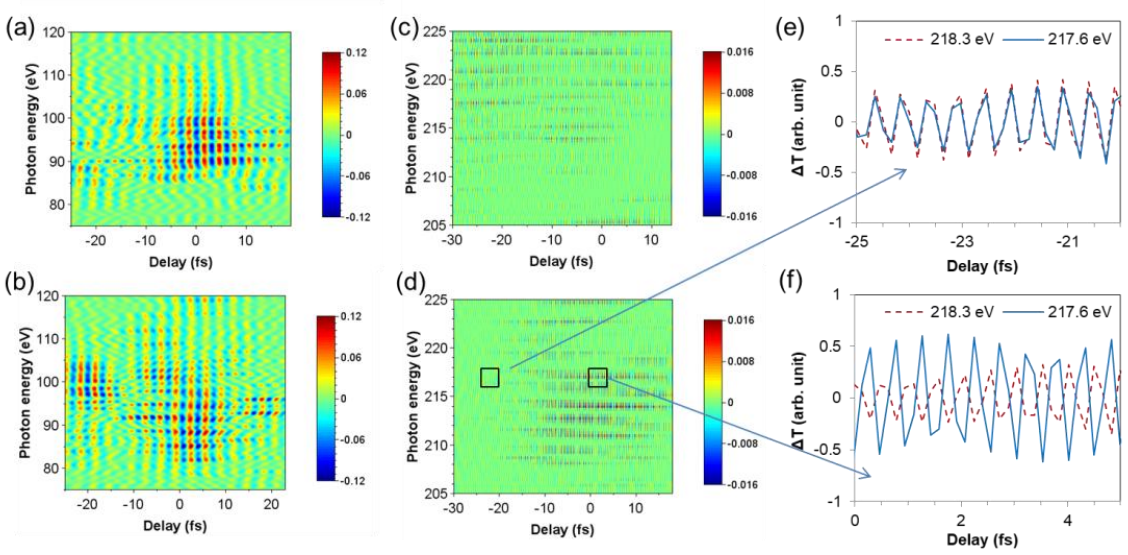

Figure 6.3: Beat signal were calculated from the measurements by applying a Fourier window on the (a), (b) 0.3 PHz beat frequency in the case of 3d levels and (c), (d) on the 2 PHz beat frequency for 3p levels at laser intensities of (a), (c) 4×10^{13} W/cm^2 and (b), (d) 8×10^{13} W/cm^2. In panels (e) and (f), the delay dependence of the transmission changes were compared at two nearby photon energies at the $3p_{1/2} - 5s_{-1/2}$ transition at around 218.2 eV.

Similar beating channels should be observed in the case of the 3p level, where the distance between the sublevels is 7.8 eV, giving a beat frequency of $2\nu_B$ = 1.9 PHz that is very close to the observed 2 PHz peak, which gave an 8.2 eV measured difference between the sublevels. Note that from the available literature [244–246] the origin and the accuracy of

these level-energies cannot be concluded. The possible channel of the beating from the 3p levels is presented in figure 6.2(e) with blue arrows. Similarly to the 3d level, there should be a spectrally periodic beating produced by the transitions $3p_{1/2} - 5s_{1/2}$ at 218.2 eV and its dressed levels, and the transition from $3p_{3/2}$ to the continuum. The other possible channel was the transition from the 3p sublevels to the continuum, similarly to 3d shell, giving a continuous beating beyond 222 eV.

To observe the beating and separate it from other processes, the delay dependent signal was Fourier transformed and Fourier filters were applied to the measured data sets with a window selecting only the 0.3 PHz peak in the case of 3d levels and the 2 PHz peak for 3p levels. More details about the Fourier filtering will be given Section 6.2.4. The results can be seen in Figures 6.3(a)-6.3(d) for dressing laser intensities of (a), (c) 4×10^{13} W/cm^2 and (b), (d) 8×10^{13} W/cm^2. In the case of 3d levels [Figures 6.3(a) and 6.3(b)], the beating was very well visible and appeared mainly between -10 fs and +10 fs delays, where the laser intensity was the highest and the spectral periodicity can be observed for both intensities. At the higher intensity, the beating spread over a boarder spectral range, as it can be expected, while the higher laser intensity produced more high-order dressed levels. The continuous beating contribution can mainly be seen between -20 fs and -10 fs delay at around 100 eV, where there was no periodic beating. In the case of 3p levels [Figure 6.3(c) and 6.3(d)], the beating was relatively weak at lower laser intensity [Figure 6.3(c)] and appeared mainly at higher photon energies and the continuous contribution dominated. However, at higher intensity [Figure 6.3(d)], it was spectrally periodic and it appeared in the -10 fs to +10 fs delay range, as it was expected. More details were resolved at the $3p_{1/2} - 5s_{-1/2}$ transition at around 218.2 eV. The black frames in Figure 6.3(d) show the delay ranges where transmissions were plotted separately in Figures 6.3(e) and 6.3(f) and at two neighbour photon energies just below and above the transition. Figure 6.3(e) shows the XUV transmission at negative delay

before strong dressing. Here, the beatings were weak and in phase. At around zero delay in Figure 6.3(f), where the laser intensity and consequently the dressing and beating were strong, and the phase between the two photon energies changed to inverse. To understand fully the detailed behaviour of the beating, development of a suitable theoretical model and further examinations are needed.

6.2.4 Dynamics of laser dressing in krypton

As presented in Figure 6.2(d), two types of possible core transition can be studied by the broad HHG spectrum that was generated, namely the $3d_{5/2}$-to-$5p_{3/2}$ and $3p_{3/2}$-to-$5s_{1/2}$ transitions at 91.3 eV and 210.4 eV, respectively. The energy difference between the $5s_{1/2}$ and $5p_{3/2}$ levels of Kr is 1.52 eV, which gave a unique opportunity to couple these levels resonantly with short Ti:sapphire laser pulses, and due to this coupling a strong dressing effect was expected. It was studied theoretically and experimentally.

I. Theoretical predictions of the laser dressing on the XUV transmissions

To make predictions about the expected effect of the laser dressing and for comparison with measurements, calculations were performed. Density matrix equations were used beyond the rotating wave approximation (RWA), since this approximation is unsuitable when the field strength of the control IR field is in the high-field regime [247]. To follow the processes for the $3d^{-1}5p$ transition, 4 levels were taken into account, namely 3d, 5s, 5p, and 6p. Note that the $3d^{-1}6p$ (92.6 eV) transition was included in the calculation since it is close to one of the dressed states of $3d^{-1}5p$, as mentioned above. The four-level system equations correspond to a double-Λ configuration [84] shown in figure 6.4 and read (Equation 6.7)

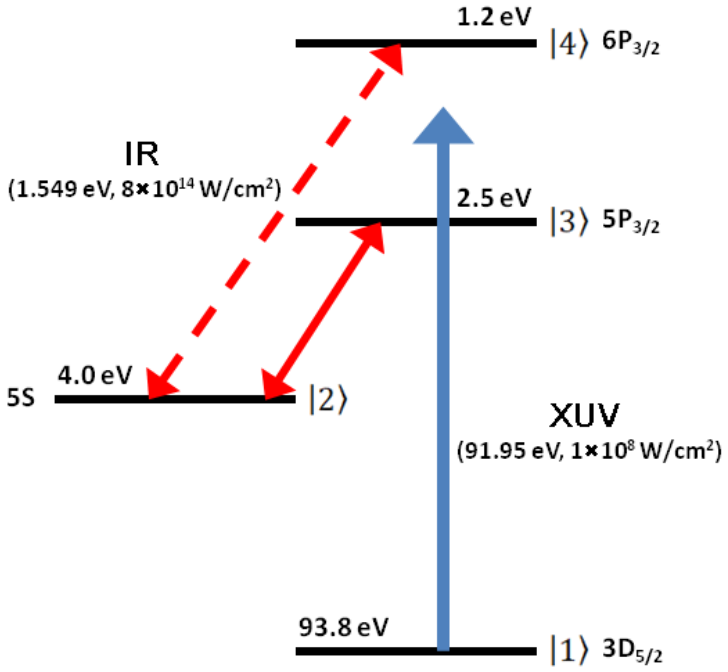

Figure 6.4: Representation of the 4-level system of krypton interacting with the IR and XUV pulses. The levels 1, 2, 3 and 4 represent 3d, 5s, 5p and 6p respectively.

$$\dot{\rho}_{22} = -i\bar{E}[\mu_{23}(\rho_{23} - \rho_{32}) + \mu_{24}(\rho_{24} - \rho_{42})]$$

$$\dot{\rho}_{33} = -i\bar{E}[\mu_{13}(\rho_{13} - \rho_{31}) + \mu_{23}(\rho_{23} - \rho_{32})]$$

$$\dot{\rho}_{44} = -i\bar{E}[\mu_{14}(\rho_{14} - \rho_{41}) + \mu_{24}(\rho_{24} - \rho_{42})]$$

$$\dot{\rho}_{11} = -\dot{\rho}_{22} - \dot{\rho}_{33} - \dot{\rho}_{44}$$

$$\dot{\rho}_{12} = i\omega_{12}\rho_{12} + -i\bar{E}[\mu_{13}\rho_{32} - \mu_{23}\rho_{13} + \mu_{14}\rho_{42} - \mu_{24}\rho_{14}] \qquad (6.7)$$

$$\dot{\rho}_{13} = i\omega_{13}\rho_{13} + -i\bar{E}[\mu_{13}(\rho_{33} - \rho_{11}) + \mu_{14}\rho_{43} - \mu_{23}\rho_{12}]$$

$$\dot{\rho}_{14} = i\omega_{14}\rho_{14} + -i\bar{E}[\mu_{14}(\rho_{44} - \rho_{11}) + \mu_{24}\rho_{12} - \mu_{13}\rho_{34}]$$

$$\dot{\rho}_{23} = i\omega_{23}\rho_{23} + -i\bar{E}[\mu_{23}(\rho_{33} - \rho_{22}) + \mu_{24}\rho_{43} - \mu_{13}\rho_{21}]$$

$$\dot{\rho}_{24} = i\omega_{24}\rho_{24} + -i\bar{E}[\mu_{24}(\rho_{44} - \rho_{22}) + \mu_{23}\rho_{34} - \mu_{14}\rho_{21}]$$

$$\dot{\rho}_{34} = i\omega_{34}\rho_{34} + -i\bar{E}[\mu_{13}\rho_{14} - \mu_{14}\rho_{31} + \mu_{23}\rho_{24} - \mu_{24}\rho_{32}]$$

Where, ρ_{ii} are the populations of levels i, with i = 1, 2, 3, 4 corresponding to levels 3d, 5s, 5p, 6p, respectively, the off-diagonal elements ρ_{ij}, with $\rho_{ij} = \rho_{ij}^*$, represent the coherences

between levels i, j, μ_{ij} are the dipole coupling coefficients of the corresponding transitions and ω_{ij} are their angular frequencies. For the $3p^{-1}5s$ transition, a corresponding three-level system in a cascade configuration 3p-5s-5p was considered. The laser pulses are of Gaussian shape, with the electric field $E = \hbar\bar{E}$ given by

$$E(t) = E_{IR}e^{-2\ln 2(t/\tau_{\mathrm{IR}})^2}\cos(\omega_{\mathrm{IR}}\mathrm{t}) + E_{XUV}e^{-2\ln 2[(t-t_0)/\tau_{\mathrm{XUV}}]^2}\cos[\omega_{\mathrm{XUV}}(\mathrm{t}-\mathrm{t}_0)] \quad (6.8)$$

Where, E_{IR} and E_{XUV} are the peak amplitudes of the IR and XUV pulses, respectively, ω_{IR} and ω_{XUV} are their optical angular frequencies. The duration of the pulses: τ_{IR} and τ_{XUV} are the full width at half maximum (FWHM) of the pulse intensity profiles. t_0 is the delay between the IR and the XUV pulses. The values of the parameters considered in the simulations shown in figure 6.3 are: $\mu_{13} = \mu_{14} = 7\times10^{-32}$ Cm, : $\mu_{23} = \mu_{24} = 2.1\times10^{-29}$ Cm, ω_{12} = 89.8 eV, ω_{23} = 1.5 eV, ω_{34} = 1.3 eV, and ω_{XUV} = 91.95 eV, for the $3d^{-1}5p$ four-level system (upper row in Figure 6.3); and $\mu_{12} = 3.3\times10^{-32}$ Cm, $\mu_{23} = 3.0\times10^{-29}$ Cm, ω_{12} = 210.4 eV, ω_{23} = 1.5 eV, and ω_{23} = 210.4 eV, for the $3p^{-1}5s$ three-level system (lower row in Figure 6.3). ω_{IR} = 1.55 eV τ_{IR} = 25 fs, τ_{XUV} = 200 as, the peak intensity of the XUV pulse is I_{XUV} = 10^8 W/cm^2, and t_0 is considered from -80 fs to 80 fs in steps of 0.2 fs. The atomic polarization response is

$$\widetilde{\mathrm{P}} = 2[\mu_{13}\mathrm{Re}(\rho_{13}) + \mu_{14}\mathrm{Re}(\rho_{14})] \quad (6.9)$$

For the calculation of the time evolution of the atomic polarization, we subtract the contribution from the IR field alone, and we safely use a window function given by a super Gaussian centred at the IR pulse with a width of 40 fs (FWHM) in order to avoid the coherences induced by the XUV pulse and the upper states when the atom is not laser dressed, which in the numerical simulation produces a "ringing" effect until long after the XUV pulse is over [207]. This well-known spurious ringing does not produce stimulated emission or

absorption and is basically absent when the atom is laser dressed. The calculated transmission signal is given by

$$T = \exp\left\{-\frac{4\pi\omega NL}{c}\,\mathrm{Im}\left(\frac{\tilde{P}(\omega)}{\tilde{E}_{XUV}(\omega)}\right)\right\} \qquad (6.10)$$

where $\tilde{P}(\omega)$ and $\tilde{E}_{XUV}(\omega)$ are the spectra of the atomic polarization and the input XUV field, respectively, c is the speed of light in vacuum, N is the atomic density, and L is the length of the interaction region [247]. In the simulations we chose NL = 9×10^{21} m^{-2}, which corresponds to a pressure of 120 mbar at room temperature with a propagation distance of 3 mm.

Calculations were performed in a wide intensity range from I_{IR} = 4×10^{13} W/cm² to 6×10^{14} W/cm² for both the $3d^{-1}5p$ (91.3 eV) and $3p^{-1}5s$ (210.4 eV) transitions and three of them are shown in Figure 6.5, where *T-1* is plotted as a function of delay and photon energy. The unique feature of Kr that the energy distance between the 5s and 5p levels is 1.52 eV indeed assures a strong dressing effect for both the $3d^{-1}5p$ and the $3p^{-1}5s$ transitions. As can be seen from the calculations in Figure 6.5, the absorption lines of $3d^{-1}5p$, $3d^{-1}6p$ [Figures 6.5(a,c,e)] and $3p^{-1}5s$ [Figures 6.5(b,d,f)] split to a structure of absorption between the delays of -20 fs and +20 fs, when the gas is pumped by the dressing laser pulse. It means temporal absorption at other photon energies than the original absorption lines appeared. This structure was broader at higher intensities and there was a spectrally periodic structure with the energy of the pump laser photons. This structure is almost washed out and disappears at very high intensities between -40 and +40 fs. Furthermore, there is a fast oscillation in the absorption following the shape of the square of the electric field of the dressing laser pulse. It can also be seen that the transmission (*T-1*) can exceed 0 meaning the appearance of gain within very short time intervals as was earlier predicted and measured [248]. The calculated dressing effect was about 3-times stronger for the $3d^{-1}5p$ than for the $3p^{-1}5s$ as can be seen from the colour bars in Figure 6.5.

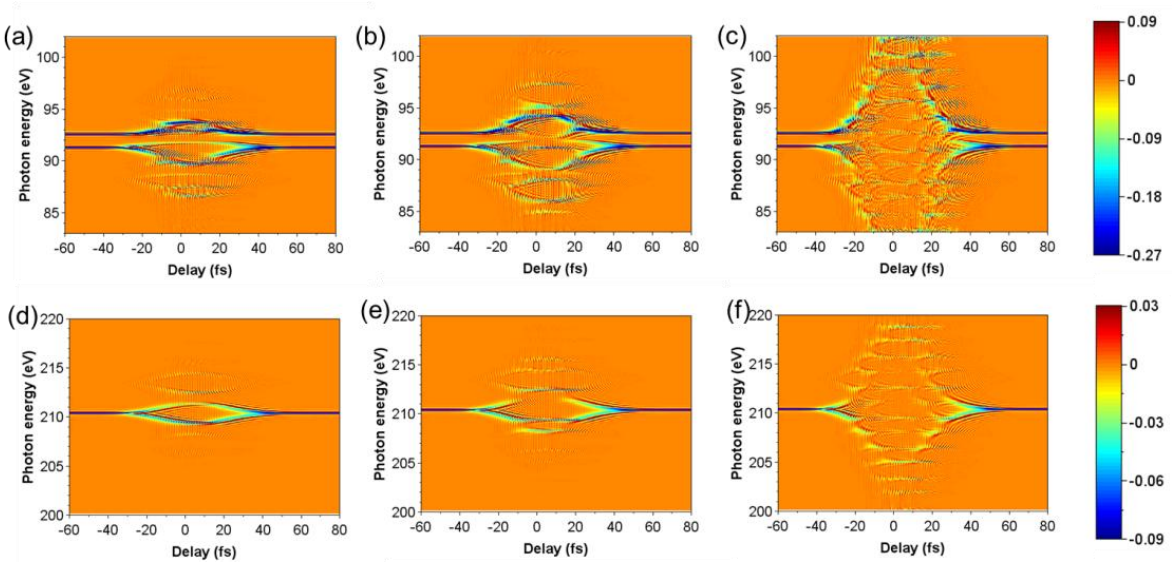

Figure 6.5: Calculated XUV transmission change [*T-1*, see Eq. (6.10)] of the (upper row) $3d^{-1}5p$ and (lower row) $3p^{-1}5s$ dressed transitions at intensities of (a, b) 4×10^{13}, (c, d) 1×10^{14} and (e, f) 6×10^{14} W/cm².

II. Results on the laser dressing of the $3d^{-1}5p$ and $3p^{-1}5s$ transition of krypton atoms

To examine and resolve the dynamics of the laser dressing on the $3d^{-1}5p$ and $3p^{-1}5s$ transitions of Kr atoms, delay scans were performed with femtosecond resolution in a delay interval of 420 fs using delay steps of 1.4 fs, furthermore with attosecond resolution in a delay interval of 50 fs using delay steps of about 170 as, respectively. Within one delay scan, HHG spectra were recorded with 2 s integration time (20 laser shots) in 300 delay steps limited by technical reasons. According to the calculations (Figure 6.5), weak dressing was predicted for a weak driving field below 1×10^{14} W/cm^2, where the ionized fraction of Kr atoms was also small below 10^{-4} according to ionization theories [249] and measurements [250]. In a strong driving field [e.g. at 6×10^{14} W/cm^2, Figures 6.5(c), 6.5(f)], the theory predicted a strong dressing

effect on the transmitted XUV signal with all atomic states merged into a continuum. Although for these laser intensities the ionization was strong and almost all the atoms became ionized during the interaction with the laser pulse, as an earlier study on Xe [233] also showed, the dressing effect remained still observable.

A. Femtosecond dynamics of the transient absorption

Applying a strong field dressing with laser peak intensity of 6×10^{14} W/cm^2, a delay scan was performed with femtosecond (1.4 fs) temporal resolution and plotted in Figures 6.6(a) and 6.6(c) in the spectral ranges around the core transitions of $3p^{-1}5s$ (210.4 eV) and $3d^{-1}5p$ (91.3 eV), respectively. Below the 214.4 eV ($3p_{3/2}$) ionization threshold in Figure 6.6(a), strong distortion of the harmonic line H137 at 211 eV can be observed at around zero delay as the consequence of the dressing laser field, as it would be expected from the calculation in Figure 6.6(f). Going further from the $3p^{-1}5s$ absorption line, calculations predicted decreasing dressing effects, which was well observable on the measurement. While the harmonic line H135 at 208 eV was still strongly affected, H133 was only weakly and H131 was almost not affected. Over the ionization threshold (H139, H141), the effect of dressing was not visible similarly to [233]. In Figure 6.6(b), the measured and calculated transient transmissions were compared at two particular photon energies of 210.4 eV, which belonged to the $3p^{-1}5s$ transition, and of 209.3 eV, where the calculations predicted a strong dressing effect. At the $3p^{-1}5s$ absorption line, the calculated strong increase of the transmission was well followed by the measurement. Similarly, the transient absorption at 209.3 eV was well reproduced by the measurement. The fast modulations observable on the calculations were caused by the dressing laser field and had a period of 1.3 fs, which could not be resolved with the 1.4 fs

temporal steps of these measurement series. They would have produced only confusing noise in the measurement, so a Fourier filter was applied to suppress the faster than 10 fs processes.

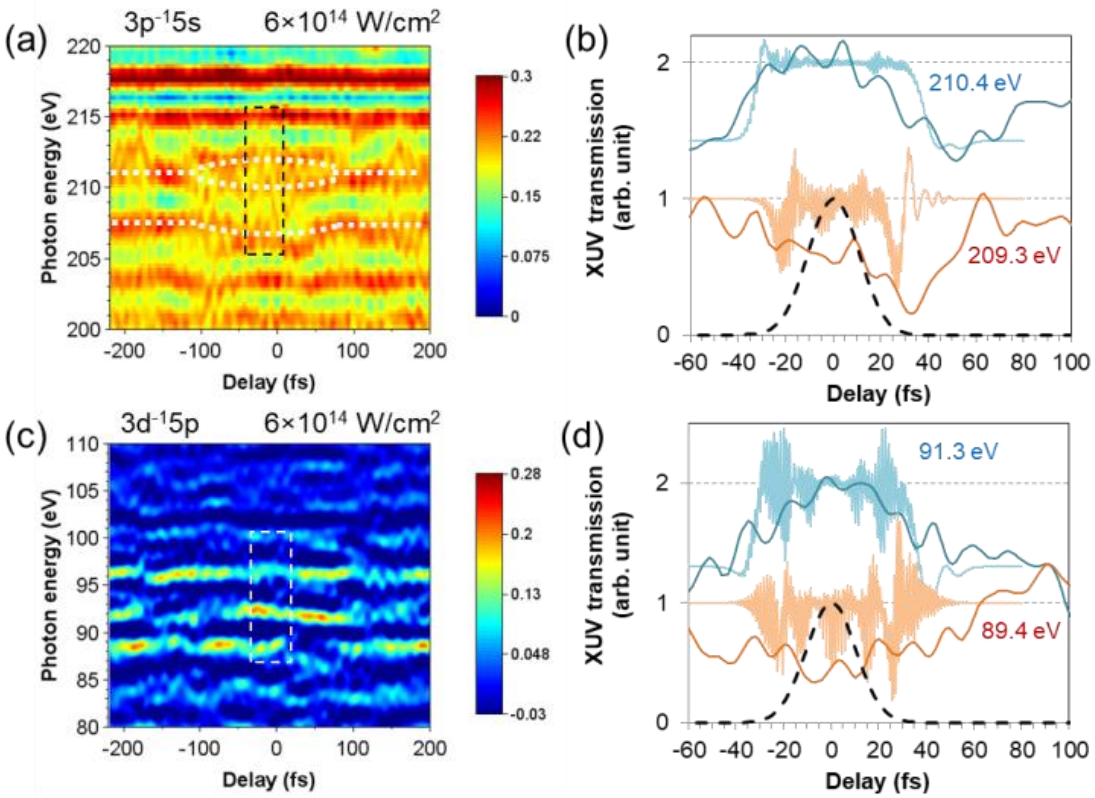

Figure 6.6: Femtosecond dynamics of the dressed Kr was resolved at laser intensity of 6×10^{14} W/cm^2. The measurements showed strong transmission change around zero delay at the core transitions of (a) $3p^{-1}5s$ at 210.4 eV noted with white dashed lines, (c) at $3d^{-1}5p$ and $3d^{-1}6p$ transitions between 91.3 eV and 92.6 eV. The dashed frames show the windows where higher resolution measurements were performed. (b), (d) Comparison of the theoretical calculations (thin lines) with the measurements (thick lines) gave good agreement for both spectral ranges. The curves were shifted vertically for better visibility. Black dashed lines note the shape of the laser pulse used for the calculations. The measured transmission changes are given in arbitrary unit in this and every later figure.

The change in the absorption spectrum at around 92 eV during the illumination with the strong laser field was also measured for the transitions $3d^{-1}5p$ and $3d^{-1}6p$ in Figure 6.6(c). In this spectral range, the shape of the HHG spectra and especially the presence of the harmonic line would dominate and overwhelm the dressing effect. To avoid this, a Fourier filter had to be applied on the measured spectra to filter out the harmonic line structure at the 0.5 harmonic orders and also the spectral shape at zero order. Consequently, this figure shows only the change of the XUV transmission. Such filtering for Figure 6.6(a) was not necessary, because there were no big changes in the spectral shape and the harmonic-line-structure was also weak in that spectral range. In Figure 6.6(c), an essential transmission change can be observed at three photon energies, at around 89 eV, 92 eV and 96 eV. At about 92 eV, the transmission increased at around zero delay, which can be attributed to the disappearance of the absorption of the transitions $3d^{-1}5p$ and $3d^{-1}6p$, similarly to the $3p^{-1}5s$ absorption line. This increased transmission was also predicted by simulations at 91.3 eV plotted in Figure 6.5(c). The fast modulations observable on the calculations were caused by the dressing laser field, which could not be resolved in the measurements with such large delay steps. The observed signal at about 89 eV had a strong transmission at negative delays and transient absorption within a time interval at and after zero delays. It can be attributed to a dressed state and also to an additional process of transient two-photon (XUV+NIR) excitation of the $3d^{-1}5s$ transition. Comparing to the calculation in Figure 6.6(d), the measurement showed a similar change of transmission but a somewhat broader delay range, what can be the consequence of the used super-Gaussian temporal window in the calculation making the calculations more efficient in the attosecond time scale but less accurate in the sub-ps time scale. The observed signal at 96 eV, which appeared at the ionization threshold, was probably caused by the laser field enhanced ionization, which process was not part of the present study and was not considered in the theory. Both in figures 6.6(a) and 6.6(c), weaker distortions of the transmitted signal

were observed at around ±190 fs delays, which were probably the consequence of a weaker pre and post pulses in the laser pulse, unrecognized during pulse characterization.

B. Fourier-transform spectroscopy to recognize attosecond transient processes

Transient changes of two core-level transitions were studied, namely, the transition from $3d_{5/2}$ to $5p_{3/2}$ at around 90 eV and the transition from $3p_{3/2}$ to $5s_{1/2}$ at around 210 eV. Looking into the results of the measurements and calculations in more detail, however, one can recognize different contributions. To do so, measurement series in the time window noted in Figure 6.6(a) and 6.6(c) were performed with attosecond resolution and the 2D data sets (spectrum versus delay) of both the measurements [Figures 6.9(a), 6.9(c), 6.10(b), 6.10(d)] and calculations (Figure 6.5) were Fourier transformed and compared in Figure 6.7. In the first row of Figs. 6.7(a) and 6.7(b) show the result of the theory and the second row the results of the corresponding measurements.

A similar change of the transient absorption can be expected in gases as was observed in earlier measurements for solids [224] and was described as follows

$$\Delta T \propto I_0(\tau)\cos^2(2\pi\nu_0\tau)\cos^4(2\pi\nu_B\tau), \qquad (6.11)$$

Where, τ is the delay between the pump and probe pulses; $I_0(\tau)$ is the envelope of the laser pulse; ν_0 is the laser frequency and $\nu_B = \Delta E/2h$ is the beat frequency determined by the energy difference of the sublevels of certain electron shell of the atom. This equation can be rewritten into a more intuitive form

$$\Delta T \propto I_0(\tau)[1+\cos(4\pi\nu_0\tau)][3+4\cos(4\pi\nu_B\tau)+\cos(8\pi\nu_B\tau)], \qquad (6.12)$$

It predicts laser dressing at $2\nu_0$ = 0.75 PHz, beating at frequencies $2\nu_B$ and $4\nu_B$, furthermore few smaller mixed terms. One can recognize from the calculations in Figure 6.7 that the density matrix equations [Eqs. (6.7)] describe the dressing as a strongly nonlinear process and

beyond the expected dressing frequency of 0.75 PHz, its second and even third harmonics appear at $4\nu_0$ = 1.5 PHz and $6\nu_0$ = 2.25 PHz. The linear description [Eq. (6.12)] however, did not predict the appearance of $4\nu_0$ and $6\nu_0$ harmonics of the laser dressing. In comparison to the 1D Fourier spectra of the measurements [Figure 6.7(c) and 6.7(d)], the peaks at 0.75 PHz and 1.5 PHz clearly appeared and were noted with black arrows. Mainly in Figure 6.7(d), the measured dressing peaks were double peaks of 0.65/0.75 PHz and their harmonics of 1.3/1.5 PHz. The third harmonic peaks at 1.95/2.25 PHz can even be recognized but were near the level of the background noise. The origin of the double-peek structure has not still been resolved.

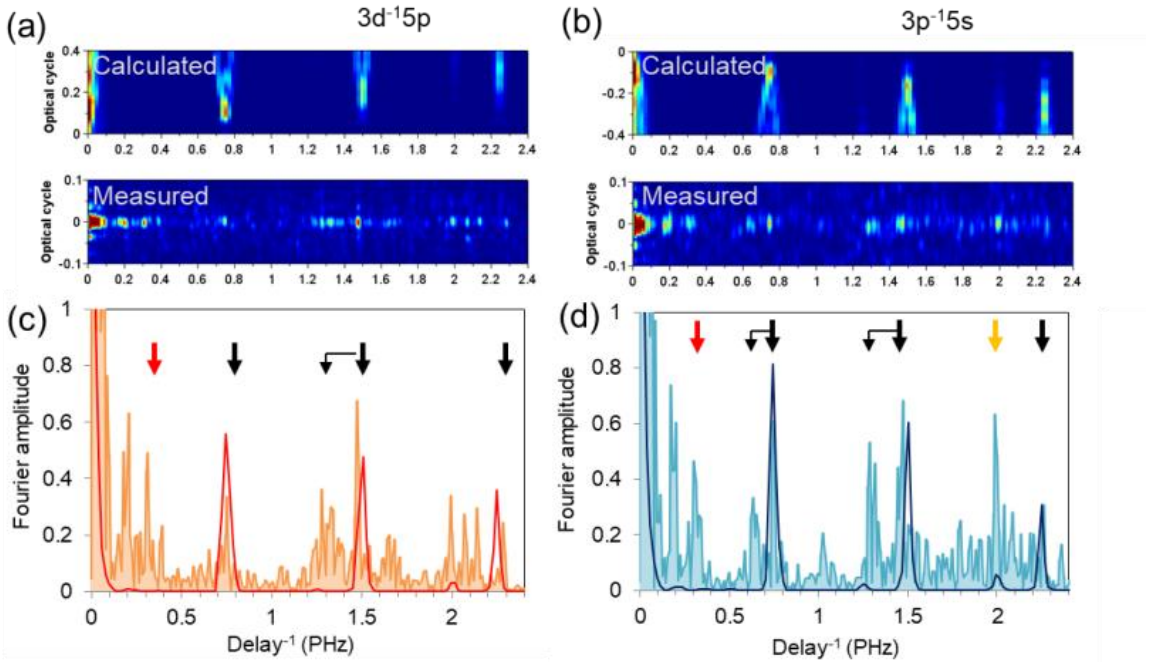

Figure 6.7: (a), (b) The 2D Fourier transformed spectra of the modelled and the measured 2D spectra-delay data sets, for the (a), (c) $3d^{-1}5p$ and (b), (d) $3p^{-1}5s$ transitions, show the peaks of the laser (black arrows) dressing and (yellow arrows) the beating. (c), (d) Averaged Fourier spectra of the (orange/light-blue) measurement and (red/blue) calculation. Possible transitions are noted with arrows where beating can be observed from 3d and 3p levels, respectively.

Additional strong spectral components can be observed at 2 PHz in Figure 6.7(d) noted with yellow arrow and at 0.3 PHz in both Figure 6.7(c) and 6.7(d) noted with red arrows. These two peaks were the beating between two absorption channels starting from the sublevels of the 3d and 3p quantum states of Kr and the possible beating schemes were presented in Figure 6.2(e) for the two quantum states. These beating are examined in details in Section 6.2.3.

In addition, well distinguishable peaks can be observed at about 0.2 PHz, which appeared in both cases. The origin of these peaks has not yet been resolved; it could be the consequence of the coupling between 5s, 5p, 6p and one higher atomic level, which were not included in the DM model.

C. Attosecond dynamics of the transient absorption in case of strong ionization

To study the transient processes in more detail, a part of the delay range in Figures 6.6(a) and 6.6(c) was scanned with a higher temporal resolution of 170 as temporal steps and was plotted in Figures 6.8(a) and 6.8(b) and compared with the calculations of Figure 6.8(c) and 6.8(d). Here, the aim was to study laser dressing, thus Fourier windows at the 0.75 PHz dressing peak and at the zero-order were applied. Beyond the temporal and spectral patterns recognized earlier, the fast change in the transmission caused by the electric field of the dressing laser pulse appeared in both spectral ranges. The calculations showed much richer temporal and spectral structures that were not possible to resolve with the measurements; however the main structural properties were well resolved in both cases. It was worth laying emphasis on the phase shift along the vertical line structures caused by the electric field of the dressing laser pulse, which consequently have a temporal period of 1.3 fs. In Figure 6.8(a), a phase shift of about one quarter period (0.7 fs) can be observed between the two measured periodic structures, just above and below the absorption line at 91.3 eV, which can also be seen in the

calculation. A similar shift can be observed at the absorption line of 210.4 eV in Figure 6.8(b). At the two photon energies below and above the two absorption lines, the transmission changes were plotted in Figures 6.8(e) and 6.8(f). Both the slow changes and the fast periodic modulations show very good agreement between the measured and the calculated results (dark and light blue solid lines), and additionally, the phase shift between the curves plotted at different photon energies (red dashed lines) are clearly visible.

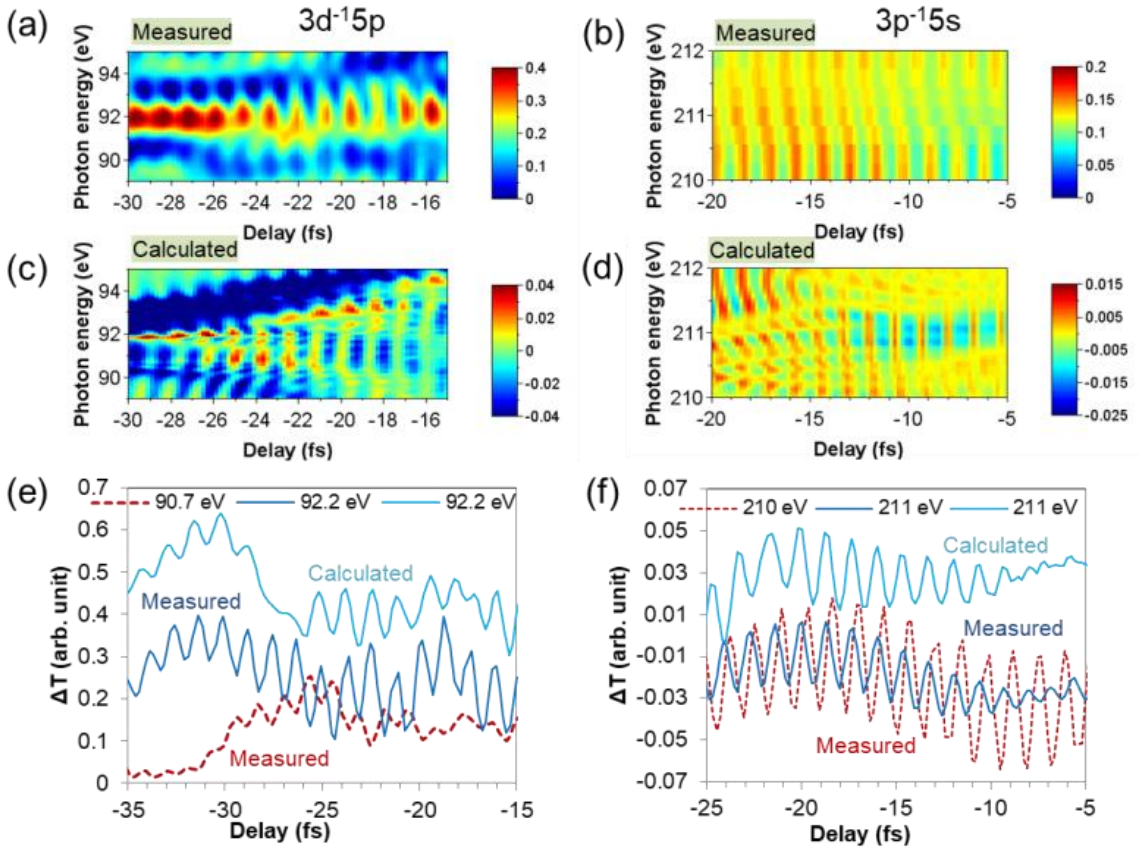

Figure 6.8: Attosecond dynamics of the dressed Kr was resolved at laser intensity of 6×10^{14} W/cm^2. The measurements and calculations of (a), (c) $3d^{-1}5p$ and (b), (d) $3p^{-1}5s$ dressed transitions showed the fast transmission change caused by the electric field of the dressing laser pulse beyond the slow change. (e), (f) At certain photon energies, the comparison of the measurements and the calculations shows very good agreements.

D. Attosecond dynamics of the transient absorption in case of weak ionization

As seen in Figures 6.5(c) and 6.5(f), when dressing the Kr atoms with a strong laser field of 6×10^{14} W/cm^2 the original absorption line of the atoms disappeared completely, and only weak and strongly structured absorption appeared during the time the atoms were illuminated with the laser pulse. Additionally, this induced absorption was extended over a wide spectral range. Much less extended and more prominent absorption changes were predicted by the theory at lower laser intensities as shown in Figures 6.5(a), 6.5(b), 6.5(d) and 6.5(e). To study this case, measurements were performed at two lower dressing intensities of 4×10^{13} W/cm^2 and 8×10^{13} W/cm^2. At the former intensity, it was observed that there was no visible ionization of the Kr gas, while at the later one, a weak ionization was visible.

To look into the measurements in detail, temporal and spectral windows of interest have been plotted in Figures 6.9(a) and 6.9(c), namely at around 92.4 eV at higher intensity, and at around 210.4 eV at lower intensity. The involved transitions are noted with red dashed arrows in Figures 6.9(a) and 6.9(c). As it can be recognized for both transitions, the phase of dressing (0.75 PHz) transmission modulation shifted at around the absorption lines. Plotting the transmission change separately at nearby photon energy (orange dashed) together with the transmission at the absorption lines (blue) in Figures 6.9(b) and 6.9(d), the phase shift can be well recognized. An interesting phenomenon can be observed in both transitions, namely that the sign of the phase shift changed at about -12 fs and -18 fs delays respectively. The phase shift of the transmission was resolved in the experimental measurements with accuracy between 300 as and 650 as.

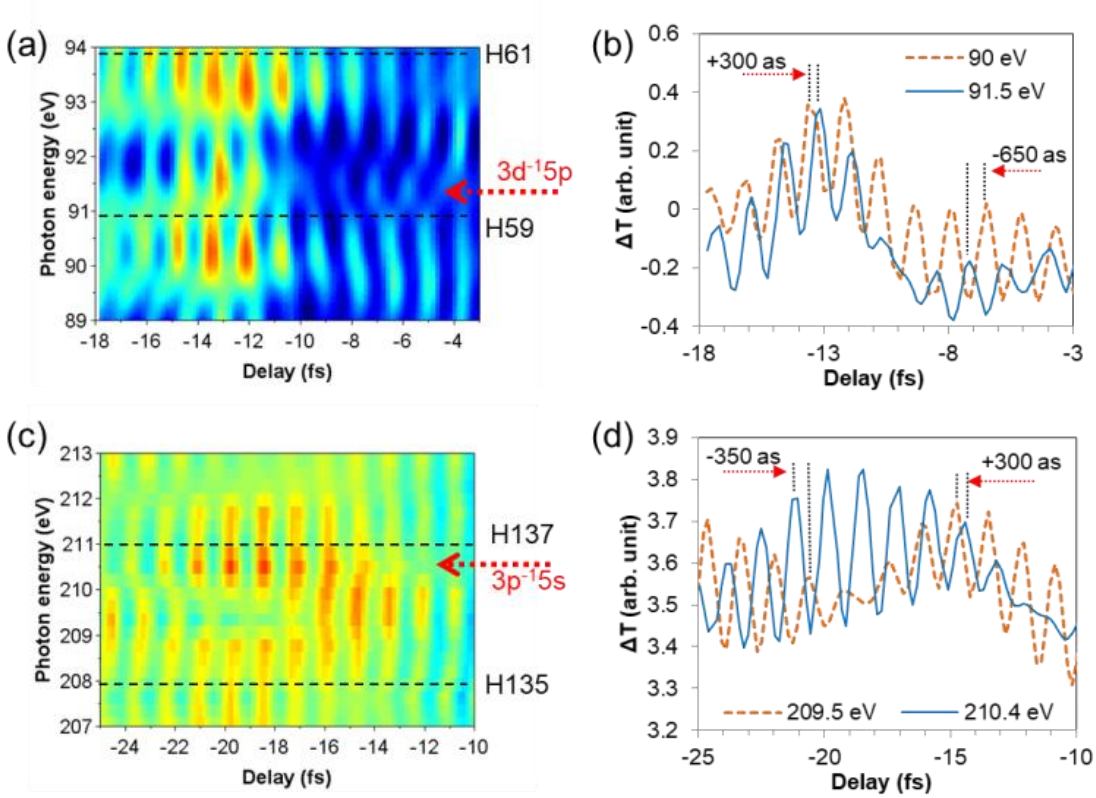

Figure 6.9: Attosecond dynamics of the dressed Kr was resolved at laser intensity of (a) 8×10^{13} W/cm^2 at $3d^{-1}5p$ and (c) 4×10^{13} W/cm^2 at $3p^{-1}5s$ transitions. In panels (b) and (d), the delay dependence of the transmission changes were compared at two nearby photon energies.

For further comparison, a larger delay range was also measured and the measurement results were plotted in Figures 6.10(b) and 6.10(d) for both transitions of $3d^{-1}5p$ and $3p^{-1}5s$ as noted in the figure. In these measurements, the Si foil was not used as earlier in Figure 6.6, so that the effects of the dressing over 100 eV became also visible. Furthermore, the zero order was not filtered out as it was done in the strong field measurement in Figure 6.6. Here another method was used to eliminate the shape of the spectrum and harmonic lines, mainly by subtracting the DC part of the delay-dependent signal at every photon-energy and plotting only the AC part.

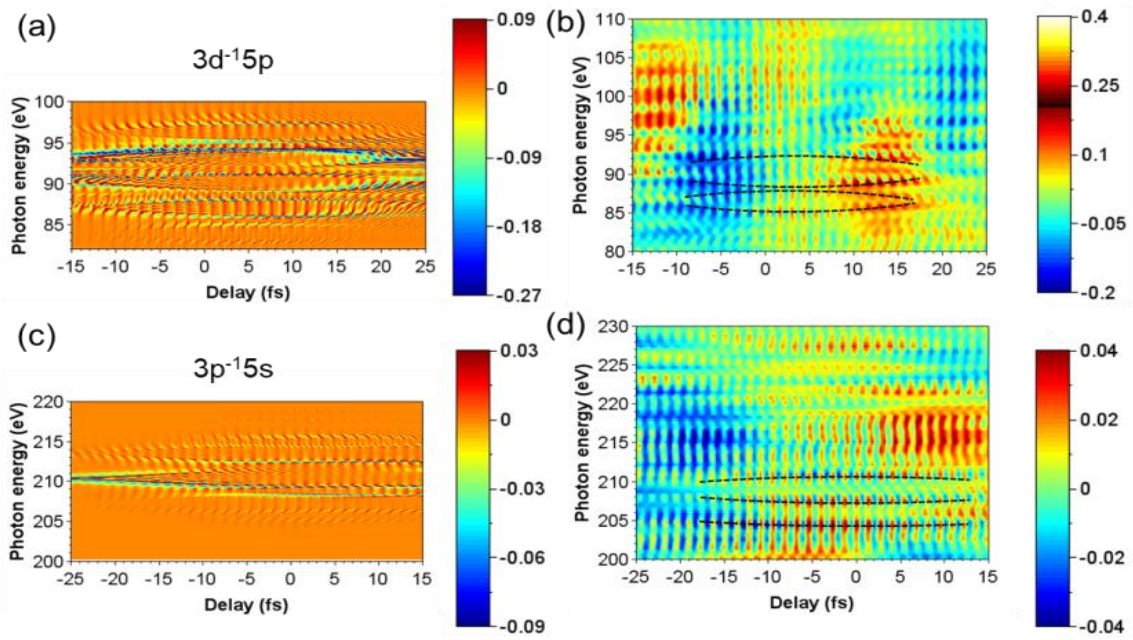

Figure 6.10: Attosecond dynamics of the dressed Kr was resolved at laser intensity of 8×10^{13} W/cm^2. The measurements of (a), (b) $3d^{-1}5p$ and (c), (d) $3p^{-1}5s$ dressed transitions showed the dense periodic change of the transmission caused by the electric field of the dressing laser pulse. The split of the absorption lines and the appearance of the dressed states are highlighted with black dashed lines.

In the left column of Figure 6.10, the magnified part of the calculations was plotted in the same delay ranges as the measurements. It can be recognized on the calculated figures that the original absorption lines were split and opened to ±1 and ±2 order dressed lines. Additionally, a fast periodic structure was around the dressed lines everywhere with a period of half optical cycle of the dressing laser field (1.34 fs or 0.75 PHz). The split of the absorption lines can be recognized in the measurement too (right column). Furthermore, the higher order (mainly negative order) dressed states caused additional absorptions and spectrally periodic patterns

with about 1.5 eV periods. The split of the absorption lines and the new dressed states were highlighted with gray dashed lines in the measured (b) and (d) panels.

For direct comparison, the delay dependence of the XUV transmission was separately plotted in Figure 6.11 at few photon energies around the absorption lines. The calculated curves at four dressing laser intensities were plotted with plastic colours and shifted with integers for better visibility. At the two measured intensities, the results (within the narrower delay range of the measurements) were plotted with similar but darker colours and also shifted with half-integers for better visibility.

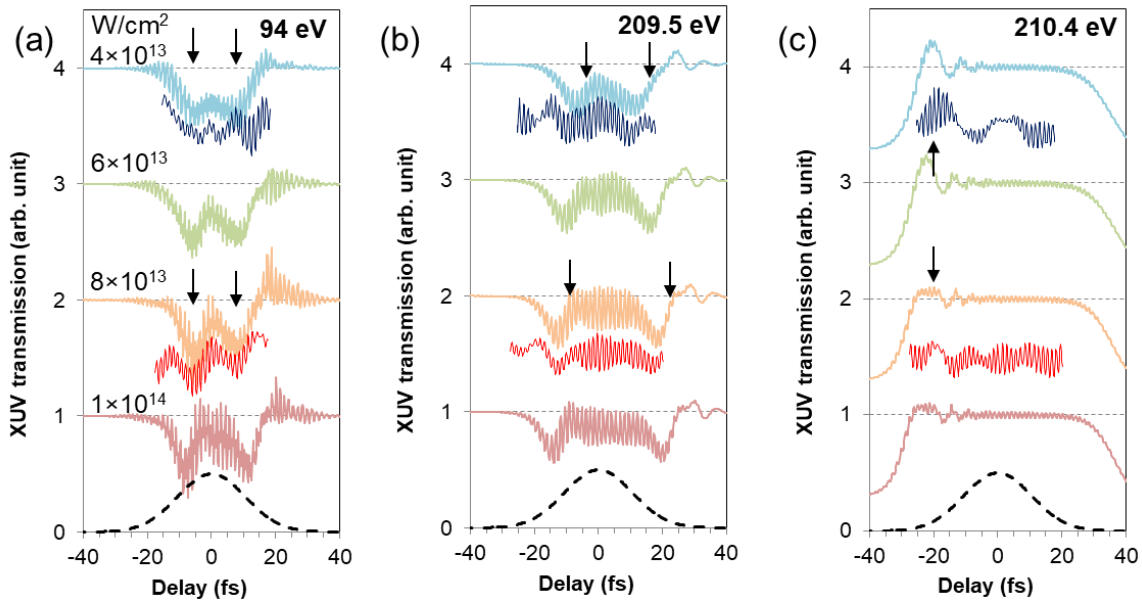

Figure 6.11: Attosecond dynamics of the dressed Kr is plotted (light colours) at four laser intensities of the calculation and (dark colours) two intensities of the measurement at few photon energies. For better visibility, the curves were shifted vertically with integers in the case of the calculations and with half-integers in the case of the measurements.

The measured transmission curves followed the theoretical predictions with good accuracy: At 94 eV and 209.5 eV, the dressing laser induced absorption with two characteristic valleys (noted with back arrows) being more prominent at higher intensities and their positions were dependent on the laser intensity. On the measurements, both the laser induced absorption and the presence of the valleys and the mentioned characteristics were observed at the correct delays. Additionally, around zero delay, the theory predicted increasing amplitude of the modulation of 0.75 PHz dressing on increasing intensity, what was also observed. At 210.4 eV, the original absorptions of the Kr atoms were cancelled by the laser pulse and even transient gain (larger than 1 transmission) appeared at the characteristic peaks at around -20 fs delay at intensity of 4×10^{13} W/cm^2, what range was anyway measured and plotted in Figure 6.9(c). This peak that was well visible at low intensities, almost disappeared at higher intensities both in the theory and the experiments, see Figure 6.11(c). Similar transient gains were theoretically predicted at 94 eV and at about +20 fs delay at larger laser intensities of 8×10^{13} W/cm^2 and 1×10^{14} W/cm^2 in Figure 6.11(a). Transient gain was also theoretically predicted and experimentally observed in Figure 6.8(a) – 6.8(d), where the calculated positive transmission change (red colours) meant larger than 1 transmission or gain.

6.2.5 Conclusion

By using attosecond pulse trains of HHG and the broad generated spectrum covering the 70 – 230 eV photon energy range, laser dressed krypton atoms was studied by attosecond transient absorption spectroscopy at the two core level transitions $3d^{-1}5p$ and $3p^{-1}5s$, at 91.3 eV and 210.4 eV, respectively. The energy difference of the 5s and 5p levels of Kr (1.52 eV) gave a unique opportunity for resonantly dressing these levels with the laser pulses of a Ti:sapphire laser system. Therefore, making it possible to observe strong dressing effects not only at high

laser intensities such as 6×10^{14} W/cm^2, but even at about 10 times lower laser intensities of 4×10^{13} W/cm^2 and 8×10^{13} W/cm^2 too. In the meantime, the dressing processes were modelled with three- and four-level density matrix equations beyond the rotating-wave approximation and compared the experimental and theoretical results. The theory predicted a complex temporal behaviour of the transmission change containing delay ranges with transient absorption and with transient gain also in the femtosecond time scale and fast laser field driven temporal oscillations at its second, fourth and sixth harmonic frequencies of 0.75, 1.5 and 2.25 THz. Experimentally, the second and fourth harmonics were observed. Furthermore, quantum beats at 0.3 PHz and 2.0 PHz were observed, which were attributed to the beating between the $3d_{5/2}$ and $3d_{3/2}$ sub-levels and the $3p_{3/2}$ and $3p_{1/2}$ sublevels, respectively.

Summary

The thesis deals with the control of atomic and molecular quantum systems dynamics as they interact with ultrashort laser pulses in the femtosecond and attosecond regime. The density matrix (DM) formalism was introduced to model and simulate the interaction process and describe the dynamics of these systems on their fundamental timescales. It gives a physical insight into coherent control and quantum control spectroscopy as they steer population distribution of atoms and molecules from an initial state to a target state with numerous potential applications.

A first study using the DM analysis was shown in chapter 3 by simulating population transfer in atomic sodium as it interacts with a trichromatic π-pulse. Complete population inversion was successfully demonstrated and controlled using optimal parameters. The influences of critical parameters like pulse area combination, field detuning and pulse chirp were shown. A set of areas $\sqrt{3}\pi$, 2π and $\sqrt{3}\pi$ was found to be the optimal area combination for achieving complete population inversion for a four-level system.

In chapter 4, the study was extended to the excitation of unoccupied Rydberg state of hydrogen-like Alkali atoms using the trichromatic π-pulse scheme. Excitation of low-lying Rydberg states in Rubidium was successfully achieved theoretically for application in the design of robust fast quantum gates, which plays a key role in effective implementation of quantum computation. A balance between the dipole moment and pulse duration is carefully studied to achieve almost complete population inversion. This was demonstrated also by comparing results obtained using single and multiphoton π-pulse schemes. The work shown in Chapters 3 and 4 were carried out beyond the RWA since intense ultrashort pulses inducing large ac-Stark shifts were involved. In cases of complex molecular systems, where low

intensity fields are involved, the RWA and slowly varying envelope approximation were implemented.

Control of population inversion and vibrational coherences was shown in Chapter 5. Parameters for a typical Oxazine system were selected to perform the simulations. An extensive study of the enhancement of population inversion and vibrational coherences was carried out by comparing results of TL pulses and shaped excitation pulses. The DM formalism was finally extended to describe control of dynamical processes on the attosecond timescale. In Chapter 6, the laser dressing processes in krypton atoms interacting with attosecond pulse trains were modelled using the DM equations beyond the RWA. The theoretical results were compared with attosecond transient absorption experiments performed in Vienna with good agreements showing the applicability of the DM formalism in this relatively new area of Physics.

An advantage of the DM formalism used without the RWA is the possibility of its implementation on different timescales and laser pulse intensities, which can account for numerous fundamental processes. The work performed in this thesis suggests several possible extensions of the DM formalism for studying other systems and geometric configurations like nano-systems, solid-state systems and also to describe other dynamic processes and configurations in atoms and molecules.

Bibliography

1. Holzwarth, A. Applications of ultrafast laser spectroscopy for the study of biological systems, Quarterly Reviews of Biophysics, 22(3): 239 – 326 (1989).

2. Diels, J.C.; Rudolph, W. *Ultrashort Laser Pulse Phenomena*, 2nd ed.; Academic Press: San Diego, CA, USA (2006).

3. Levine, R.D.; Jortner, J. Mode Selective Chemistry. In Proceedings of the 24th Jerusalem Symp. On Quantum Chemistry and Biochemistry, Jerusalem, Israel, 20–23 May 1991; pp. 535–571 (1991).

4. Liu, Q.; Zewail, A. Femtosecond Real-Time Probing of Reactions. 10. Reaction Times and Model Potentials, Journal of Physical Chemistry, 97, pp. 2209-2220 (1993).

5. Malý, P. Ultrafast laser spectroscopy of semiconductor nanocrystals, Czechoslovak Journal of Physics, 52(5): 645 – 667 (2002).

6. Arimondo, E. *Progress in Optics* (Amsterdam: Elsevier) 35, 257 (1996).

7. Arimondo, E.; Orriols, G. "Nonabsorbing atomic coherences by coherent two-photon transitions in a three-level optical pumping.", Lett. Nuovo Cimento 17, 333 (1976).

8. Gray, H. R.; Whitley, R. M.; Stroud, C. R. Coherent trapping of atomic populations, Opt. Lett. 3, 218 (1978).

9. Harris, S. Electromagnetically Induced Transparency, Phys. Today 50, 36 (1997).

10. Whitley, R.M.; Stroud, C.R. Double optical resonance, Phys. Rev. A 14, 1498 (1976).

11. Vitanov, N.V.; Rangelov, A.A.; Shore, B.W.; Bergmann, K. Stimulated Raman adiabatic passage in physics, chemistry, and beyond, Rev. Mod. Phys. 89, 015006 (2017).

12. Scully, M.O.; Zubairy, M.S. Quantum Optics, Cambridge University Press, Cambridge (2006).

13. Carroll, C.E.; Hioe F.T., Driven three-state model and its analytic solutions. Journal of Mathematical Physics, 29, 487 (1988).

14. Chelkowski, S.; Bandrauk, A.D. Coherent propagation of intense ultrashort laser pulses in a molecular multilevel medium. Journal of Chemical Physics, 89, 3618 (1988).

15. Biegert, J.; Diels, J.C.; Milonni, P.W. Bichromatic two-photon coherent excitation of sodium to provide a dual-wavelength guidestar, Optics Letters, 25(10): 683-685 (2000).

16. Li, Y.; Xiao, M. Transient properties of an electromagnetically induced transparency in three-level atoms Phys. Rev. A 51, R2703 (1995).

17. Boller, K.J.; Imamoglu, A.; Harris, S. Observation of electromagnetically induced transparency, Phys. Rev. Lett., 66, 2593 (1991).

18. Kuklinski, J.R.; Gaubatz, U.; Hioe, F.T.; Bergmann, K. Adiabatic population transfer in a three-level system driven by delayed laser pulses, Phys. Rev. A 40, 6741 (1989).

19. Gaubatz, U.; Rudecki, P.; Schiemann, S.; Bergmann, K. Population transfer between molecular vibrational levels by stimulated Raman scattering with partially overlapping laser fields. A new concept and experimental results, J. Chem. Phys. 92, 5363 (1990).

20. Fleischbauer, M.; Imamoglu, A.; Marangos, J.P. Electromagnetically induced transparency: Optics in coherent media, Rev. Mod. Phys. 77, 633 (2005).

21. Band, Y.B. Julienne, P.S. Population transfer by multiple stimulated Raman scattering, J. Chem. Phys. 95, 5681 (1991).

22. Lukin, M.D.; Imamoglu, A. Controlling photons using electromagnetically induced transparency, Nature 413, 273 (2001).

23. Zhang, G.P.; George, T. Proposed coherent trapping of a population of Electrons in a C 60 molecule induced by laser excitation, Phys. Rev. Lett. 109, 257401 (2012).

24. Zhang, G.P.; George, T. Laser-induced coherent population trapping in C 60, Phys. Rev. A 88, 063808 (2013).

25. Zhang, G.P. Hidden identity in a generic Λ system: applications to coherent population trapping" J. Phys. B: At. Mol. Opt. Phys. 46, 035504 (2013).

26. Yan, M.; Rickey, E.G.; Zhu, Y. Electromagnetically induced transparency in cold rubidium atoms, J. Opt. Soc. Am. B 18, 1057 (2001).

27. Das, B.C.; Bhattacharyya, D.; Das, A.; Chakrabarti, S.; De, S. Spontaneous observations of electromagnetically induced transparency (EIT) and absorption (EIA) in a multi-level V-type system of ^{87}Rb and theoretical simulation of the observed spectra using a multi-mode approach, J. Chem. Phys. 145, 224312 (2016).

28. Kou, J.; Wan, G.; Kang, Z.H.; Wang, H.H.; Jiang, L.; Zhang, X.J.; Jiang, Y.; Gao, J.Y. EIT-assisted large cross Kerr nonlinearity in a four-level inverted-Y atomic system, J. Opt. Soc. Am. B 27, 2035 (2010).

29. Yang, X.; Li, S.; Zhang, C.; Wang, H. Enhanced cross Kerr nonlinearity via electromagnetically induced transparency in a four-level tripod atomic system, J. Opt. Soc. Am. B 26, 1423 (2009).

30. Brumer, P.; Shapiro, M. *Coherent Control of Molecular Dynamics*; Springer: Heidelberg, Germany, pp. 191–213 (1999).

31. Chen, C.; Yin, Y.Y.; Elliott, D.S. Interference between optical transitions, Phys. Rev. Lett. **64** (5), 507 (1990).

32. Chen, C.; Elliott, D.S. Measurements of optical phase variations using interfering multiphoton ionization processes, Phys. Rev. Lett. **65** (14), 1737 (1990).

33. Zhu, L.; Suto, K.; Fiss, J.A.; Wada, R.; Seideman, T.; Gordon, R.J. Effect of Resonances on coherent control of the photoionization and photodissociation of HI and DI, Phys Rev. Lett. 79, 4108 (1997).

34. Dupont, E; Corkum, P.B., Liu, H.C.; Buchanan, M., Wasilewski, Z.R. Phse-controlled currents in semiconductors, Phys Rev. Lett. 74, 3596 (1995).

35. Serrat, C. Coherent control of ultrafast optical four-wave mixing with two-color ω-3ω laser pulses, Phys Rev. Lett. 72, 023808 (2005).

36. Tannor, D.J.; Kosloff, R.; Rice, S.A., Coherent pulse sequence induced control of selectivity of reactions: Exact quantum mechanical calculations. Journal of Chemical Physics, 85, 5805 (1986).

37. Lozovoy, V.V.; Antipin, S.A.; Gostev, F.E., Titov, A.A.; Tovbin, D.G.; Sarkisov, O.M.; Vetchinkin, A.S.; Umanskii, S.Y., Experimental demonstration of coherent control of the molecular iodine vibrational dynamics by chirped femtosecond light pulses, Chem. Phys. Lett., 284 (3-4); 221 – 229 (1998).

38. Baumert, T.;Engel, V.; Röttgermann, C., Strunz, W.T., Gerber, G. Femtosecond pump-probe study of the spreading and recurrence of vibrational wavepacket in Na_2, Chem Phys Lett., 191(6): 639 – 644 (1992).

39. Baumert, T.; Grosser, M.; Thalweiser, R.; Gerber, G. Femtosecond time-resolved molecular multiphoton ionization: The Na_2 system, *Phys. Rev. Lett., 67* (1991).

40. Brif, C.; Chakrabarti, R.; Rabitz, H. Control of quantum phenomena: past, present and future, New Journal of Physics, 12, 075008 (2010).

41. Yang, X.; Zhang, Z., Yan, X., Li, C. Enhanced selectivity and efficiency of coherent population transfer via train of pulse pairs, Phys. Rev. A, 82, 033831 (2010).

42. Bucksbaum, P.H. Attophysics: Ultrafast control, Nature, 421, 593 – 594 (2003).

43. Zewail, A.H. Femtochemistry. Past, present and future, Pure and Appl. Chem., 72(12): 2219 – 2231 (2000).

44. Safronova, M.S.; Williams, C.J.; Clark, C.W. Optimizing the fast Rydberg quantum gate, Phys Rev. A, 67, 040303R (2003).

45. M. Saffman and T. G. Walker, Quantum information with Rydberg atoms, Rev. Mod. Phys. 82, 2313 (2010).

46. Stockman, M.I.; Faleev, S.V.; Bergman, D.J. Coherent Control of Femtosecond Energy Localization in Nanosystems Phys. Rev. Lett., 88(6): 067402-1 (2002).

47. Lozovoy, V.V.; Sarkisov, O.M.; Vetchinkin, A.S.; Umanskii, S.Y., Coherent control of the molecular iodine vibrational dynamics by chirped femtosecond light pulses: theoretical simulation of the pump-probe experiment, Chem. Phys., 243 (1-2); 97 – 114 (1999).

48. Corrales, M.E.; Gonzalez-Vazquez, J.; Balerdi, G.; Sola, I.R.; de Nalda, R.; Bañares, L. Control of ultrafast molecular photodissociation by laser-field-induced potentials, Nature Chemistry, 6, 785 – 790 (2014)

49. Florean, A.C.; Cardoza, D.; White, J.L.; Lanyi, J.K.; Sension, R.J.; Bucksbaum, P.H. Control of retinal isomerization in bacteriorhodopsin in the high-intensity regime. *Proc. Natl. Acad. Sci. USA*, *106*, 10896–10900 (2009).

50. Hildner, R.; Brinks, D.; Van Hulst, N.F. Femtosecond coherence and quantum control of single molecules at room temperature *Nat. Phys.*, *7*, 172–177 (2011).

51. Hildner, R.; Brinks, D.; Nieder, J.B.; Cogdell, R.J.; Van Hulst, N.F. Quantum coherent energy transfer over varying pathways in single light-harvesting complexes. Science, 340, 1448-1451 (2013).

52. Glaser, S.J; Boscain, U.; Calarco, T.; Koch, C.P., *et al*. Training Schrödinger's cat: quantum optimal control, European Physical Journal D, 69: 279 (2015).

53. Bariani, F.; Dudin, Y.O. ; Kennedy, T.A.B.; Kuzmich, A. Dephasing of Multiparticle Rydberg Excitations for Fast Entanglement Generation, Phys. Rev. Lett., 108, 030501 (2012).

54. Jaksch, D.; Cirac, J.I.; Zoller, P.; Rolston, S.L.; Côte, R.; Lukin, M.D. Fast Quantum Gates for Neutral Atoms, Phys. Rev. Lett. 85, 2208 (2000).

55. Xiang Z-L, Ashhab, S. You, J.Q., Nori, F. Hybrid quantum circuits: superconducting circuits interacting with other quantum systems, Rev. Mod. Phys. 85, 623 (2013).

56. Hutson, J.M.; Soldan, P. Molecule formation in ultracold atomic gases, Int. Pev. Phys. Chem. 25, 497-526 (2006). Available in 2010.

57. Corkum, P.B.; Krausz, F. Attosecond science. Nature Physics, 3, 381 – 387 (2007).

58. Miao, J.; Sandberg, R.L.; Song, C. Coherent x-ray diffraction imaging. IEEE J. Selected Topics in Quant. Electronics, 18(1): 399 – 410 (2011).

59. Seres, J.; Seres, E.; Hochhaus, D.; Ecker, B.; Zimmer, D.; Bagnoud, V.; Kuehl, T.; Spielmann, C. Laser-driven amplification of soft X-rays by parametric stimulated emission in neutral gases, Nature Phys. **6**, 455-461 (2010).

60. Serrat, C. Broadband spectral amplitude control in high-order harmonic generation, Appl. Sci., 2(4): 816 – 830 (2012).

61. Serrat, C. Broadband spectral-phase control in high-order harmonic generation, Phys. Rev. A, 87, 013825 (2013).

62. Ranitovic, P.; Hogle, C.W.; Riviere, P.; Palacios, A. *et al*. Attoseconf vacuum UV coherent control of molecular dynamics, 111(3); 912 – 917 (2014).

63. Stockman, M.I.; Bergman, D.J.; Kobayashi, T. Coherent control of nanoscale localization of ultrafast optical excitation in nanosystems, Physical Review B 69, 054202 (2004).

64. Stockman, M.I. Ultrafast nanoplasmonics under coherent control. New Journal of Physics 10, 025031 (2008).

65. Wollenhaupt, M.; Bayer, T.; Baumert, T. Control of Ultrafast Electron Dynamics with Shaped Femtosecond Laser Pulses: From Atoms to Solids. In: Kitzler M., Gräfe, S. (eds) Ultrafast Dynamics Driven by Intense Light Pulses, Springer Series on Atomic, Optical, and Plasma Physics, 86, Springer, Cham (2016).

66. Rullire, C. *Femtosecond laser pulses; principles and experiments*, Springer (2005).

67. Serrat, C.; Biegert, J. Energy efficient method for two-photon population transfer with near-resonant chirped pulses. Opt. Express, 16, 19667–19673 (2008).

68. McCall, S.L.; Hahn, E.L., Self-Induced Transparency. Phys. Rev. 183, 457 (1969); Allen, L. and Eberly, J.H. *Optical Resonance and Two-Level Atoms,* Dover Publications (1987).

69. Eberly, J.H. Area Theorem rederived. Optics Express, 2(5): 173 – 176 (1998).

70. Cao, J.; Bardeen, C.J., Wilson, K.R. Molecular π pulses: Population inversion with positively chirped short pulses. Journal of Chemical Physics, 113(5): 1898 (2000).

71. Malinovsky, V.S.; Krause, J.L. General theory of population transfer by adiabatic rapid passage with intense chirped laser pulses, European Phys. Journal D, 14: 147 – 155 (2001).

72. Liu, G; Zakharov, V., Collins, T., Gould, P.; Malinovskaya, S.A. Population inversion in hyperfine states of Rb with a single nanosecond chirped pulse in the framework of a four-level system, Phys. Rev. A, 89, 041803(R) (2014).

73. Gavrila M. *Atoms in Intense Fields,* Academic, NY (1992).

74. Rhodes, C.K. Multiphoton ionization of atoms. Science, 229, 1345 (1985).

75. Clark, C.W.; Littman, M.G.; Miles, R.; Skinner, C.H.; McIlrath, T.J.Possibilities for achieving x-ray lasing action by use of high-order multiphoton processes, Journal of the Optical Soc. Am. B, 3, 371 – 378 (1986).

76. Afa, I.J., Font, J.L., Serrat, C. Control of rubidium low-lying Rydberg states with trichromatic femtosecond π-pulses for ultrafast quantum information processing, Phys Rev A, 96(5), 053843 (2017).

77. Gibson, G.N. Multiphoton π pulses, Phys. Rev. Lett. 89(26): 263001 (2003).

78. Holthaus M.; Just, B. Generalized π pulses, Phys. Rev. A, 49, 1950 (1994).

79. Grynberg, G.; Aspect, A.; Fabre, C. *Introduction to Quantum Optics: From the Semi-classical Approach to Quantized Light*, Cambridge University Press, Science (2010).

80. Boyd, R. *Nonlinear Optics*, 3rd ed., Academic Press (2008).

81. Weiner, A. *Ultrafast Optics*, Wiley (2009).

82. Buckup, T.; Hauer, J.; Serrat, C.; Motzkus, M. Control of excited-state population and vibrational coherence with shaped-resonant and near-resonant excitation. J. Phys. B At. Mol. Opt. Phys., 41(7), 074024 (2008).

83. Afa, I.J.; Serrat, C. Quantum Control of Population Transfer and Vibrational States via Chirped Pulses in Four Level Density Matrix Equations, Appl. Sci. 6, 351 (2016).

84. Braun, M.; Sobotta, C.; Durr, R.; Pulvermacher, H.; Malkmus, S. Analysis of wave packet motion in frequency and time domain: Oxazine 1, Journal of Physical Chemistry, 110(32): 9793 – 9800 (2006).

85. Drummond, P.D.; Hillery, M. *The Quantum Theory of Nonlinear Optics*, Cambridge University Press, Science (2014).

86. Kien, F.L.; Hakuta, K. *Density operator and applications in nonlinear optics*. Lecture notes (winter semester) (2004). Available online.

87. Fainberg, B.D.; Gorbunov, V.A. Coherent population transfer in molecules coupled with a dissipative environment by intense ultrashort chirped pulse, Journal of Chemical Physics, 117(15): 7222 – 7232 (2002).

88. C. Serrat, M. Corbera, J. Afa, "Trichromatic π-Pulse for Ultrafast Total Inversion of a Four-Level Ladder System", Appl. Sci. 5, 1484 (2015).

89. Hioe, F.T.; Bergmann, K. Adiabatic population transfer in a three-level system driven by delayed laser pulses. Phys. Rev. A, 40, 6741–6744 (1989).

90. Schiemann, S.; Kuhn, A.; Steuerwald, S.; Bergmann, K. Efficient coherent population transfer in NO molecules using pulsed lasers. Phys. Rev. Lett., 71, 3637–3640 (1993).

91. Bergmann, K.; Theuer, H.; Shore, B.W. Coherent population transfer among quantum states of atoms and molecules. Rev. Mod. Phys., 70, 1003–1025 (1998).

92. Král, P.; Thanopulos, I.; Shapiro, M. Colloquium: Coherently controlled adiabatic passage. Rev. Mod. Phys., 79(1), 53 (2007).

93. Diels, J.-C.; Besnainou, S. Multiphoton coherent excitation of molecules. J. Chem. Phys., 85, 6347–6355 (1986).

94. Brewer, R.G.; Hahn, E.L. Coherent two-photon processes: Transient and steady-state cases. Phys. Rev. A, 11, 1641–1649 (1975).

95. Sargent, M., III; Horwitz, P. Three-level Rabi flopping. Phys. Rev. A, 13, 1962–1964 (1976).

96. Shore, B.W.; Ackerhalt, J. Dynamics of multilevel laser excitation: Three-level atoms. Phys. Rev. A, 15, 1640–1647 (1977).

97. Choe, A.S.; Rhee, Y.; Lee, J.; Han, P.S.; Borisov, S.K.; Kuzmina, M.A.; Mishin, V.A. Effective excitation method of a three-level medium in a selective photoionization. Phys. Rev. A, 52, 382–386 (1995).

98. Linskens, A.F.; Holleman, I.; Dam, N.; Reuss, J. Two-photon Rabi oscillations. Phys. Rev. A, 54, 4854–4862 (1996).

99. Zhang, B.; Wu, J.-H.; Yan, X.-Z.; Wang, L.; Zhang, X.-J.; Gao, J.-Y. Coherence generation and population transfer by stimulated Raman adiabatic passage and π pulse in a four-level ladder system. Opt. Express, 19, 12000–12007 (2011).

100. Ziolkowski, R.W.; Arnold, J.M.; Gogny, D.M. Ultrafast pulse interactions with two-level atoms. Phys. Rev. A, 52, 3082–3094 (1995).

101. Biegert, J.; Diels, J.-C. Feasibility study to create a polychromatic guidestar in atomic sodium. Phys. Rev. A, 67, 043403 (2003).

102. Wrzesinski, P.J.; Pestov, D.; Lozovoy, V.V.; Gord, J.R.; Dantus, M.; Roy, S. Group-velocity-dispersion measurements of atmospheric and combustion-related gases using an ultrabroadband-laser source. Opt. Express, 19, 5163–5171 (2011).

103. Zimmerman, M.L.; Littman, M.G.; Kash, M.M.; Kleppner, D. Stark structure of the Rydberg states of alkali-metal atoms, Phys. Rev. A, 20, 2251 (1979).

104. Pohl, T.; Berman, P.R. Breaking the Dipole Blockade: Nearly resonant dipole interactions in few-atom systems, Phys. Rev. Lett. 102, 013004 (2009).

105. Lim, J; Lee, H.; Ahn, J. Review of cold Rydberg atoms and their applications, Journal of the Korean Physical Society, 63, 867 – 876 (2013).

106. Kleppner, D.; Littman, M.G.; Zimmerman, M.L. Highly excited atoms, Scientific American, 244, 108 – 122 (1981).

107. Martinson, I; Curtis, L.J. Janne Rydberg – his life and work, Nuclear Intruments and Methods in Physics Research B, 235, 17-22 (2005)

108. Gallagher, T.F. *Rydberg atoms*, Cambridge University Press, New York (1994).

109. Gallas, J.A.C.; Leuchs, G.; Walther, H.; Figger, H. Rydberg atoms: High-resolution spectroscopy and radiation interaction-Rydberg molecules, Advances in Atomic and Molecular Physics, 20, 413 – 466 (1985).

110. Gnedin, Y.N.; Mihajlov, A.A.; *et al*. Rydberg atoms in astrophysics, New Astronomy Reviews, 53(7-10): 259 – 265 (2009).

111. Killian T.C.; Kulin, S.; Bergeson, S.D.; Orozco, L.A.; Orzel, C.; Rolston, S.L. Creation of an ultracold neutral plasma, Phys. Rev. Let. 83, 4776 (1999).

112. Saffman, M. Quantum computing with atomic qubits and Rydberg interactions: progress and challenges, J. Phys. B: At. Mol. Opt. Phys. 49, 202001 (2016).

113. Maller, K.M.; Lichtman, M.T.; Xia, T.; Piotrowicz, M.J.; Carr, A.W.; Isenhower, L.; Saffman, M., Rydberg-blockade controlled-NOT gate and entanglement in a two-dimensional array of neutral-atom qubits, Phys. Rev. A, 92(2): 022336 (2015).

114. Pritchard *et al*. Cooperative atom-light interaction in a blockaded Rydberg ensemble, Phys. Rev. Lett. 105, 193603 (2010).

115. Lukin, M.D. *et al.* Dipole blockade and quantum information processing in mesoscopic atomic ensembles, Phys. Rev. Lett. 87, 037901 (2001).

116. Branden D.B.; Juhasz, T. ; Mahlokozera, T.; Vesa, C. *et al*. Radiative lifetime measurements of rubidium Rydberg states, J. Phys. B: At. Mol. Opt. Phys., 43, 015002 (2010).

117. Duan, L.-M. Scaling Ion Trap Quantum Computation through Fast Quantum Gates, Phys. Rev. Lett. 93, 100501 (2004).

118. de Vivie-Riedle, R.; Troppmann, U. Femtosecond Lasers for Quantum Information Technology, Chem. Rev. 107, 5082 (2007).

119. Ahn, J.; Weinacht, T. C.; Bucksbaum, P. H. Information storage and retrieval through quantum phase, Science 287, 463 (2000).

120. Weinacht, T. C.; Ahn, J.; Bucksbaum, P. H.; Controlling the shape of a quantum wavefucntion. Nature (London), 397, 233 (1999).

121. Preclíková, J.; Kozák, M.; Fregenal, D.; Frette, Ø.; Hamre, B.; Hjertaker, B.T.; Hansen, J.P.; Kocbach, L. Excitation of Rydberg wave packets with chirped laser pulses, Phys. Rev. A 86, 063418 (2012).

122. Kozák, M.; Preclíková, J.; Fregenal, D.; Hansen, J.P. State-selective Rydberg excitation with femtosecond pulses, Phys. Rev. A 87, 043421 (2013).

123. Safronova, M.S.; Johnson, W.R.; Derevianko, A. Relativistic many-body calculations of energy levels, hyperine constants, electric-dipole matrix elements, and static polarizabilities for alkali-metal atoms", Phys. Rev. A 60, 4476 (1999).

124. Safronova, M.S.; Williams, C.J.; Clark, C.W. Relativistic many-body calculations of electric-dipole matrix elements, lifetimes and polarizabilities in rubidium, Phys. Rev. A 69, 022509 (2004).

125. Siegman, A.E. Lasers, University Science Books, Sausalito CA 94965 (1986), p. 99.

126. Li, X.-H.; Zhang, X.-Z.; Zhang, R.-Z.; Yang, X.-D. Population transfer via adiabatic passage in Rydberg potassium atom, Chinese Phys. 16, 2924 (2007).

127. Bajema, M.L.; Jones, R.R.; Gallagher, T.F. Femtosecond laser control of the angular distribution of electrons due to autoionization, Phys. Rev. A, 70, 062722 (2004).

128. Brandenberger, J.R.; Malyshev, G.S. Fine-structure splitting in high-lying ^2F states of rubidium via three-step laser spectroscopy, Phys. Rev. A, 81, 032515 (2010).

129. Carr, C. *et al*. Three-photon electromagnetically induced transparency using Rydberg states. Optics Lett., 37(18): 3858 – 3860 (2012).

130. Vogt, T.; Viteau, M.; Zhao, J.; Chotia, A.; Zhao, J.; Comparat, D.; Pillet, P. Electric-field induced dipole blocakde with Rydberg atoms, Phys. Rev. Lett. 97, 083003 (2006).

131. Deiglmayr, J.; Reetz-Lamour, M.; Amthor, T.; Westermann, S.; de Oliviera, A.L.; Weidemuller, M. Coherent excitation of Rydberg atoms in an ultracold gas, Opt. Comm. 264, 298 (2006).

132. Thoumany, P.; Germann, T.; Hansch, T.; Stania, G.; Urbonas, L.; Becker, T. Spectroscopy of rubidium Rydberg states with three diode lasers, J. Mod. Opt. 56, 2055 (2009).

133. Ryabtsev, I.I.; Beterov, I.I.; Tretyakov, D.B.; Entin, V.M.; Yakshina, E.A. Doppler- and recoil-free laser excitation of Rydberg states via three-photon transitions, Phys. Rev. A 84, 053409 (2011).

134. Qian, J.; Zhai, J.; Zhang, L.; Zhang, W., Chirped multiphoton adiabatic passage for four-level ladder-type Rydberg excitation, Phys. Rev. A 91, 013411 (2015).

135. Ryabtsev, I.I.; Beterov, I.I.; Tretyakov, D.B.; Entin, V.M.; Yakshina, E.A. Spectroscopy of cold rubidium Rydberg atoms for applications in quantum information, Physics - Uspekhi 59, 196 (2016).

136. Volkova, E.A.; Popov, A.M.; Tikhonova, O.V. Numerical modeling of the photoionization of Rydberg atoms by the field of an electromagnetic wave, J. Exp. Theor. Phys. 86, 328 (1998).

137. Autler, S.H.; Townes, C.H. Stark Effect in Rapidly Varying Fields, Phys. Rev. 100, 703 (1955).

138. Chen, C. An introduction to coherent multidimensional spectroscopy, Applied Spectroscopy, 70(12): 1937 – 1951 (2016).

139. Schmitt, M.; Knopp, G.; Materny, A.; Kiefer, W. Femtosecond time-resolved four-wave mixing spectroscopy in iodine vapour, Chem. Phys. Lett., 280(3-4): 339 – 347 (1997).

140. Terada, Y.; Yoshida, S., Takeuchi O.; Shigekawa, H. Real-Space imaging of transient carrier dynamics by nanoscale pump-probe microscopy, Nature Photonics, 4, 869 – 874 (2010).

141. Silberberg, Y. Quantum coherent control for nonlinear spectroscopy and microscopy, Annual Review of Physical Chemistry, 60(1): 277 – 292 (2009).

142. Brixner, T.; Pfeifer T, Gerber, G.; Wollenhaupt, M.; Baumert, T. *2004 Progress in Lasers: Femtosecond Laser Spectroscopy*; Kluwer: Dordecht, The Netherlands (2004) Volume 9, pp. 229–271.

143. Kohler, B.; Yakovlev, V.V.; Che, J.; Krause, J.L.; Messina, M.; Wilson, K.R.; Schwentner, N.; Whitnell, R.M.; Yan, Y. Quantum control of wave packet evolution with tailored femtosecond pulses. *Phys. Rev. Lett.*, 74, 3360 (1995).

144. Vogt, G.; Nuernberger, P.; Brixner, T.; Gerber, G. Femtosecond pump-shaped-dump quantum control of retinal isomerization in bacteriorhodopsin. Chem. Phys. Lett., 433, 211–215 (2006).

145. Baumert, T.; Helbing, J.; Gerber, G. *Advances in Chemical Physics-Photochemistry*; Wiley: New York, NY, USA (1997); pp. 47–77.

146. Tannor, D.; Kazakov, V.; Orlov, V. *Time Dependent Quantum Molecular Dynamics*; Plenum: New York, NY, USA (1992); pp. 347–360.

147. Meshulach, D.; Silberberg, Y. Coherent quantum control of manipulation transitions by shaped ultrashort optical pulses. Phys. Rev. A, 60, 1287 (1999).

148. Meshulach, D.; Silberberg, Y. Coherent quantum control of two-photon transitions by femtosecond laser pulse. Nature, *396*, 239–242 (1998).

149. Krüger, M.; Schenk, M.; Hommelhoff, P. Attosecond control of electrons emitted from a nanoscale metal tip. Nature, 475, 78–81 (2011).

150. Herek, J.L.; Wohlleben, W.; Cogdell, R.J.; Zeidler, D.; Motzkus, M. Quantum control of energy flow in light harvesting. Nature, 417, 533–535 (2002).

151. Prokhorenko, V.I.; Nagy, A.M.; Waschuk, S.A.; Brown, L.S.; Birge, R.R.; Miller, R.J.D. Coherent control of retinal isomerization in Bacteriorhodopsin. Science, 313, 1257–1261 (2006).

152. Feurer, T.; Vaughan, J.C.; Nelson, K.A. Spatiotemporal coherent control of lattice vibrational waves. Science, *299*, 374–377 (2003).

153. Lüker, S.; Gawarecki, K.; Reiter, D.E.; Grodecka-Grad, A.; Axt, V.M.; Machnikowski, P.; Kuhn, T. Influence of acoustic phonons on the optical control of quantum dots driven by adiabatic passage. Phys. Rev. B, 85, 121302 (2012).

154. Debnath, A.; Meier, C.; Chatel, B.; Amand, T. Chirped laser excitation of quantum dot excitons coupled to a phonon bath. Phys. Rev. B, 86, 161304 (2012).

155. Renaud, N.; Grozema, F.C. Cooperative biexciton generation and destructive interference in coupled quantum dots uing adiabatic rapid passage. *Phys. Rev. B*, 90, 165307 (2014).

156. Kuroda, D.G.; Singh, C.P.; Peng, Z.; Kleiman, V.D. Mapping excited-state dynamics by coherent control of a dendrimer's photoemission efficiency. Science, 326, 263–267 (2009).

157. Zewail, A.H. *Femtochemistry: Ultrafast Dynamics of the Chemical Bond*; World Sci.: New York, NJ, USA (1994).

158. Nuernberger, P.; Vogt, G.; Brixner, T.; Gerber, G. Femtosecond quantum control of molecular dynamics in the condensed phase. Phys. Chem. Chem. Phys., 9, 2470–2497 (2007).

159. Picón, A.; Biegert, J.; Jaron-Becker, A.; Becker, A. Coherent control of the vibrational state population in a nonpolar molecule. Phys. Rev. A, 83, 023412 (2011).

160. Zhang, Z.; Yang, X.; Yan, X. Selective and efficient control of population transfer in the presence of an equally populated initial doublet. J. Opt. Soc. Am. B, 29, 1551–1556 (2012).

161. Kumar, P.; Sarma, A.K. Ultrafast and selective coherent population transfer in four-level atoms by a single nonlinearly chirped femtosecond pulse. Phys. Rev. A, 88, 033823 (2013).

162. Zhang, Z.; Tian, J.; Du, J. Selective population transfer and creation of an arbitrary superposition between quantum states in a Λ-type four-level system by a single linearly chirped pulse. Laser Phys. Lett., 13(5), 055201 (2016).

163. Weiner, A.M.; Leaird, D.E.; Wiederrecht, G.P.; Nelson, K.A. Femtosecond pulse sequences used for optical manipulation of molecular motion. Science, 247, 1317–1319 (1990).

164. Hauer, J.; Skenderovic, H.; Kompa, K.L.; Motzkus, M. Enhancement of Raman modes by coherent control in β-carotene. Chem. Phys. Lett., 421, 523–528 (2006).

165. Buckup, T.; Hauer, J.; Motzkus, M. On the paradigm of coherent control: The phase-dependent light-matter interaction in the shaping window. New J. Phys., 11, 105049 (2009).

166. Hauer, J.; Buckup, T.; Motzkus, M. Quantum control spectroscopy of vibrational modes: Comparison of control scenarios for ground and excited states in β-carotene. Chem. Phys., 350, 220–229 (2008).

167. Wohllenben, W.; Buckup, T.; Herek, J.L.; Motzkus, M. Coherent control for spectroscopy and manipulation of biological dynamics. ChemPhysChem., 6, 850–857 (2005).

168. Hauer, J.; Buckup, T.; Skenderovic, H.; Kompa, K.L.; Motzkus, M. Enhancement of Raman modes in complex molecules by coherent control. In *Ultrafast Phenomena, X.V.*; Springer: Berlin, Germany (2007); p. 303.

169. Hornung, T.; Skenderovic, H.; Motzkus, M. Observation of all-trans-β-carotene wavepacket motion on the electronic ground and excited state using degenerate four-wave mixing (DFWM) and pump-DFWM. Chem. Phys. Lett., 402, 283–288 (2005).

170. Kiefer, W.; Materny, A.; Schmitt, M. Femtosecond time-resolved spectroscopy of elementary molecular dynamics. Naturwissenschaften, 89, 250–258 (2002).

171. Siebert, T.; Maksimenka, R.; Materny, A.; Engel, V.; Kiefer, W.; Schmitt, M. The role of specific normal modes during non-Born-Oppenheimer dynamics: The S_1-S_0 internal conversion of β-caroteneinterrogated on a femtosecond time-scale with coherent anti-Stokes Raman scattering. J. Ram. Spect., 33, 844–854 (2002).

172. Bitter, M.; Shapiro, E.A.; Milner, V. Enhancing strong-field-induced molecular vibration with femtosecond pulse shaping. Phys. Rev. A, 86, 043421 (2012)..

173. Buckup, T.; Hauer, J.; Voll, J.; Vivie-Riedle, R.; Motzkus, M. A general control mechanism of energy flow in the excited state of polyenic biochromophores. Faraday Discuss, 153, 213–225 (2011).

174. Amitay, Z.; Uberna, R.; Leone, S.R. Time-shifting the dynamics of Li2 multistate rovibrational wavepackets by state selective coherent phase control. *Advances in Multiphoton Processes and Spectroscopy:* Proc of US-Japan Workshop, Honolulu, USA, 12–15 December 1999; Gordon, R.J.; Fujimura, Y., Eds.; World Scientific,: Singapore (2000); Volume 14, pp. 3–14.

175. Andrianov, I.V.; Paramonov, G.K. Selective excitation of the vibrational-rotational states and dissociation of diatomic molecules by picoseconds infrared laser pulses: Modelling for HF in the ground electronic state. Phys. Rev. A, 59, 2134 (1999).

176. Korolkov, M.V.; Paramonov, G.K. Vibrationally state-selective electronic excitation of diatomic molecules by ultrashort laser pulses. Phys. Rev. A, 57, 4998 (1998).

177. Savolainen, J.; Fanciulli, R.; Dijkhuizen, N.; Moore, A.L.; Hauer, J.; Buckup, T.; Motzkus, M.; Herek, J.L. Controlling the efficiency of an artificial light-harvesting complex. Proc. Natl. Acad. Sci. USA, 105, 7641–7646 (2008).

178. Savolainen, J.; Buckup, T.; Hauer, J.; Jafarpour, A.; Serrat, C.; Motzkus, M.; Herek, J.L. Carotenoid deactivation in an artificial light-harvesting complex via a vibrationally hot ground state. Chem. Phys., 357, 181–187 (2009).

179. Buckup, T.; Lebold, T.; Weigel, A.; Wohlleben, W.; Motzkus, M. Singlet versus triplet dynamics of β-carotene studied by quantum control spectroscopy. J. Photochem. Photobiol. A, 180, 314–321 (2006).

180. Buckup, T.; Hauer, J.; Möhring, J.; Motzkus, M. Multidimensional spectroscopy of β-carotene: Vibrational cooling in the excited state. Arch. Biochem. Biophys., 483, 219–223 (2009).

181. Buckup, T.; Lebold, T.; Weigel, A.; Wohlleben, W.; Motzkus, M. Multiphoton Quantum-control spectroscopy of β-carotene. In *Ultrafast Phenomena, X.V.*; Springer: Berlin, Germany, 2007; p. 483.

182. Buckup, T.; Savolainen, J.; Wohlleben, W.; Herek, J.L.; Hashimoto, H.; Correia, R.R.B.; Motzkus, M. Pump-probe and pump-deplete-probe spectroscopies on carotenoids with N = 9–15 conjugated bonds. J. Chem. Phys., 125, (2006).

183. Buckup, T.; Wohlleben, W.; Heinz, B.; Savolainen, J.; Herek, J.L.; Hashimoto, H.; Cogdell, R.J.; Motzkus, M. Energy flow in carotenoids, studied with pump-deplete-probe, multiphoton- and coherent control spectroscopy. In *Ultrafast Phenomena XIV*; Springer: Berlin, Germany (2005); p. 368.

184. Consani, C.; Ruetzel, S.; Nuernberger, P.; Brixner, T. Quantum control spectroscopy of competing reaction pathways in a molecular switch. J. Phys. Chem. A, 118, 11364–11372 (2014).

185. Wohlleben, W.; Buckup, T.; Hashimoto, H.; Cogdell, R.J.; Herek, J.L.; Motzkus, M. Pump-deplete-probe spectroscopy and the puzzle of carotenoid dark states. J. Phys. Chem. B, 108, 3320–3325 (2004).

186. Kraack, J.P.; Motzkus, M.; Buckup, T. Selective nonlinear response preparation using femtosecond spectrally resolved four-wave-mixing. J. Chem. Phys., 135 (2011).

187. Nuernberger, P.; Ruetzel, S.; Brixner, T. Multidimensional electronic spectroscopy of photochemical reactions. Angew. Chem. Int. Ed. Engl., 54, 11368–11385 (2015).

188. Ruetzel, S.; Diekmann, M.; Nuernberger, P.; Walter, C.; Engels, B.; Brixner, T. Multidimensional spectroscopy of photoreactivity. Proc. Natl. Acad. Sci. USA, 111, 4764–4769 (2014).

189. Meshulach, D.; Yelin, D.; Silberberg, Y. Adaptive real-time femtosecond pulse shaping. J. Opt. Soc. Am. B, 15, 1615–1619 (1998).

190. Yelin, D.; Meshulach, D.; Silberberg, Y. Adaptive femtosecond pulse compression. Opt. Lett., 22, 1793–1795 (1997).

191. Feist, A.; Echternkamp, K.E.; Schauss, J.; Yalunin, S.V.; Schafer, S.; Ropers, C. Quantum coherent optical phase modulation in an ultrafast transmission electron microscope. Nature, 521, 200–203 (2015).

192. Yan, Y.J.; Mukamel, S. Electronic dephasing, vibrational relaxation, and solvent friction in molecular nonlinear optical line shapes. J. Chem. Phys., 89 (1988).

193. Joo, T.; Albrecht, A.C. Electronic dephasing studies of molecules in solution at room temperature by femtosecond degenerate four wave mixing. Chem. Phys., 176, 233–247 (1993).

194. Nibbering, E.T.J.; Duppen, K.; Wiersma, D.A. Optical dephasing in solution: A line shape and resonance light scattering study of azulene in isopentane and cyclohexane. J. Chem. Phys., 93 (1990).

195. Wand, A.; Kallush, S.; Shoshanim, O.; Bismuth, O.; Kosloff, R.; Ruhman, S. Chirp effects on impulsive vibrational spectroscopy: A multimode perspective. Phys. Chem. Chem. Phys., 12, 2149–2163 (2010).

196. Malkmus, S.; Dürr, R.; Sobotta, C.; Pulvermacher, H.; Zinth, W.; Braun, M. Chirp dependence of wave packet motion in Oxazine 1. J. Phys. Chem. A, 109, 10488–10492 (2005).

197. Ruhman, S.; Kosloff, R. Application of chirped ultrashort pulses for generating large-amplitude ground-state vibrational coherence: A computer simulation. J. Opt. Soc. Am. B, 7, 1748–1752 (1990).

198. Bardeen, C.J.; Wang, Q.; Shank, C.V. Selective excitation of vibrational wave packet motion using chirped pulses. Phys. Rev. Lett., 75, 3410 (1995).

199. Cao, J.; Bardeen, C.J.; Wilson, K.R. Molecular π-pulse for total inversion of electronic state population. Phys. Rev. Lett., 80, 1406 (1998).

200. Konar, A.; Lozovoy, V.V.; Dantus, M. Solvent environment revealed by positively chirped pulses. J. Phys. Chem. Lett., 5, 924–928 (2014).

201. Möhring, J.; Buckup, T.; Motzkus, M. A Quantum control spectroscopy approach by direct UV femtosecond pulse shaping. IEEE J. Sel. Top. Quant. Elect., 18, 449–459 (2012).

202. Carroll, E.C.; Florean, A.C.; Bucksbaum, P.H.; Spears, K.G.; Sension, R.J. Phase control of the competition between electronic transitions in a solvated laser dye. Chem. Phys., 350, 75–86 (2008).

203. Chini, M.; Wang, X.; Cheng, Y.; Chang, Z. Resonance effects and quantum beats in attosecond transient absorption of helium, J. Phys. B: At. Mol. Opt. Phys., 47, 124009 (2014).

204. Martín, F.; Cheng, Y.; Chini, M.; Wang, A.; *et al*. Attosecond transient absorption spectroscopy of molecular hydrogen, J. Phys.: Conference series (IOP Publishing), 635, 112070 (2015).

205. Pabst, S.; Sytcheva, A.; Moulet, A.; Wirth, A.; Goulielmakis, E.; Santra, R. Theory of attosecond transient-absorption spectroscopy of krypton for overlapping pump and probe pulses, Phys. Rev. A, 86, 063411 (2012).

206. Otobe, T. Theory of attosecond transient absorption spectroscopy in solids, arXiv: 1707.07462v2 (2017).

207. Gaarde, M.B.; Buth, C.; Tate, J.L.; Schafer, K.J. Transient absorption and reshaping of ultrafast XUV light by laser-dressed helium," Phys. Rev. A 83, 013419 (2011).

208. Corkum, P.B. Plasma perspective on strong-field multiphoton ionization, Phys. Rev. Lett. 71, 1994 – 1997 (1993).

209. Pabst, S.; Santra, R. Spin-orbit effects in atomic high-harmonic generation, J. Phys. B: At. Mol. Opt. Phys., 47, 124026 (2014).

210. Santra, R.; Yakovlev, V.S.; Pfeifer, T.; Loh Z.-H. Theory of attosecond transient absorption spectroscopy of strong-field-generated ions, Phys. Rev. A, 83, 033404 (2011).

211. Wang, H.; Chini, M.; Chen, S.; Zhang, C.-H.; He, F.; Cheng, Y.; Wu, Y.; Thumm, U.; Chang, Z. Attosecond Time-Resolved Autoionization of Argon, Phys. Rev. Lett. 105, 143002 (2010).

212. Wirth, A.; Hassan, M.T.; Grguras, J.; Gagnon, J.; Moulet, A.; *et al*. Synthesized Light Transients, Science, 334, 195 (2011).

213. Pabst, S. Greenman, L., Ho P.J., Mazziotti, D.A., Santra, R. Decoherence in Attosecond Photoionization, Phys. Rev. Lett., 106, 053003 (2011).

214. Pfeiffer, A.N.; Leone, S.R. Transmission of an isolated attosecond pulse in a strong-field dressed atom, Phys. Rev. A 85, 053422 (2012).

215. Chini, M.; Zhao, B.; Wang, H.; Cheng, Y.; Hu, S.X.; Chang, Z. Subcycle ac Stark shift of Helium excited states probed with isolated attosecond pulses, Phys. Rev. Lett. 109, 073601 (2012).

216. Wu, M.; Chen, S.; Camp, S.; Schafer, K.J.; Gaarde, M.B. Theory of strong- field attosecond transient absorption, J. Phys. B. 49, 062003 (2016).

217. Seres, J.; Seres, E.; Landgraf, B.; Ecker, B.; Aurand, B.; Hoffmann, A.; Winkler, G.; Namba, S.; Kuehl, T.; Spielmann, C. Parametric amplification of attosecond pulse trains at 11 nm, Sci. Rep. 4, 4254 (2014).

218. Serrat, C.; Roca, D.; Budesca, J.M.; Seres, J.; Seres, E.; Aurand, B.; Hoffmann, A.; Namba, S.; Kuehl, T.; Spielmann, C. Avalanche of stimulated forward scattering in high harmonic generation, Opt. Express 24(8), 8028-8044 (2016).

219. Seres, E.; Seres, J.; Spielmann, C. X-ray absorption spectroscopy in the keV range with laser generated high harmonic radiation, Appl. Phys. Lett. 89, 181919 (2006).

220. Popmintchev, T.; Chen, M.-C.; Popmintchev, D.; Arpin, P.; Brown, S.; Alisauskas, S.; Andriukaitis, G.; Balciunas, T.; Mucke, O.D.; Pugzlys, A.; Baltuska, A.; Shim, B.; Schrauth, S.E.; Gaeta, A.; Hernández-García, C.; Plaja, L.; Becker, A.; Jaron-Becker, A.; Murnane, M.M.; Kapteyn, H.C. Bright Coherent Ultrahigh Harmonics in the keV X-ray Regime from Mid-Infrared Femtosecond Lasers, Science 336, 1287-1291 (2012).

221. Seres, J.; Seres, E.; Landgraf, B.; Ecker, B.; Aurand, B.; Kuehl, T.; Spielmann, C. High-harmonic generation and parametric amplification in the soft X-rays from extended electron trajectories, Sci. Rep. 4, 4234 (2014).

222. Kwon, O.; Kim, D. PHz current switching in calcium fluoride single crystal, Appl. Phys. Lett. 108, 191112 (2016).

223. Schultze, M.; Ramasesha, K.; Pemmaraju, C.D.; Sato, S.A.; Whitmore, D.; Gandman, A.; Prell, J.S.; Borja, L.J.; Prendergast, D.; Yabana, K.; Neumark, D.M.; Leone, S.R. Attosecond band-gap dynamics in silicon, Science 346, 1348-1352 (2014).

224. Seres, E.; Seres, J.; Serrat, C.; Namba, S. Core-level attosecond transient absorption spectroscopy of laser-dressed solid films of Si and Zr, Phys. Rev. B 94, 165125 (2016).

225. Lucchini, M.; Sato, S.A.; Ludwig, A.; Herrmann, J.; Volkov, M.; Kasmi, L.; Shinohara, Y.; Yabana, K.; Gallmann, L.; Keller, U. Attosecond dynamical Franz-Keldysh effect in polycrystalline diamond, Science 353, 916-919 (2016).

226. Chini, M.; Wang, X.; Cheng, Y.; Wu, Y.; Zhao, D.; Telnov, D.A.; Chu, S.-I.; Chang, Z. Sub-cycle Oscillations in Virtual States Brought to Light, Sci. Rep. 3, 1105 (2013).

227. Reduzzi, M.; Hummert, J.; Dubrouil, A.; Calegari, F.; Nisoli, M.; Frassetto, F.; Poletto, L.; Chen, S.; Wu, M.; Gaarde, M.B.; Schafer, K.; Sansone, G. Polarization control of absorption of virtual dressed states in helium, Phys. Rev. A 92, 033408 (2015).

228. Simpson, E.R.; Sanchez-Gonzalez, A.; Austin, D.R.; Diveki, Z.; Hutchinson, S.E.E.; Siegel, T.; Ruberti, M.; Averbukh, V.; Miseikis, L.; Strüber, C.S.; Chipperfield, L.;

Marangos, J.P. Polarisation response of delay dependent absorption modulation in strong field dressed helium atoms probed near threshold, New J. Phys. 18, 083032 (2016).

229. Li, Y.; Gao, C.; Dong, W.; Zeng, J.; Zhao, Z.; Yuan, J. Coherence and resonance effects in the ultra-intense laser-induced ultrafast response of complex atoms, Sci. Rep. 6, 18529 (2016).

230. Wang, X.; Chini, M.; Cheng, Y.; Wu, Y.; Tong, X.-M.; Chang, Z. Subcycle laser control and quantum interferences in attosecond photoabsorption of neon, Phys. Rev. A 87, 063413 (2013).

231. Cheng, Y.; Chini, M.; Wang, X.; Gonzalez-Castrillo, A.; Palacios, A.; Argenti, L.; Martın, F.; Chang, Z. Reconstruction of an excited-state molecular wave packet with attosecond transient absorption spectroscopy, Phys. Rev. A 94, 023403 (2016).

232. Kobayashi, Y.; Timmers, H.; Sabbar, M.; Leone, S.R.; Neumark, D.M. Attosecond transient-absorption dynamics of xenon core-excited states in a strong driving field, Phys. Rev. A 95, 031401(R) (2017).

233. Sabbar, M.; Timmers, H.; Chen, Y.-J.; Pymer, A.K.; Loh, Z.-H.; Sayres, S.G.; Pabst, S.; Santra, R.; Leone, S.R. State-resolved attosecond reversible and irreversible dynamics in strong optical fields, Nat. Phys. 13, 472-478 (2017).

234. Ott, C.; Kaldun, A.; Argenti, L.; Raith, P.; Meyer, K.; Laux, M.; Zhang, Y.; Blattermann, A.; Hagstotz, S.; Ding, T.; Heck, R.; Madronero, J.; Martin, F.; Pfeifer, T. Reconstruction and control of a time-dependent two-electron wave packet, Nature 516, 374-378 (2014).

235. Goulielmakis, E.; Loh, Z.-H.; Wirth, A.; Santra, R.; Rohringer, N.; Yakovlev, V.S.; Zherebtsov, S.; Pfeifer, T.; Azzeer, A.M.; Kling, M.F.; Leone, S.R.; Krausz, F. Real-time observation of valence electron motion, Nature 466,739-744 (2010).

236. Hosler, E.R.; Leone, S.R. Characterization of vibrational wave packets by core-level high-harmonic transient absorption spectroscopy, Phys. Rev. A 88, 023420 (2013).

237. Attar, A.R.; Bhattacherjee, A.; Pemmaraju, C.D.; Schnorr, K.; Closser, K.D.; Prendergast, D.; Leone, S.R. Femtosecond x-ray spectroscopy of an electrocyclic ring-opening reaction, Science 356, 54-59 (2017).

238. Pertot, Y.; Schmidt, C.; Matthews, M.; Chauvet, A.; Huppert, M.; Svoboda, V.; Conta, A.; Tehlar, A.; Baykusheva, D.; Wolf, J.-P.; Wörner, H.J. Time-resolved x-ray absorption spectroscopy with a water window high-harmonic source, Science 355, 264-267 (2017).

239. Seres, E.; Spielmann, C. Ultrafast soft x-ray absorption spectroscopy with sub-20-fs resolution, Appl. Phys. Lett. 91, 121919 (2007).

240. Seres, E.; Spielmann, C. Time-resolved optical pump X-ray absorption probe spectroscopy in the range up to 1 keV with 20 fs resolution, J. Mod. Optics 55(16), 2643-2651 (2008).

241. Seres, E.; Seres, J.; Spielmann, C. Time resolved spectroscopy with femtosecond soft-x-ray pulses, Appl.Phys A 96, 43-50 (2009).

242. King, G.C.; Tronct, M.; Read, F.H.; Bradford, R.C. An investigation of the structure near the $L_{2,3}$ edges of argon, the $M_{4,5}$ edges of krypton and the $N_{4,5}$ edges of xenon, using electron impact with high resolution, J. Phys. B 10(12), 2479-2495 (1977).

243. Sairanen, O.-P.; Kivimaki, A.; Nommiste, E.; Aksela, H.; Aksela, S. High-resolution pre-edge structure in the inner-shell ionization threshold region of rare gases Xe, Kr, and Ar, Phys. Rev. A 54, 2834-2839 (1996).

244. Lang, J.; Watson, W.S. The photoabsorption coefficients of krypton and xenon from 48 Å to 210 Å, J. Phys. B 8(14), L339-L343 (1975).

245. West, J.B.; Marr, G.V. The absolute photoionization cross sections of helium, neon, argon and krypton in the extreme vacuum ultraviolet region of the spectrum, Proc. R. Soc. Lond. A. 349, 397-421 (1976).

246. Henke, B.L.; Gullikson, E.M.; Davis, J.C. X-ray interactions: photoabsorption, scattering, transmission, and reflection at E=50-30000 eV, Z=1-92, At. Data Nucl. Data Tables 54(2), 181-342 (1993).

247. Lin, M.-F.; Pfeiffer, A.N.; Neumark, D.M.; Leone, S.R.; Gessner, O. Strong-field induced XUV transmission and multiplet splitting in 4d-16p core-excited Xe studied by femtosecond XUV transient absorption spectroscopy, J. Chem. Phys. 137, 244305 (2012).

248. Herrmann, J.; Weger, M.; Locher, R.; Sabbar, M.; Riviere, P.; Saalmann, U.; Rost, J.-M.; Gallmann, L.; Keller, U. Virtual single-photon transition interrupted: Time-gated optical gain and loss, Phys. Rev. A 88, 043843 (2013).

249. Bauer, D.; Mulser, P. Exact field ionization rates in the barrier-suppression regime from numerical time-dependent Schrodinger-equation calculations, Phys. Rev. A 59, 569-577 (1999).

250. Kobayashi, Y.; Hirayama, N.; Ozawa, A.; Sukegawa, T.; Seki, T.; Kuramoto, Y.; Watanabe, S. 10-MHz, Yb-fiber chirped-pulse amplifier system with large-scale transmission gratings, Opt. Express 21(10), 12865-12873 (2013).